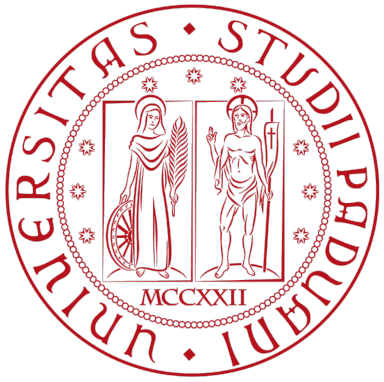

Università degli Studi di Padova

Dipartimento di
Fisica e Astronomia
Galileo Galilei

Scuola di dottorato in astronomia

XXXII ciclo

Probing the population of narrow-line Seyfert 1 galaxies with a southern hemisphere extended sampling

Supervisor:
Dr. Stefano Ciroi

Co-supervisors:
Dr. Marco Berton
Dr. Giovanni La Mura

Ph.D. student:
Sina Chen

Contents

List of Figures

List of Tables

Abstract

During my Ph.D., I carried out a multi-wavelength study of narrow-line Seyfert 1 galaxies (NLS1s), with the aim of better understanding this peculiar class of AGN.

I present a new accurately selected catalog of NLS1s in the southern hemisphere from the Six-degree Field Galaxy Survey (6dFGS) final data release. The classification was based on their optical spectral properties. I further derived for the first time their flux-calibrated spectra that are not provided by the 6dFGS. By analyzing these spectra, I obtained strong luminosity correlations between continuum and optical emission lines. The central black hole masses were estimated with methods based on the reverberation mapping, confirming that NLS1s indeed host a relatively low-mass black hole compared to broad-line Seyfert 1 galaxies (BLS1s).

In addition, I present a detailed study of a limited number of NLS1s from the 6dFGS sample that both have optical and X-ray spectroscopic observations. There are five complex NLS1s (C-NLS1s) and six simple NLS1s (S-NLS1s). I propose a possible correlation between [O III] line asymmetry and X-ray complexity. The outflow or wind from the inner accretion disk is commonly present in NLS1s and mostly directed along the system axis. S-NLS1s are sources viewed at a small inclination, where the speed of the wind is high thus the blueshift of the blue wing is large. Such a strong wind could blow away the ionized material, therefore result in a simple X-ray spectrum. At a large inclination, instead, the speed of the wind is low, thus the blueshift is less prominent in C-NLS1s. The presence of ionized material in the weak wind could lead to the X-ray spectral complexity.

A fraction of NLS1s are detected at radio frequency. I studied their radio properties at 1.4 GHz and 5 GHz using the NRAO VLA Sky Survey (NVSS) and the Karl G. Jansky Very Large Array (JVLA) respectively. Radio-loud (RL) sources tend to reside in the more distant universe, host a large massive black hole, and have a higher radio and optical luminosity compared to radio-quiet (RQ) sources. To extend the spectral coverage, I generated the test statistic (TS) maps for each radio-emitting source using the *Fermi*-LAT ten years data set, finding no γ-ray NLS1 in the sample.

Chapter 1

Introduction [1]

1.1 The AGN unification

Active galactic nuclei (AGN) are compact regions at the center of galaxies with much higher luminosities than their host galaxies. Their energies are emitted in all frequencies, radio, microwave, infrared, optical, ultra-violet, X-ray, and sometimes up to γ-ray, which can not be attributed to the composition of stars, gas, and dust of the host galaxies themselves. It is believed that the radiation of AGN is powered by accretion of matter falling into a supermassive black hole at the center of the galaxy.

AGN are composed of many classes having a variety of observed properties and a vast parameter space. The masses of central black hole M_{BH} range from 10^5 $M_\odot$ up to 10^{10} $M_\odot$, where $M_\odot$ is the mass of the Sun, and the bolometric luminosities L_{bol} are in the range of 10^{41} - 10^{48} erg s^{-1}. In addition, some AGN show rapid variability, while others appear as persistent sources. They reside in different kinds of galaxies, such as spiral or elliptical galaxies. It is believed that the various properties of AGN can be explained by several basic parameters with different values in a single model.

The simplest unification model of AGN was given by Antonucci (1993) to connect the various groups of AGN. Such scheme contains a central supermassive black hole, an accretion disk, a plasma corona above the disk, a molecular torus which is a dusty structure that surrounds the central engine on the equatorial plane, a broad-line region (BLR) and a narrow-line region (NLR) formed by gaseous clouds, a relativistic jet emitting radio and γ-ray radiation in the system, as shown in Fig. 1.1.

1.1.1 Black hole

It has long been assumed that supermassive black holes reside at the center of most galaxies. These central black holes have masses up to billion times that of the Sun, but their sizes are

[1] This chapter is based on Beckmann & Shrader (2012).

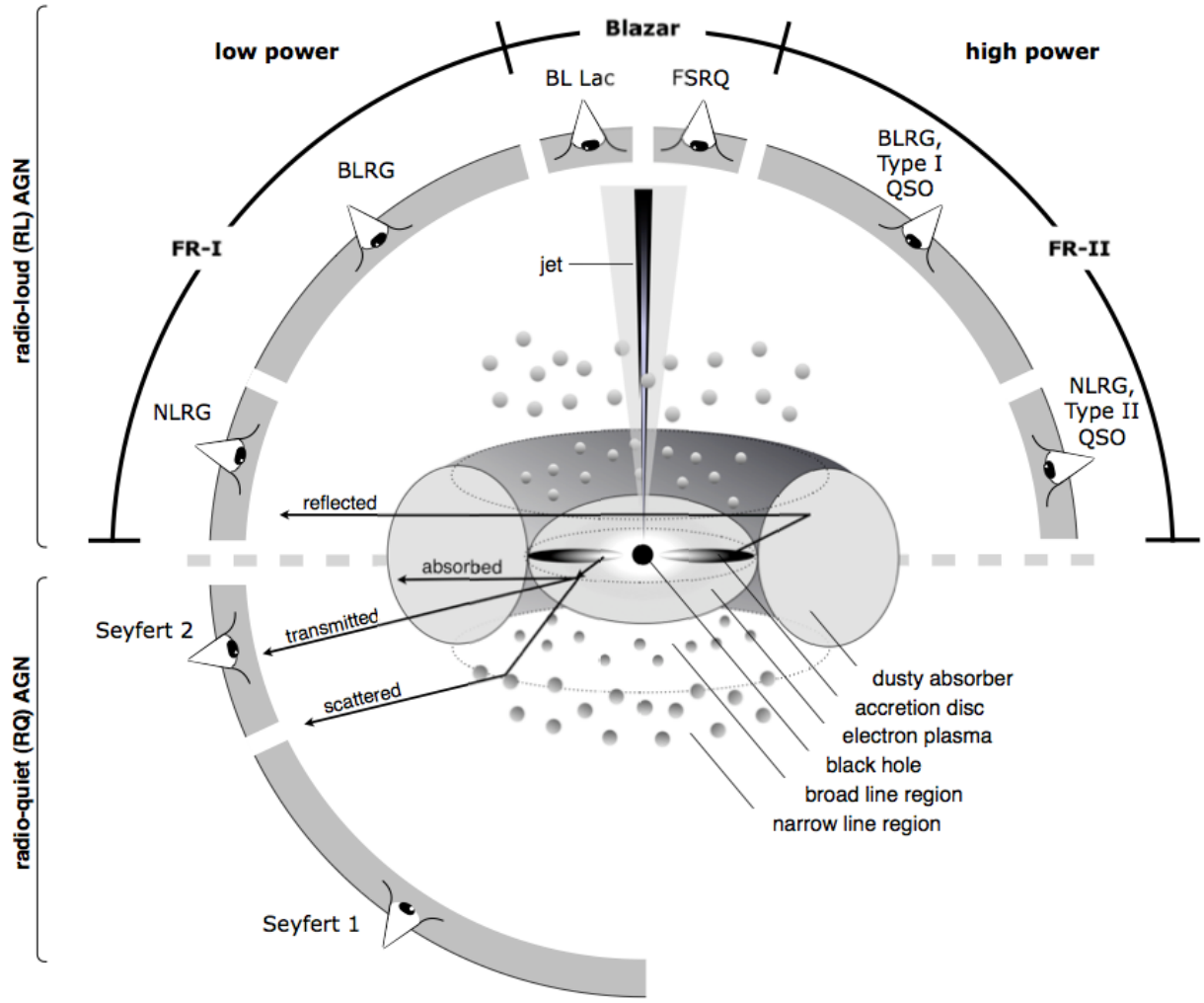

Figure 1.1: The AGN unified scheme. Figure is from Beckmann & Shrader (2012).

limited to a size smaller than one light day. Indeed AGN are powered by accretion onto the central massive black holes, as such a mechanism can provide highly efficient conversion of potential and kinetic energy to radiation. Hence AGN are able to maintain a persistent high luminosity, which in some cases is comparable to the Eddington limit. A black hole can not be observed directly like other sources, instead it can be detected through indirect ways, such as the interaction between a black hole and its surrounding environment, and the thermal radiation from in-falling matter heated to extreme temperatures.

A powerful method in establishing physical scales in the central region of AGN and probing the central black hole masses is known as reverberation mapping (Peterson, 1993). The observed spectra of some AGN consist of a strong continuum superposed by broad emission lines. The continuum is believed to be generated by an accretion process. Matter falls onto a black hole leading to the conversion of gravitational potential energy to

electromagnetic radiation. The broad emission lines, which are Doppler broadened by the strong gravitational field, are produced by the gas surrounding the central region in the unification scheme. Since these lines are created by photoionization or excitation from the continuum radiation, variations in the continuum should lead to the changes in the line emission delayed by a time of $\tau = R_{BLR}/c$, where R_{BLR} is the size of the BLR and c is the speed of light. The mass of black hole can then be determined by applying the virial theorem (Peterson et al., 2004; Peterson & Horne, 2004)

$$M_{BH} \simeq f R_{BLR} \frac{\Delta v^2}{G} = \frac{\tau c}{G} f \Delta v^2, \tag{1.1}$$

where f is a dimensionless scale factor that depends on structure, kinematics, and orientation of the BLR, Δv is the velocity dispersion of emission line, and G is the gravitational constant.

Another major method in estimating the central black hole mass of a galaxy is the so-called M_{BH} - σ_* relation, where σ_* is the stellar velocity dispersion of the galaxy bulge (Ferrarese & Merritt, 2000; Greene & Ho, 2006). This relation can be expressed as

$$\frac{M_{BH}}{M_\odot} = \alpha \left(\frac{\sigma}{200 \mathrm{km\,s^{-1}}} \right)^\beta, \tag{1.2}$$

where α and β depend on the surveys and vary a little (Gebhardt et al., 2000; Gültekin et al., 2009; Ho & Kim, 2014). This method is based on the idea that the central black hole of galaxy is closely related to the surrounding spheroidal distribution of stars (Magorrian et al., 1998), more precisely, is believed to be proportional to the galactic bulge mass, which in turn scales directly with an observable quantity σ_*.

1.1.2 Accretion disk

It is commonly believed that the basic mechanism underlying the AGN central engine is accretion. Matter orbiting the central black hole will settle into a flattened structure, which is referred to as an accretion disk. The gravitational field will draw the matter in the accretion disk falling onto the supermassive black hole with an accretion rate

$$\dot{M} = \frac{L_{acc}}{\eta c^2}, \tag{1.3}$$

where L_{acc} is the accretion luminosity and η is the mass-to-luminosity conversion efficiency. This will lead to viscous heating and conversion of gravitational potential energy to electromagnetic radiation. In principle, accretion onto the central black hole is limited by the effects of radiation pressure experienced by in-falling plasma. This limit depends on the mass of black hole and the mean opacity of in-falling material, usually referred to as the opacity of ionized hydrogen. The observable luminosity corresponding to the critical mass accretion rate in spherical symmetry for a black hole at a known distance is the Eddington

luminosity, which is obtained by equating the pressure gradient of in-falling matter to the radiation pressure,

$$L_{Edd} = \frac{4\pi G M_{BH} m_p c}{\sigma_T} \simeq 1.3 \times 10^{38} \frac{M_{BH}}{M_\odot} \mathrm{erg\,s^{-1}}, \tag{1.4}$$

where m_p is the proton mass and σ_T is the Thomson scattering cross-section. The Eddington ratio is the rate of the bolometric luminosity and the Eddington luminosity

$$\epsilon_{Edd} = \frac{L_{bol}}{L_{Edd}}, \tag{1.5}$$

the Eddington limit is reached when $\epsilon_{Edd} = 1$.

A remarkably useful accretion disk model in AGN is the geometrically thin but optically thick disk with a constant accretion rate (Shakura & Sunyaev, 1973), which is often referred to as an α-disk in literature. A basic assumption in the α-disk scenario is that the energy from accreting material is dissipated within a small region of the disk at its radius r. A part of the released gravitational energy goes into the kinetic energy of the gas, while the other emits away as the black body radiation with a temperature of T, since the disk material is optically thick. Applying an equilibrium between the releasing gravitational energy and the black body radiation leads to

$$T \propto (M_{BH}\dot{M})^{1/4} r^{-3/4}. \tag{1.6}$$

The spectral energy distribution (SED) of the accretion disk is described by the Planck function

$$B_\nu(T) \propto \nu^3 \left[\exp(\frac{h\nu}{kT}) - 1\right]^{-1}, \tag{1.7}$$

where B_ν is the spectral radiance of a black body at a frequency ν, h is the Planck constant, and k is the Boltzmann constant. The flux density at a given frequency is obtained via integration

$$S_\nu \propto \int_{R_{in}}^{R_{out}} B_\nu(T) 2\pi r dr, \tag{1.8}$$

where R_{in} and R_{out} are the radius of the inner and outer edges of the accretion disk respectively. This basic α-disk model has been successful in interpreting a number of observed AGN properties. However, some issues remain unresolved, such as super-Eddington accretion rates, launching of winds or jets, and double-peaked emission lines.

A basic problem of the accretion disk model is the conservation of angular momentum. The orbiting material falls onto the central black hole and loses angular momentum. Thus there should be a granting transport process that the angular momentum lost is balanced by the angular momentum gain of matter far from the center. The angular momentum transport process is now believed to be qualitatively understood in the context of magnetohydrodynamical calculations. The basic idea is called the magnetohydrodynamic instability involving a magnetic field with a component in the axial direction of the accretion disk (Balbus & Hawley, 1992). The material in the accretion disk interacts with each

other through the magnetic tension. The inner matter orbits faster than the outer matter at the beginning. Then due to the magnetic interaction, the inner element slows down, reduces its angular momentum, and moves to a smaller orbit. Instead the outer element speeds up, increases its angular momentum, and moves to a larger orbit. This process leads to a dynamically unstable situation and a plausible model of the accretion disk.

1.1.3 Torus

The AGN unification model generally invokes an obscuring dust structure with a toroidal geometry surrounding the central accretion disk, the so-called torus. In this scenario, AGN can be divided into two subgroups, type I and type II, depending on the observer's line of sight toward the central core and the BLR or obscured by the dust torus respectively.

This torus structure is suggested to have a range of geometrical thickness, with a scale height-radius relation of H/R $\sim$ 1 (Schmitt et al., 2001). It is expected to be located within the region dominated by the gravitational influence of the central black hole in parsec scale, according to the size of the BLR calculation by reverberation mapping and photoionization. The inner edge of the torus could be determined by the radial distance from the central engine where the dust reaches its sublimation temperature.

The structure of the torus tends to favor a clumpy rather than a smooth toroid (Elitzur & Shlosman, 2006). The origin of the torus is a question to be answered. One possibility is that the molecular clouds come from a clumpy wind structure, which is relatively cool and located in the outer region of the accretion disk (Kondratko et al., 2005). Alternatively, the molecular clouds might be accreted from the host galaxy (Krolik & Begelman, 1988). In any case, it is likely that the torus basically constitutes the prolongation of the accretion disk on the equatorial plane after the dust sublimation line, where the photons field coming from the accretion disk is so weak that dust grains can exist for a long time.

1.1.4 Broad-line and narrow-line regions

A distinguishing observational property of AGN is the presence of emission lines with different Doppler widths. The most prominent ones are the broad permitted lines, mainly hydrogen Balmer series lines Hα λ6563, Hβ λ4861, Hγ λ4340, Hδ λ4101, hydrogen Lyα λ1216, as well as magnesium Mg II λ2798 and carbon C IV λ1549, corresponding to velocities up to 10^4 km s^{-1}. Besides, there are forbidden or semi-forbidden emission lines which are much narrower, like oxygen [O II] λ3727 and [O III] $\lambda\lambda$4959,5007, nitrogen [N II] $\lambda\lambda$6548,6583, neon [Ne III] λ3869 and [Ne V] $\lambda\lambda$3346,3425, sulfur [S II] $\lambda\lambda$6716,6731, corresponding to velocities up to 10^3 km s^{-1}. This led to the respective designations of BLR and NLR in the AGN unified scheme. Depending on the redshift of a given AGN, these lines may not be observable in spectroscopy for a given bandpass.

The physical properties of the BLR are based on the photoionization model (Gaskell, 2009). The BLR gas is assumed to be in photoionization equilibrium, where the rates of photoionization and recombination are in balance. The ionization parameter can be

expressed as

$$\xi = \int \frac{F_\nu}{h\nu n_e c} d\nu, \tag{1.9}$$

where F_ν is the flux of a given line and n_e is the gas density. Typically, the gas temperature and density of the BLR are of order $T \sim 10^4$ K and $n_e \sim 10^9$ cm^{-3} respectively, which are determined by the observational ionization states. The BLR gas could exhibit an orbital motion around the central core. The large Doppler widths of the broad emission lines strongly suggest that the BLR resides deep inside the gravitational potential well, which is corroborated by reverberation mapping studies. Thus the BLR provides important insight into the central engine. The inferred BLR scales are of order light days to months for low-luminosity AGN and of order light years for high-luminosity AGN.

In the NLR, the gas is photoionized by the continuum radiation emitted from the central core, with the gas density of $n_e \sim 10^3$ - 10^6 cm^{-3}. The total mass of the NLR gas is estimated to be 10^6 $M_\odot$. The size of the NLR can provide a probe of the distribution of dust and gas in the central region of AGN. It is believed to occupy a much larger region as suggested by the lack of observable flux variations in the emission lines, extend to 10^2 - 10^4 pc and scale with the luminosity of some prominent forbidden lines (Bennert et al., 2004). Some observations support the influence of a jet or collimated outflow on the NLR structure (Kraemer et al., 2008).

1.1.5 Jet

A notable feature of AGN is the presence of relativistic jets emanating from the central nucleus in a fraction of sources, which is believed to be extremely energetic and highly collimated outflowing plasma structures launched from the central engine. The jets can exhibit a variety of observational appearances due to both intrinsic properties and projection effects. Their morphologies can appear short and irregular, or long and straight extending up to hundreds of kpc or even Mpc into space and retaining a remarkably high degree of collimation. Their apparent propagation velocities can be up to tens of times the speed of light, but sometimes, slower-moving, stationary, and even apparently reverse-moving features are seen.

The composition of AGN jets is an issue to be solved. It is generally accepted that the low-frequency (radio to X-ray) emission is synchrotron radiation of relativistic electrons in the jets. While for the origin of high-energy (X-ray to γ-ray) emission, there are two fundamental approaches referred to as leptonic models and hadronic models (Böttcher et al., 2013). In leptonic models, the jet radiation is assumed to be dominated by leptons (electrons). The high-energy emission is plausibly due to Compton scattering of low-energy photons by electrons producing synchrotron emission at lower frequencies. Any hadrons (protons) are likely to exist in the outflow, but not accelerated to sufficiently high energies to contribute to the radiative output. In hadronic models, both electrons and protons in the jets are accelerated to ultra-relativistic energies, and the energetic protons exceed the threshold of pion-photon production. The high-energy emission is dominated by

neutral pion decay photons $\pi^0 \rightarrow 2\gamma$, additionally synchrotron and Compton radiation from protons and secondary decay products. Current AGN jet studies favor the composition of a mixed lepton and hadron plasma. The leptons are responsible for the entire radiation and the hadrons comprise most of the kinetic energy (Sikora et al., 2009).

The formation of AGN jets is an uncertain issue. The conventional picture involves a twisting magnetic field perpendicular to the accretion disk. The interaction between the magnetic field and ionized material in the accretion disk leads to the collimation of outflow generally along the rotation axis of central core. Thus the jets emerge from each face of the accretion disk. The energy powering the jets involves the Blandford–Znajek mechanism (Blandford & Znajek, 1977), which requires a spinning black hole allowed for extracting energy. A numerical simulation invoking three-dimensional relativistic magnetohydrodynamics by Tchekhovskoy et al. (2011) supports this scenario. Their calculations lead to powerful outflows in the case of a spinning black hole. Furthermore, the fraction of available energy from the accretion flows onto the black hole directed into the jets increases with the presumed black hole angular momentum or spin.

1.2 The AGN family

In the AGN unification model, there are basically two intrinsic classes of AGN: radio-loud (RL) and radio-quiet (RQ), according to the presence of a relativistic jet originated from the vicinity of central black hole, while other observational differences would be explained by orientation effects. The classification of RL and RQ AGN is based on the radio-loudness parameter defined by Kellermann et al. (1989), which is the flux ratio between radio and optical bands $R_L = F_{radio}/F_{optical}$. Sources with $R_L > 10$ are considered as RL, while the others belong to RQ population. However, this dividing line $R_L = 10$ is not restricted and a little arbitrary. We recall that RL AGN do not have to be a bright radio sources but the radio to optical flux ratio is high, conversely RQ AGN are not necessarily faint or no radio emitters.

A recent work by Padovani (2017) argued that AGN should be classified based on physical differences rather than just an observational phenomenon. They defined two new classes of AGN: jetted AGN, which are characterized by strong relativistic jets, and non-jetted AGN, which also have jet structures but with weak power compared to those of jetted sources. The SED of non-jetted AGN has a cutoff at much lower energy than jetted AGN. Despite this, the radio-loudness parameter has been useful to separate physically different sources, as it provides an estimate of the amount of non-thermal radiation, particularly synchrotron emission, with respect to optical radiation in the SED.

The existence of an optically thick torus surrounding the nuclear region of AGN would absorb the radiation from it and thus hide it. Such a structure introduces a viewing angle parameter with respect to the line of sight, and is able to explain most of observed differences between various kinds of AGN. Depending on the viewing angles, AGN are also described as type I and type II objects. Type I AGN are observed face-on, with a small viewing angle, thus the BLR and NLR are both visible from the line of sight. This leads

to the broad permitted lines and the narrow forbidden lines appearing together in their optical spectra. Instead type II AGN are observed edge-on, with a large viewing angle. As the NLR lies further away from the central region than the BLR, hence the BLR is obscured by the torus and only the NLR is seen from the observers. This results in the broad lines missing and the permitted and forbidden lines both appearing as narrow in their optical spectra.

1.2.1 Seyfert galaxies

Seyfert galaxies are the most common class of AGN in the local universe, which were first defined by Seyfert (1943). The identification of Seyfert galaxy is based on the optical spectrum of central core showing highly ionized emission lines. Studying the spectra of Seyfert galaxies, Khachikian & Weedman (1974) found that Seyfert galaxies can be generally divided into two distinct types, Seyfert 1 (Sy1) and Seyfert 2 (Sy2), according to their relative widths of Balmer lines and forbidden lines. In Sy1 objects, the Balmer lines, mainly Hα, Hβ, Hγ, and Hδ, are very broad, having Doppler widths of order 10^3 - 10^4 km s^{-1}. While the forbidden lines, like [O II], [O III], [N II], [Ne III], [Ne V], and [S II], are narrower than the permitted lines, having Doppler widths of 500 km s^{-1} typically. In contrast, both the Balmer lines and the forbidden lines have similar narrow widths of order 10^2 km s^{-1} in Sy2 objects. Another spectroscopic distinction between Sy1 and Sy2 is the ionization level, with respect to their line ratio of [O III] λ5007 / Hβ λ4861, Sy1 settle at [O III]/Hβ < 3 while Sy2 stay in [O III]/Hβ > 3 (Caccianiga et al., 2008).

According to the AGN unification scheme, the broad Balmer lines arise from the BLR and the narrow forbidden lines come from the NLR. A closer inspection of Sy1 spectra shows that the Balmer lines have a broad and a narrow components, which reveals that the broad permitted lines in Sy1 spectra contain the radiation from both BLR and NLR. This can be explained by the AGN unified model very well. Sy1 are sources seen in small viewing angles, thus the radiation from BLR and NLR is visible from our line of sight. Instead Sy2 are sources seen in large viewing angles, hence the BLR is obscured by the torus and only the emission from NLR is visible for us. Another indication of the visibility of BLR in Sy1 is that the Fe II multiplets emission around 4570 Å in optical spectra is present in Sy1 but missing in Sy2.

The continuum emission of Seyfert galaxies is a superposition of the AGN core and the host galaxy. Sy1 generally exhibit a strong featureless continuum having a non-thermal origin, which distinguish them from the host galaxy emission with a characteristic of stellar absorption lines. On the contrary, the continuum emission in Sy2 is generally less dominant with respect to the host galaxy than in Sy1, which is a sign that the central core in Sy2 is obscured by the torus. Hence Sy2 are more difficult to find, usually longer exposure times are needed to separate the weak emission-line spectrum superposed on the stellar spectrum of the galaxy. Two examples of Sy1 and Sy2 spectra are showed in Fig. 1.2. In spite of the clear distinction between Sy1 and Sy2, intermediate objects, like Seyfert 1.2, 1.5, 1.8 and 1.9, are observed. These definitions are based on the relative width of Hβ line and

the ratio of broad and narrow components (Osterbrock, 1977). However, we noted that the subdivision of intermediate Seyfert galaxies is arbitrary as the signal-to-noise (S/N) of optical spectra is usually not enough to measure the line widths precisely.

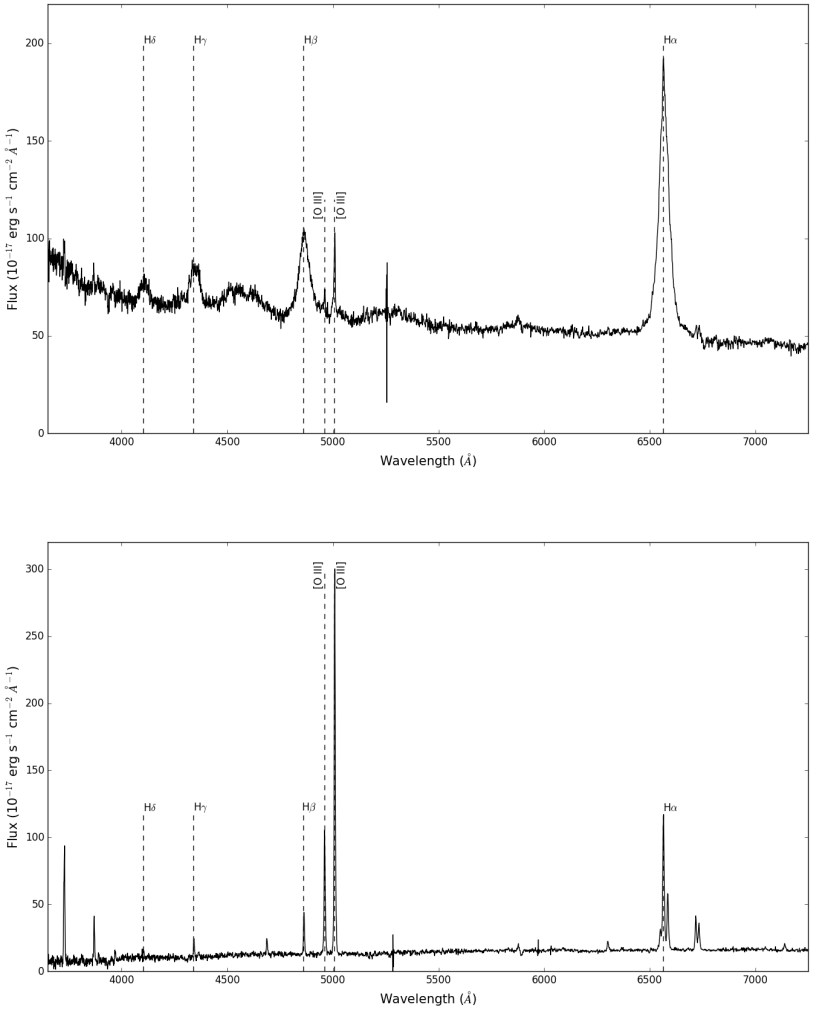

Figure 1.2: Two examples of Seyfert galaxies spectra. *Top panel:* Seyfert 1 spectrum SDSS J001335.38-095120.9. *Bottom panel:* Seyfert 2 spectrum SDSS J215649.51-074532.4. Both spectra are derived from the SDSS archive.

Seyfert galaxies are generally strong X-ray emitters. A distinction is made in the X-ray regime to discern Sy1 and Sy2 based on the intrinsic absorption measurement in the soft X-ray ($E < 2$ keV) band. Such intrinsic absorption indicates matter surrounding the central engine of AGN, and is measured as a column density of hydrogen n_H in the line of sight. In the AGN unification scheme, the differences between Sy1 and Sy2 result from the amount of absorbing material close to the central engine. Sy1 (and Seyfert 1.2, 1.5)

usually exhibit low absorption having $n_H < 10^{22}$ cm^{-2}. Conversely, Sy2 (and Seyfert 1.8, 1.9) are often highly absorbed sources with $n_H > 10^{22}$ cm^{-2}. Although some exceptions are known. Seyfert galaxies are typically weak radio emitters. However in some cases, they are detected in radio frequencies. This might be due to the non-thermal synchrotron radiation from a weak jet or star formation in the galaxies, which also contributes to the optical emission.

1.2.2 LINERs

Low-ionization nuclear emission-line regions (LINERs) are the low-luminosity tail of AGN filling the luminosity gap between Seyfert and non-active galaxies. Their central core might be accreting at a low efficiency compared to Seyfert galaxies. LINERs represent the link between Sy2 and H II regions as well. Since the optical spectra of these three types of objects are very similar, having narrow emission lines produced by the ionized gas, as shown in Fig. 1.3, in order to distinguish Sy2, LINERs and H II regions, Veilleux & Osterbrock (1987) presented several classification diagrams based on the line ratios measurement, as shown in Fig. 1.4. It is seen that different types of galaxies mostly occupy separated areas in the diagram of [O III] λ5007 / Hβ λ4861 versus [N II] λ6583 / Hα λ6563. Sy2 take [O III] / Hβ $>$ 3 area, while LINERs are in [O III] / Hβ $<$ 3 area. In comparison to H II regions, Sy2 and LINERs have stronger [N II] / Hα line ratios. Besides other line ratios, [S II] $\lambda\lambda$6716,6731 / Hα λ6563 and [O I] λ6300 / Hα λ6563, are also considered for a correct classification. However, it is controversial whether LINERs belong to the AGN population, due to the weak nuclear emission compared to the surrounding starlight, as it is often difficult to distinguish between the central core emission and the host galaxy contribution in LINERs.

1.2.3 Quasars

Quasars were discovered in the late 1950s and early 1960s by large sky surveys using radio telescopes. They are called quasi-stellar radio sources or quasars, as their optical images look like blue stars. Their optical spectra reveal strong emission lines like Seyfert galaxies, but with significant redshift which mean that these sources are more distant than nearby Seyfert galaxies. In order to separate these two kinds of AGN, an arbitrary criterion was introduced, Seyfert galaxies with an absolute magnitude on B-band brighter than -23 mag ($B <$ -23) are referred to as Quasars (Schmidt & Green, 1983). Quasars can be divided into type 1 and type 2 objects as well as Seyfert galaxies, according to the width of permitted lines in their optical spectra. Indeed type 2 Quasars are easier to escape detection than type 1 Quasars, in particular at high redshifts. Quasars are potentially bright X-ray sources like Seyfert galaxies. It is known that Quasars and Seyfert galaxies are different manifestations of the same underlying phenomenon. Compared to Seyfert galaxies, Quasars are more luminous and located at farther distances. Besides, Seyfert galaxies are generally hosted in spiral galaxies, while Quasars are typically hosted in elliptical galaxies. A possible

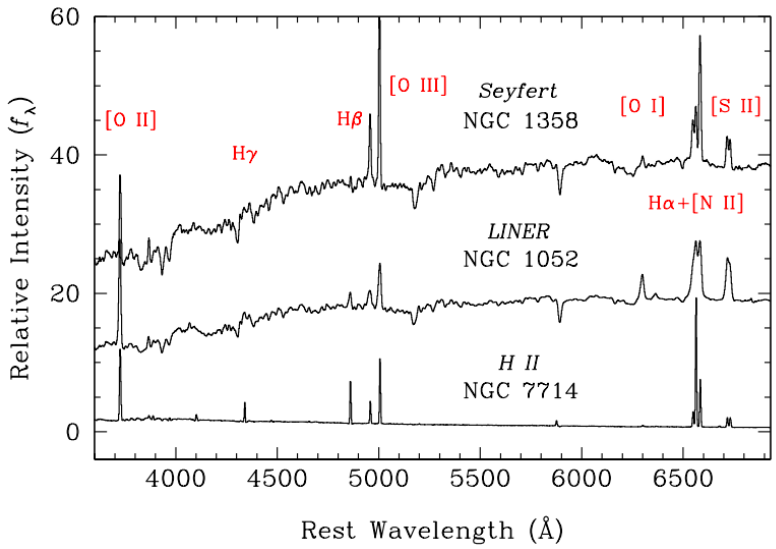

Figure 1.3: Three examples of optical spectra showing the differences between Sy2, LINER, and H II region.

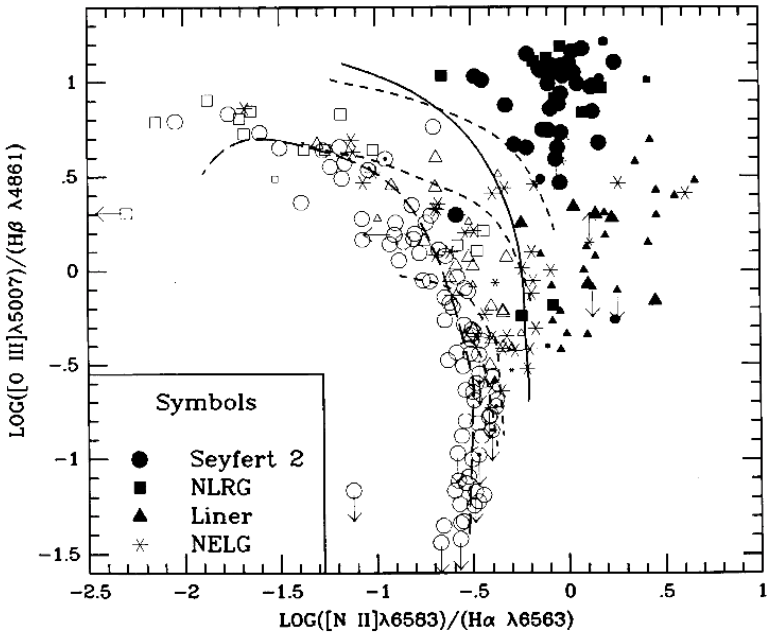

Figure 1.4: Classification diagram using reddening-corrected [O III] λ5007 / Hβ λ4861 vs. [N II] λ6583 / Hα λ6563. Open circles indicate H II regions, open squares are H II galaxies, and open triangles are starburst galaxies. The other symbols represent AGN as indicated in the plot, NLRGs and NELGs are narrow-line radio galaxies and narrow-emission-line galaxies respectively. The solid curve divides AGN from H II region-like objects. Figure is from Veilleux & Osterbrock (1987).

interpretation is that Seyfert galaxies formed recently in the cosmic time whereas Quasars formed at the early times of the universe.

A fraction of Quasars are RL (15%), while the majority of them are RQ (85%). RL Quasars are more easily discovered than RQ objects, because of their strong radio emission which is a signature of powerful relativistic jets through synchrotron radiation. Moreover, RL Quasars tend to be more massive and more luminous than RQ sources. RL Quasars are further classified as Flat Spectrum Radio Quasars and Steep Spectrum Radio Quasars, according to whether their radio spectra are flat or steep toward higher frequencies in GHz range. The former ones have compact radio structures, instead the latter ones are dominated by extended radio lobes emission. The mechanism of radio emission in RQ Quasars is not well understood yet. One possibility is that the jet in RQ sources is less powerful and non-relativistic compared with RL sources (Ulvestad et al., 2005). An alternative explanation is that the origin of synchrotron emission might be due to the magnetically heated coronae (Laor & Behar, 2008) or the particles accelerated in shocks occurring in accretion flows (Ishibashi & Courvoisier, 2011).

1.2.4 Blazars

Blazars are a special class of AGN in which the relativistic jets are pointing at the observers or very close to the observers' line of sight. They are prominent emitters in the whole electromagnetic spectrum from radio frequencies up to Very High Energies (VHE) above 1 TeV, and show dramatic variability reported on time scales from years down to less than a day. Blazars are divided into Flat Spectrum Radio Quasars (FSRQs) and BL Lacertae Objects (BL Lacs), according to their optical spectral line properties. FSRQs exhibit strong broad emission lines overlapped with a featureless power-law continuum in their optical spectra. These sources are extremely bright and located in large cosmological distances. On the contrary, the optical spectra of BL Lacs are virtually dominated by a simple non-thermal continuum, showing no prominent emission and absorption lines. Thus it is difficult to obtain spectroscopic redshifts for BL Lacs. A criterion on emission lines is applied to tell them apart, FSRQs have EW > 5 Å whereas BL Lacs have EW < 5 Å. This criterion is somewhat arbitrary, because the continuum emission of Blazars is variable, and lines can become visible during a low jet activity state and become invisible during a high jet activity state (Foschini, 2012). Two examples of FSRQ and BL Lac spectra are showed in Fig. 1.5.

One property to identify Blazars is throughout their large variations in all frequency bands. The variability might be intrinsic and due to intensity variations of the relativistic jets, or caused by different amounts of absorption in the vicinity of emission region. However, this issue is still under debate. Other method is finding sources with strong radio emission and/or high X-ray flux, called radio-selected Blazars and/or X-ray-selected Blazars respectively. Since these selection criteria strongly depend on the features and observations of the sources, different types of Blazars are currently distinguished by the characteristics of their overall SED.

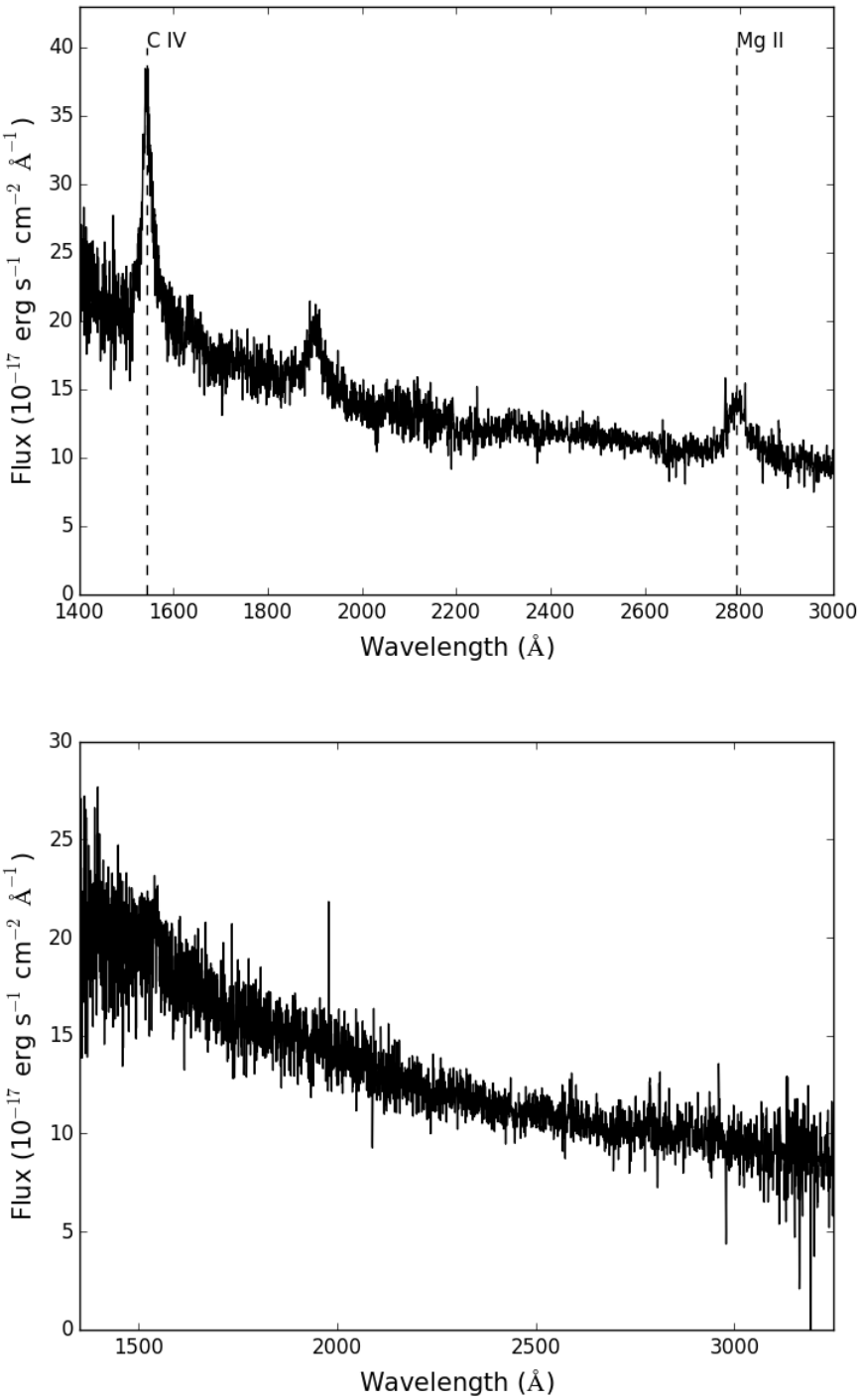

Figure 1.5: Two examples of Blazars spectra. *Top panel:* FSRQ spectrum 3FGL J1131.4+3819. *Bottom panel:* BL Lac spectrum 3FGL J1247.0+4421. Both spectra are derived from the SDSS archive.

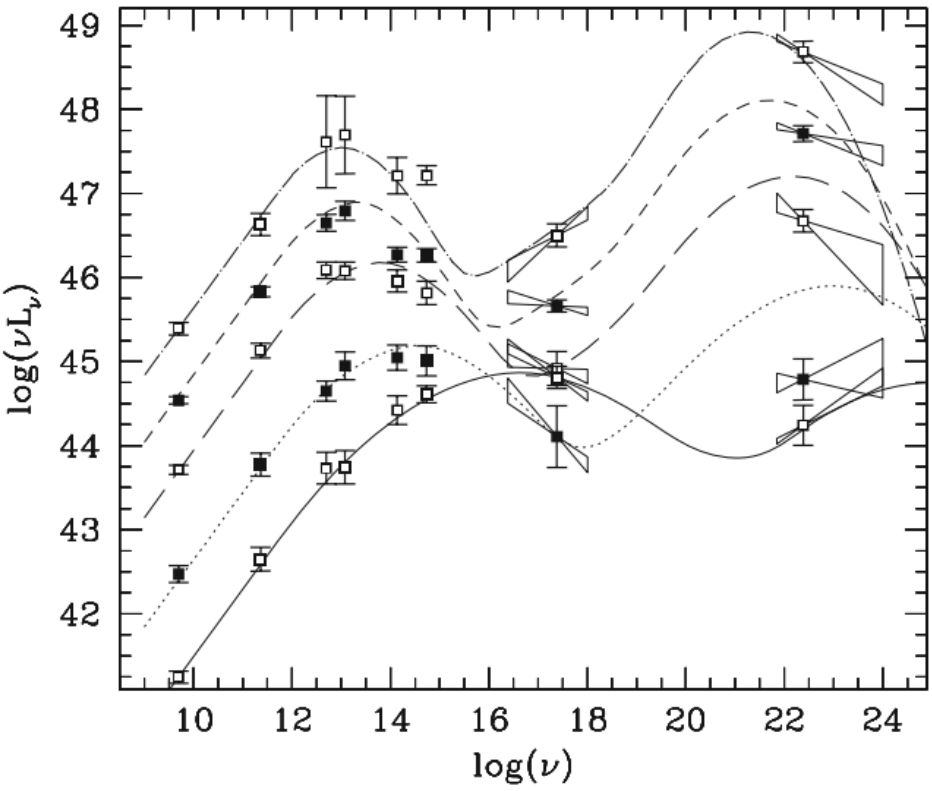

Figure 1.6: The Blazar sequence. Figure is from Fossati et al. (1998).

It is interesting that the SED of Blazars is double-peaked in the $\log \nu$ - $\log \nu L_\nu$ plane. The first peak is produced by the synchrotron radiation and the second peak is dominated by the inverse Compton radiation. The most powerful objects, like FSRQs, have relatively low peak frequencies, in radio for synchrotron branch and in γ-ray for inverse Compton branch. Instead the less powerful objects, like BL Lacs, show high peak frequencies, in X-ray for synchrotron branch and in VHE for inverse Compton branch. This is the so-called Blazar sequence (Fossati et al., 1998) suggesting that, the more powerful the Blazars appear to be, the lower the peak frequencies of synchrotron and inverse Compton radiations, as shown in Fig. 1.6. Thus historically, FSRQs are radio-selected Blazars whereas BL Lacs are X-ray-selected Blazars. This can be explained by different cooling processes of relativistic electrons depending on if the environment is photon-rich (FSRQs) or photon-starving (BL Lacs), which is the main factor of regulating the electromagnetic radiation (Ghisellini et al., 1998; Foschini, 2017). In case of the most powerful FSRQs, the contribution from the external radiation to the electron cooling is the greatest. The emission by synchrotron and external Compton (EC) processes can not extend to frequencies higher than infrared and VHE bands respectively. Whereas for the less powerful BL Lacs, the external radiation is weak, hence the electron cooling is less dramatic. The electrons can reach energies high enough to produce synchrotron emission peak at X-ray band and synchrotron self-Compton

(SSC) emission peak at VHE band.

1.2.5 Radio galaxies

Radio galaxies are a class of AGN that exhibit prominent relativistic jets bright in radio. Their central core, however, is likely to be the same as in Quasars and Seyfert galaxies. Radio galaxies are morphologically classified as two subgroups according to the appearance of extended radio emission. The low-luminosity Fanaroff–Riley class I (FR-I) galaxies exhibit a rather compact emission arising from close to the core. The high-luminosity Fanaroff–Riley class II (FR-II) galaxies are dominated by the radio lobes structure and most of the emission appears to come from the far end of extended emission (Fanaroff & Riley, 1974). Two examples of FR-I and FR-II radio images are shown in Fig. 1.7.

The FR-I galaxies show a jet-dominated radio structure. In contrast, the FR-II objects have a lobe-dominated radio morphology, whose jet is originating at the central core then terminating in the large lobes. The radio jets in FR-I might be not so powerful as in FR-II, thus the jets in FR-II are more collimated and confined over a larger distance than in FR-I. The radio structure can extend out to hundreds of kpc from the core, far beyond the host galaxy. The radio spectra of core, jet, and lobes are non-thermal and featureless, hence it is thought to be produced by synchrotron radiation.

The two radio lobes are supposed to have equivalent intrinsic brightness, but the jet can appear as single-sided or double-sided. An example of single-sided jet is displayed in Fig. 1.8. The reason might be that the visible jet component is Doppler boosted toward the observers, the non-visible part, instead, is pointing away from us. This single-sided jet can give an estimation of the outflow speed under the assumption of a intrinsically symmetric FR-II. Such as the morphology, speed, and power of the jets on the both sides of the central engine are supposed to be the same. The only difference will be caused by the different Doppler enhancement of the radiation toward the observers. The observed flux ratio of the approaching jet (f_+) to the receding jet (f_-) can be derived from the Doppler factors

$$\frac{f_+(\nu)}{f_-(\nu)} = \left(\frac{1+\beta\cos\theta}{1-\beta\cos\theta}\right)^{2+\alpha}, \tag{1.10}$$

where α is the spectral index of the observed continuum, $\beta = v/c$, and θ is the angle of the jet with respect to the line of sight. Thus we can have an estimate of the speed of the jet toward us.

However, there are many open issues about the jets. How the jets are so well collimated very close to the central engine? How the jets are confined over a large distance, in some cases hundreds of kpc? What kinds of charged particles dominate the jets, electrons, positrons, protons, or a mix of them? Currently, the mixed plasma is regarded as the most likely configuration, since electrons and positrons can be accelerated more easily than protons simply because of their lower mass, whereas heavier particles are more likely to be stable and confined out to large distances.

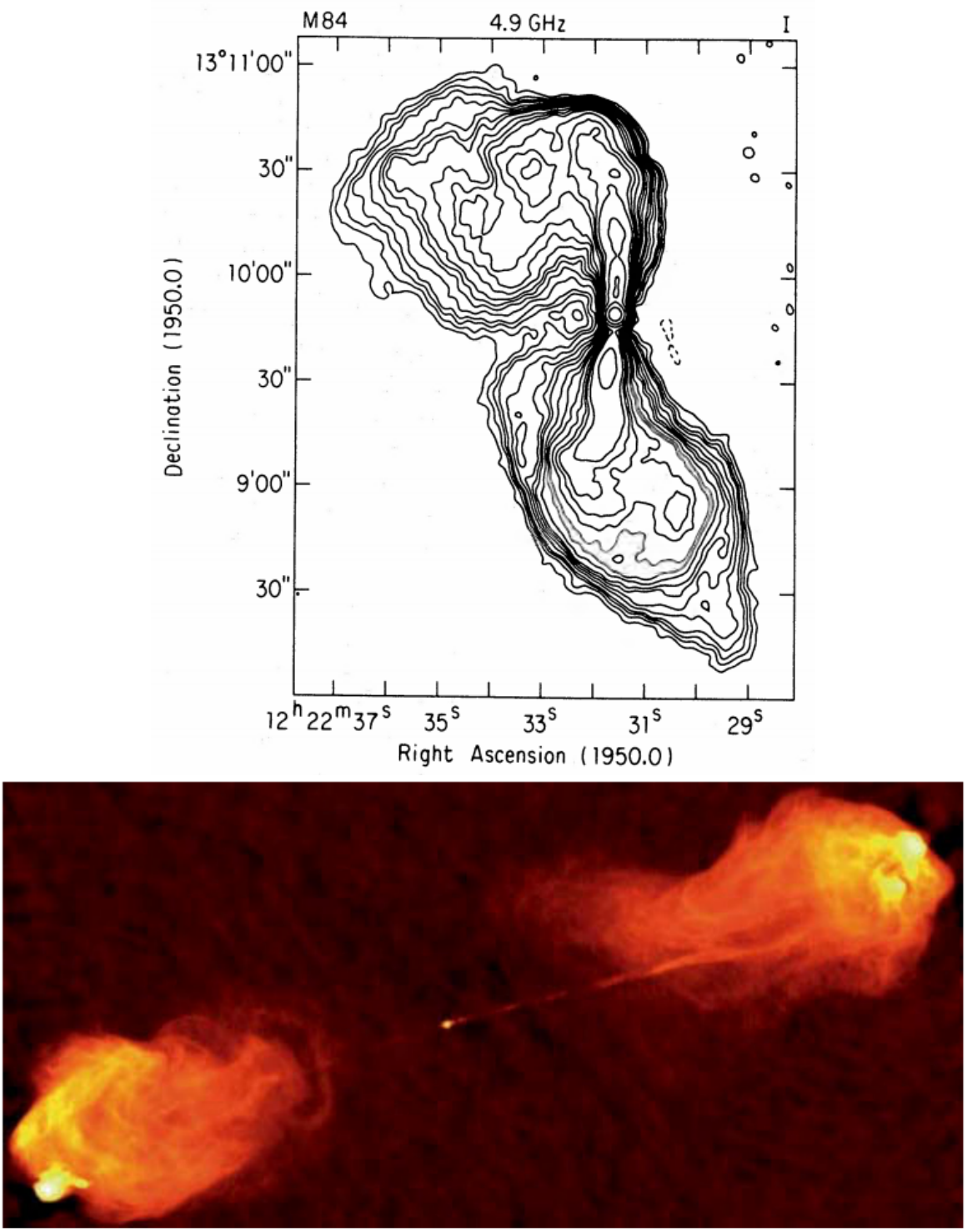

Figure 1.7: Two examples of radio galaxy images. *Top panel:* FR-I. Figure is from Laing & Bridle (1987). *Bottom panel:* FR-II. Figure is from Carilli & Barthel (1996).

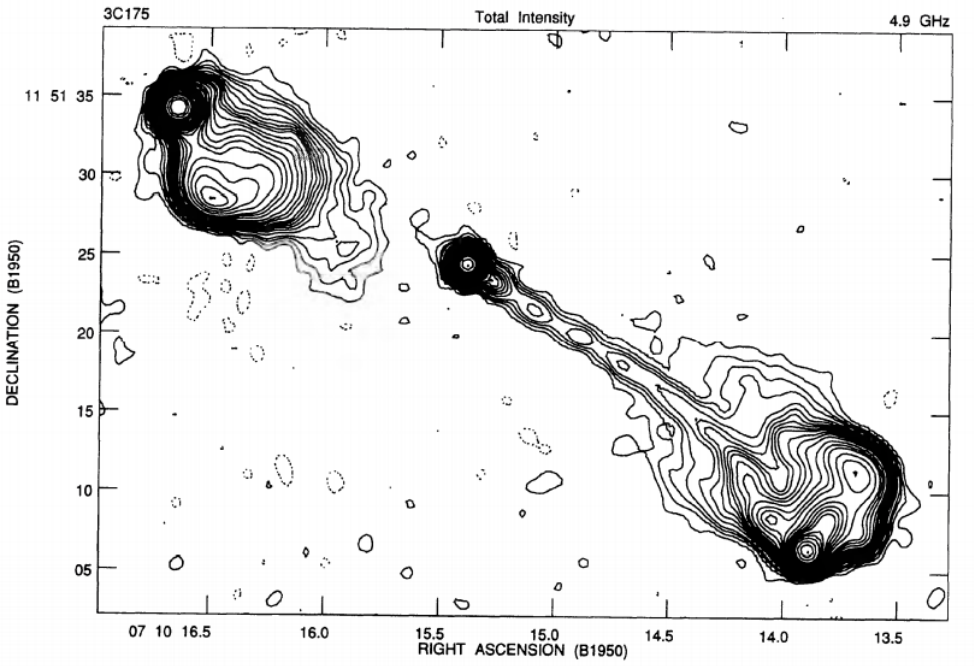

Figure 1.8: An example of radio galaxy image showing two lobes but single-sided jet. Figure is from Bridle et al. (1994).

1.3 The multi-wavelength properties of AGN

1.3.1 Radio

The radio emission in AGN is produced by synchrotron radiation occurring when charged particles are accelerated in magnetic field. The radio images generally consist of compact and extended components. The compact structure is the central core of AGN unresolved at arcsec scales, whose position is believed to be coincident with the central black hole. On the contrary, the extended structure is caused by the jet interacting with surrounding environments, and in some cases is affected by the relativistic beaming. The radio spectra have a power-law distribution of $F_\nu \propto \nu^{-\alpha}$, where F_ν is the flux density at frequency ν and α is the spectral index, representing the non-thermal radiation. The radio spectrum of compact emission is usually flatter than that of extended emission.

The process of launching the plasma jets is not well understood. One possibility is that the magnetic field around the nuclear region of AGN provides a mechanism to convert gravitational and rotational energies into kinetic energy and produce high-velocity outflows perpendicular to the accretion disk. This implies that the radio emitting plasma is accelerated to a relativistic speed in the magnetic field, with a Lorentz factor of

$$\Gamma \equiv \frac{1}{\sqrt{1-\frac{v^2}{c^2}}} \sim 10^4, \tag{1.11}$$

where v and c are the velocities of plasma and light respectively. Since the plasma must be neutral, in addition to electrons, it should also contain either protons or positrons. However, it is hard to determine the actual composition of synchrotron radiation directly from radio observations.

1.3.2 Optical

The optical emission is a direct view of the nuclear continuum of AGN. The optical spectroscopy is the main tool of AGN classification, as well as redshift identification and thus distance information. Their spectra generally exhibit a power-law distribution originated from synchrotron radiation. A large excess often extending into the ultra-violet (UV) band superposed on the underlying power-law continuum, is the so-called big blue bump. It is believed to have a thermal origin from the accretion disk. If jets are present, in some cases, they could also contribute to the optical emission and make the optical spectra variable.

A pronounced feature of various AGN is the presence of emission lines in the optical spectroscopy. These permitted and forbidden lines emanate from material surrounding the central black hole (BLR and NLR), and arise from photoionization by the non-thermal continuum radiation. Hence, there are strong luminosity correlations between emission lines and continuum, which is useful for tracing the central engine properties. However, some AGN do not exhibit emission lines in their optical spectra, or their emission lines are weak. This could be related to the activity of the continuum (Foschini, 2012). If the source is in a high state, the bright continuum will overwhelm the emission lines, hence the emission lines are less prominent. In a low state, instead, the emission lines will be visible under the weak continuum.

1.3.3 X-ray

The X-ray emission originates in the central engine of AGN, where the accretion disk surrounding the black hole produces a thermal radiation through accretion processes. The low-energy photons are scattered to higher energies by relativistic electrons residing in the corona above the accretion disk. Thus they gain in energy and radiate in X-ray band through inverse Compton scattering (Haardt & Maraschi, 1993). The soft photons upscattered in inverse Compton radiation are believed to come from the cool thick accretion disk with a temperature of $kT < 50$ eV, and the relativistic electrons residing in the corona have $kT \sim 100$ keV. The X-ray spectra have a power-law continuum with a photon index of $\Gamma_X \simeq 2$ ($\Gamma = \alpha + 1$) extending up to a few hundreds keV. As the temperature of the accretion disk and the energy distribution of the relativistic electrons are limited, the resulting inverse Compton spectra have a high-energy cutoff. A model X-ray spectrum of AGN showing the contribution of various spectral features is shown in Fig. 1.9.

The primary X-ray emission could be reprocessed by reflecting material giving rise to reflection features. The reflecting material might be the accretion disk, the BLR, and the molecular torus whose location is a question of debate. One of the reflection features is the

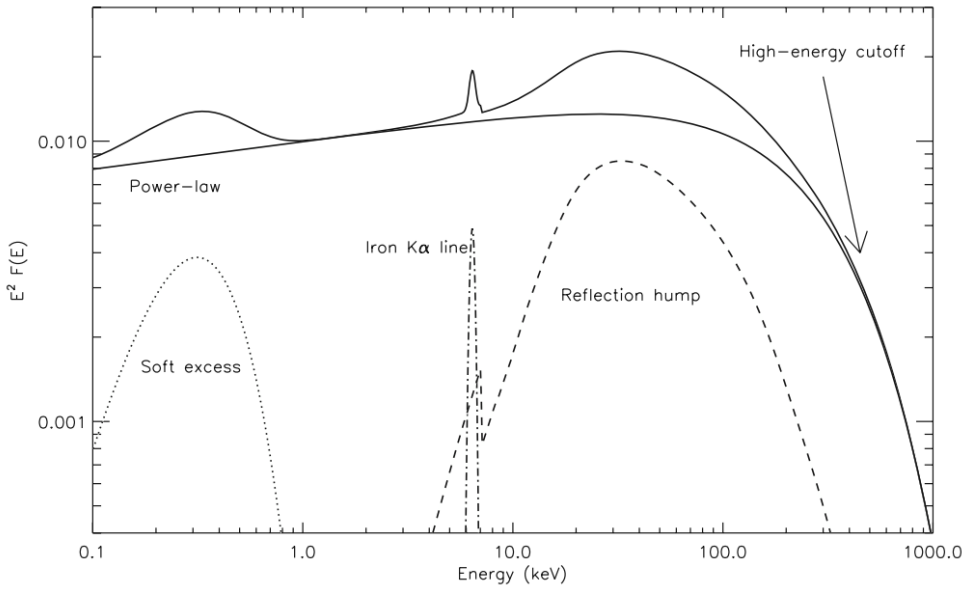

Figure 1.9: A model X-ray spectrum of AGN. Figure courtesy of Claudio Ricci.

reflection hump observed in the hard X-ray spectra, peaking at around 30-40 keV where the reflection efficiency reaches its maximum. This reflection hump is produced only if the reprocessing material is colder than $T \simeq 10^6$ K and Compton thick with a column density of $n_H > 10^{24}$ cm^{-2}. The strength of the reflection hump depends on the material's geometry, chemical composition, and orientation with respect to the line of sight. Its measurement is difficult, as the modeled strength of this component is closely linked to the intrinsic absorption measured at softer X-ray, the spectral slope of underlying continuum, and the high-energy cutoff, which are not well constrained in many cases.

Another notable reflection feature of the reprocessed radiation is the Fe Kα fluorescence line, having an energy of $E = 6.4$ keV at the rest frame and an equivalent width of EW ~ 50 eV on average. This iron emission line can be produced by both Compton thin and thick material, thus it is usually treated as a probe of the reflection process. The Fe Kα line is likely to be arising from cold gas in the vicinity of central engine illuminated by the X-ray continuum (Zdziarski et al., 1994). The X-ray photons entering the cold gas can be Compton scattered by free or bound electrons, or absorbed following fluorescent line emission. Moreover, they can also be absorbed via the Auger de-excitation, which either destroys the photons and scatters them out of the gas, or reprocesses them into fluorescent line photons escaping the gas (Fabian et al., 2000). In principle, the fluorescence line should be narrow. Hence the broadened Fe Kα line indicates relative movement toward the observers or turbulence in the accretion disk (Pariev & Bromley, 1998). In addition, an asymmetric line profile might be shaped by the relativistic effect or the disk wind model.

In the soft X-ray ($E \lesssim 2$ keV) spectra, a component observed over the power-law continuum is the soft excess. It has a nearly constant temperature of $kT \simeq 0.1$-0.2 keV, regardless of the mass of black hole and the luminosity of AGN. The origin of the soft excess

is still an open issue. There are three competing models to explain the soft excess: an additional Comptonization component (Dewangan et al., 2007), blurred reflection from an ionized disk (Crummy et al., 2006), and smeared absorption by an ionized wind (Gierliński & Done, 2004; Done, 2007).

1.3.4 γ-ray

In the γ-ray sky, AGN are rather dim sources compared to the bright galactic sources and do not show lines in their γ-ray spectra due to the lack of enough γ-ray photons and the poor resolution of γ-ray detectors. Seyfert galaxies are not expected to be detectable in γ-ray but with some exceptions. Their X-ray emission, which is dominated by inverse Comptonization of UV photons from the accretion disk being up-scattered on relativistic electrons, should fall off rapidly beyond 100 keV. Blazars are the main γ-ray emitting sources in the AGN regime. Such beamed sources can radiate much higher energy photons, as charged particles in the relativistic jets providing energy for inverse Compton up-scattering can have much higher energies than thermal electrons close to the accretion disk. Apart from Blazars, γ-ray emission is also detected from radio galaxies, which might be the result of a misaligned jet.

However, identifying γ-ray sources is a challenging task. This is simply due to the poor position determination of γ-ray detectors, which result in many possible counterparts in the uncertainty circle, in particular for faint sources. One way to identify γ-ray sources is cross-matching the counterparts in both radio and X-ray bands, as γ-ray sources should be sufficiently powerful to radiate energy in all frequencies. With the *Fermi* Large Area Telescope (LAT) launched in 2008, thousands of Blazars have been detected. FSRQs exhibit rather steep spectra in the *Fermi* LAT energy band with a photon index of $\Gamma_\gamma \sim 2.5$, while the γ-ray spectra of BL Lacs are relatively flat having $\Gamma_\gamma \sim 2$. This reveals that the inverse Compton branch of FSRQs generally lies at lower energies than that of BL Lacs. Besides, radio galaxies show γ-ray spectra resembling those of FSRQs.

Chapter 2

Narrow-line Seyfert 1 galaxies

Narrow-line Seyfert 1 galaxies (NLS1s) are a peculiar class of AGN. They were first discovered in 1978 and drew curiosity due to their unusually optical spectral properties. They have Sy1-like spectra with narrow permitted lines comparable to those seen in Sy2 (Davidson & Kinman, 1978; Koski, 1978; Phillips, 1978). Whereas the presence of strong Fe II emission indicates that they are type I objects (Sargent, 1968; Phillips, 1976, 1978). The first classification of NLS1s was given in 1985 by Osterbrock & Pogge (1985). Their Hβ lines originating in the BLR, have a full width at half maximum of FWHM (Hβ) < 2000 km s^{-1} and a flux ratio of [O III]λ5007 / Hβ < 3 (Osterbrock & Pogge, 1985; Goodrich, 1989). Most of their optical spectra show strong Fe II multiplets emission, which is a sign that the BLR and the accretion disk are visible (Mullaney & Ward, 2008; Pogge, 2011). An example of NLS1 optical spectrum is showed in Fig. 2.1.

The narrowness of permitted lines in NLS1s are commonly interpreted as a small Doppler broadening due to a low rotational velocity of the gas in the BLR around a relatively undermassive central black hole compared to broad-line Seyfert 1 galaxies (BLS1s) (Mathur, 2000; Grupe, 2000). Estimating by the reverberation mapping, the central black hole masses are in the ranges of $M_{BH} \sim 10^{6-8} M_{\odot}$ for NLS1s and $M_{BH} \sim 10^{7-8} M_{\odot}$ for BLS1s typically (Järvelä et al., 2015; Cracco et al., 2016; Chen et al., 2018b). Since the bolometric luminosity of NLS1s is comparable to that of BLS1s, a low black hole mass corresponds to a low Eddington luminosity and thus a high Eddington ratio from Equations (1.4) and (1.5). This suggests that NLS1s have a high accretion luminosity and thus a high physical mass accretion rate following Equation (1.3). Hence, NLS1s are accreting in an efficient process comparable to that of FSRQs (Ghisellini et al., 2010) and close to the Eddington limit (Boroson & Green, 1992; Collin & Kawaguchi, 2004). Consequently, a small massive black hole suggests that NLS1s are likely to be a young and fast-growing phase of AGN (Mathur, 2000; Grupe, 2000). In this scenario, NLS1s might be different with respect to BLS1s, as suggested by their different large-scale environments: NLS1s preferably reside in less dense environments than BLS1s (Järvelä et al., 2017).

Another possible interpretation is that the narrowness of Hβ lines in NLS1s might be due to the pole-on orientation of a disk-like BLR, which prevents us from seeing any

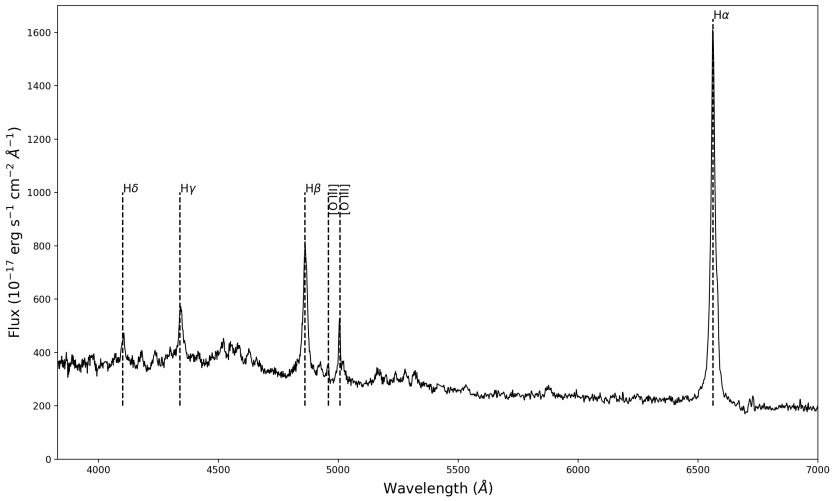

Figure 2.1: An optical spectrum of NLS1 (6dF J0039159-511702) derived from the 6dFGS archive.

Doppler broadening (Decarli et al., 2008). In this case, the low black hole mass of NLS1s is not real, but only an inclination effect. A study by Baldi et al. (2016) revealed that the Balmer line width will be broader in the polarized spectrum yielding a larger black hole mass. Hence, we can not exclude the possibilities that the BLR has a flattened disk-like geometry, and the orientation influence the width of the Balmer lines and likely account for the observed black hole mass deficit in NLS1s Shen & Ho (2014); Marziani et al. (2018).

It is common that AGN with high Eddington ratios, such as NLS1s, generate powerful outflows or winds by the radiation pressure from the accretion disk (Proga et al., 2000). These outflows are generally associated with the presence of asymmetric [O III] lines, which can be decomposed in two distinct components (Greene & Ho, 2005a). The narrow component is the line core, typically having the same redshift as the whole galaxy. The broad component is the blue wing usually connected with a gas outflow in the NLR and blueshifted with respect to their rest-frame wavelength (Zamanov et al., 2002; Marziani et al., 2003). The mechanism of the [O III] shift is not well understood. A common hypothesis is that the blueshift is generated by the strong winds from the accretion disk (Komossa et al., 2008). Alternative possibility is that a powerful jet can affect the gas kinematics in the NLR and induce a blueshift in these lines (Berton et al., 2016).

In the X-ray regime, NLS1s display extreme behaviors. They exhibit fast variability, typically on short time scale less than one day (Boller, 2000), as expected for the small black hole mass and high accretion rate (Ponti et al., 2012). In the soft X-ray band (below 2 keV), NLS1s show strong soft X-ray excess above the prediction of a single power-law (Boller et al., 1996). The origin of the soft X-ray excess is still unclear. An explanation is the low temperature optically thick Comptonization model, which includes an additional cool Comptonizing component from an inner disk producing the soft excess (Gierliński &

Done, 2004; Done et al., 2012). Another one is the relativistically blurred photoionized reflection from an inner accretion disk, which reproduces the emission expected from an optically thick photoionized disk around a black hole (Ross & Fabian, 2005; Crummy et al., 2006). Both models fit the spectra very well in the X-ray range, thus it is difficult to tell them apart. In the hard X-ray band (2-10 keV), NLS1s generally have steeper intrinsic spectra than BLS1s (Brandt et al., 1997). This might suggest that photons from the soft excess of NLS1s could Compton cool the coronae, which create lower temperature and more diffuse coronae than in BLS1s and thereby steepen the hard X-ray continua of NLS1s (Maraschi & Haardt, 1997).

Some NLS1s exhibiting extremely complex features around Fe K-shell at 6-8 keV are classified as complex NLS1s (C-NLS1s), while the others are described as simple NLS1s (S-NLS1s), whose 2-10 keV spectra do not strongly deviate from a single power-law continuum (Gallo, 2006). The same authors proposed that C-NLS1s are in a low X-ray flux state, whereas S-NLS1s are in a normal X-ray flux state. However, a research by Jin et al. (2017a,b) proposes a global picture for the structure of a super-Eddington accretion flow where the inner disk puffs up, shielding much of the potential NLR materials, and appearing as an inclination effect with respect to the clumpy disk wind, as shown in Fig. 2.2. In this picture, simple and complex NLS1s can be interpreted within the same accretion flow scenario but with different viewing angles. The inclination of S-NLS1s is low and the line of sight is unobscured showing original X-ray emission produced by the coronae. Instead, C-NLS1s are those seen at large viewing angles and the line of sight is intercepted by absorption materials.

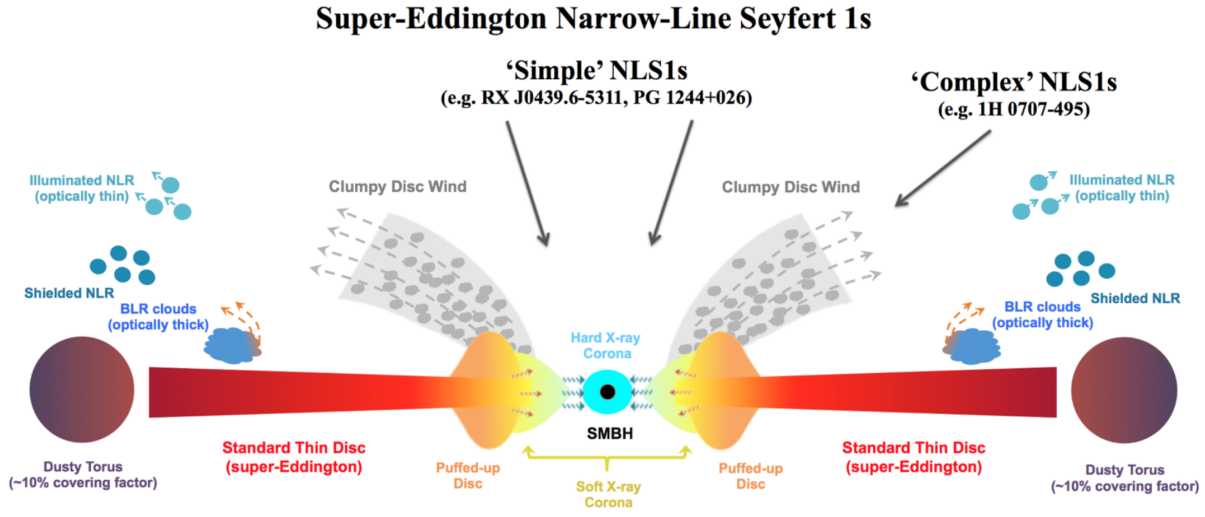

Figure 2.2: An inclination scenario of simple and complex NLS1s. Figure is from Jin et al. (2017b).

A fraction of NLS1s are detected at radio frequencies. Among the radio-detected NLS1s, only 7% of them are RL and 2.5% of them are very RL ($R_L > 100$), the majority of them are RQ (Komossa et al., 2006). The RL fraction of NLS1s is half of that of Quasars (15%)

(Kellermann et al., 1989). However, this fraction strongly depends on the redshift since it appears to be lower in the nearby universe (Cracco et al., 2016), and on the large-scale environment as it tends to be higher with increasing large-scale environment density (Järvelä et al., 2017). Multi-frequency studies of NLS1s show that RL sources have a higher redshift, more massive black hole, and larger luminosity than RQ sources. RL NLS1s are more likely to launch a powerful relativistic jet, which is a predominant origin of the radio, optical, and partially X-ray radiation. Instead, RQ NLS1s do not host a jet or the jet is very weak, radio emission is likely to originate from star formation processes, optical and X-ray emission come from the inner region of AGN (Järvelä et al., 2015).

Assuming the flux density and spectral index convention of $F_\nu \propto \nu^{-\alpha}$, RL NLS1s can be divided into two subclasses according to the radio spectral index α, flat-spectrum RL NLS1s ($\alpha < 0.5$) and steep-spectrum RL NLS1s ($\alpha > 0.5$). In general, flat-spectrum RL NLS1s have a compact radio morphology, high luminosity, and high brightness temperature (Gu & Chen, 2010; Doi et al., 2012). These Blazar-like physical characteristics suggest that flat-spectrum RL NLS1s might be the young, low-mass, and low-luminosity analogs of FSRQs (Foschini et al., 2015). Besides, steep-spectrum RL NLS1s often show an intermediate or extended morphology, lower luminosity, and lower brightness temperature with respect to flat-spectrum RL sources, although remain brighter than RQ sources. Conversely, RQ NLS1s exhibit a faint diffuse emission surrounding an unresolved core (Berton et al., 2018). At present, it is not clear how to include NLS1s in the orientation-driven AGN unification model (Antonucci, 1993; Urry & Padovani, 1995). If the young scenario is true, NLS1s are young AGN that are still growing, their jets and radio lobes might have not yet developed and might be not as powerful as Blazars. Therefore, they can appear as flat-spectrum RL NLS1s when observed along their jets at small angles, and as steep-spectrum RL NLS1s when observed at intermediate angles. When observed at large angles but remain unobscured by the torus, their radio emission is almost invisible for current radio facilities, thus they appear as RQ NLS1s (Berton et al., 2015, 2017). However, it is worth mentioning that a large number of jetted NLS1s are hidden in the radio-silent population, as suggested by Lähteenmäki et al. (2018). An orientation-driven AGN unification model considering young and old sources is showed in Fig. 2.3.

The discovery of γ-ray emission from RL NLS1s detected by the *Fermi* LAT confirmed that NLS1s are the third class of AGN emitting γ-ray from relativistic beamed jets, in addition to Blazars and radio galaxies (Abdo et al., 2009a,b,c; Foschini et al., 2011, 2015; Yao et al., 2015; Liao et al., 2015; D'Ammando et al., 2015, 2016; Paliya & Stalin, 2016; Berton et al., 2017; Paliya et al., 2018; Lähteenmäki et al., 2018; Yao et al., 2019). Indeed, radio images from the Very Long Baseline Array (VLBA) observations of several NLS1s show Blazar-like parsec-scale radio jets having very compact radio morphology, flat or inverted radio spectra, high brightness temperatures, and a significant degree of polarization (Abdo et al., 2009a,b; Gu et al., 2015; Lister et al., 2018). Moreover, radio monitoring campaigns reveal that they display fast and intensive variability, which is commonly seen in Blazars (Foschini et al., 2012; Angelakis et al., 2015; Fuhrmann et al., 2016). In some cases, an apparent superluminal motion is also observed (Lister et al., 2013, 2016, 2019). These findings indicate the presence of relativistic jets and pose a challenging question about the

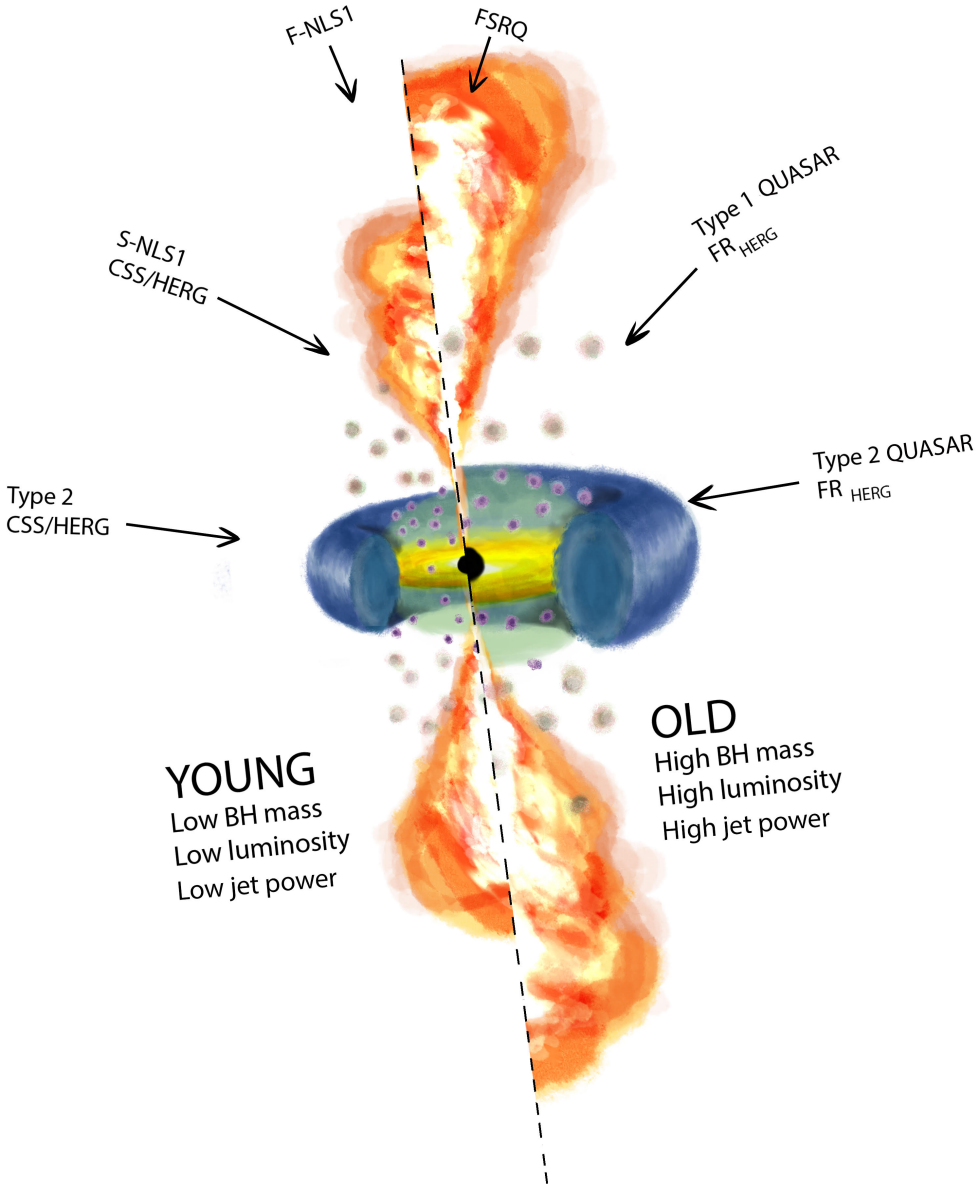

Figure 2.3: An orientation-driven AGN unified scheme considering young and old sources. Figure is from Berton et al. (2017).

generation and evolution of the jet system in NLS1s harboring a relatively undermassive black hole. The physical properties of NLS1s are different from those of Blazars and radio galaxies. The central black hole masses of NLS1s are on average one to two orders of magnitude lower than those of Blazars and radio galaxies having $M_{BH} \sim 10^{8-10} M_{\odot}$ (Mathur, 2000). This difference might be due to a projection effect in the inclination scenario. Moreover, NLS1s are generally hosted in spiral galaxies (Deo et al., 2006; Järvelä et al., 2018), while Blazars and radio galaxies are both typically hosted in elliptical galaxies

(Sikora et al., 2007).

It is interesting that γ-ray NLS1s typically belong to the flat-spectrum RL NLS1s population, and multi-wavelength follow-up studies provide evidences supporting the similarity of γ-ray NLS1s with Blazars, in particular with FSRQs (Foschini et al., 2015; Paliya et al., 2019). The broadband SED of γ-ray NLS1s is modeled by a simple one-zone leptonic emission model and exhibit behaviors resembling FSRQs (Ghisellini & Tavecchio, 2009), as shown in Fig. 2.4. The electromagnetic spectrum of relativistic jets is modeled by synchrotron radiation and inverse-Compton radiation derived by the interaction between relativistic electrons and different seed photons from synchrotron, molecular torus, BLR, accretion disk, and corona (Foschini et al., 2011). In addition, γ-ray NLS1s show soft X-ray spectra below 2 keV possibly originated from the X-ray corona, and display relatively hard X-ray spectra above 2 keV with a photon index of $\Gamma_X < 2$ indicating the relativistic jet dominance (Paliya et al., 2019). In the *Fermi* LAT regime, they have steep γ-ray spectra with a photon index of $\Gamma_\gamma > 2$ similar to FSRQs, and γ-ray luminosities smaller than powerful FSRQs (Romano et al., 2018; Paliya et al., 2018). These properties imply a strong similarity of γ-ray NLS1s with FSRQs. If the young age scenario is correct, γ-ray NLS1s might be the low luminosity and low black hole mass progenitors of the powerful FSRQs (Foschini et al., 2015; Berton et al., 2017).

As far as now, many studies tend to favor the scenario that NLS1s are a young and fast-growing phase of AGN, instead of an inclination effect. To explore the multi-wavelength properties of NLS1s, I adopt a standard ΛCDM cosmology with a Hubble constant $H_0 = 70$ km s^{-1} Mpc^{-1}, $\Omega_\Lambda = 0.73$ and $\Omega_M = 0.27$ in the following work (Komatsu et al., 2011).

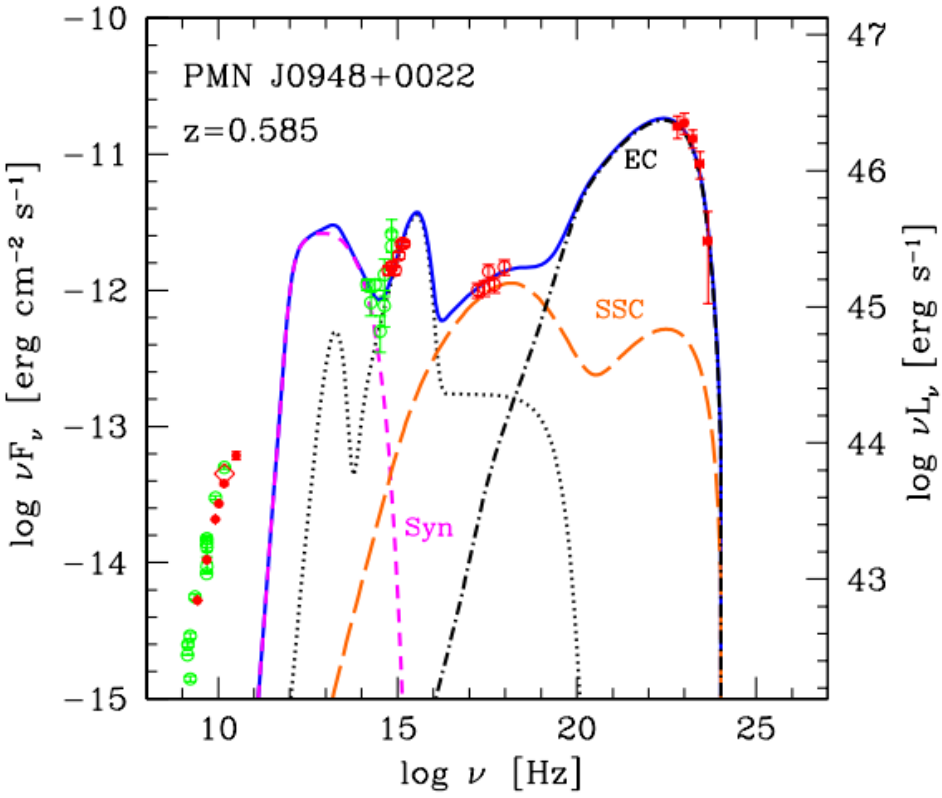

Figure 2.4: A broadband SED of PMN J0948+0022, which is the first γ-ray NLS1 discovered by the *Fermi* LAT. Figure is from Abdo et al. (2009a).

Chapter 3

Probing NLS1s in the southern hemisphere [1]

3.1 Sample selection

To have a better understanding of the nature of NLS1s, observations with advanced observing facilities will be necessary. NLS1s are typically fainter with respect to Blazars and Quasars, and RL NLS1s are especially tricky since they are usually located at relatively high redshift. Some new facilities, such as the Extremely Large Telescope (ELT), the Atacama Large Millimeter/sub-millimeter Array (ALMA), and the Square Kilometre Array (SKA), could make a great contribution in providing break-through evidences to solve many long lasting problems concerning this particularly intriguing class of AGN. However, most of these large telescopes are concentrated in the southern hemisphere. Therefore, the aim of this work is to create a new NLS1 sample that can be observed by large telescopes in the southern hemisphere, for the purpose of investigating the peculiarity of NLS1s with respect to other AGN.

To do this, I exploited the large unexplored archive of the Six-degree Field Galaxy Survey (6dFGS) [2]. The spectral data are collected from the 6dFGS, which is a combined redshift and peculiar velocity survey over the entire southern sky with $|b| > 10^{\circ}$. Optical spectra were obtained through separate V and R gratings and later spliced to produce combined spectra spanning 4000-7500 Å. The instrumental resolution is $R \sim 1000$ (Jones et al., 2004). The third and final data release (DR3) for the 6dFGS was published on 1 April 2009 (Jones et al., 2009).

I analyzed 110880 archive spectra from the 6dFGS DR3 catalog. They were first corrected for redshift using the cz velocity parameter (km s^{-1}) provided by the catalog. The continuum was fitted in two wavelength intervals (4725-4775 Å and 5075-5125 Å) that do

[1] This chapter is published on Chen et al. (2018b).

[2] http://www-wfau.roe.ac.uk/6dFGS/.

not show strong emission line, and subtracted from the original spectra. The root mean square (RMS) was calculated in the regions mentioned above as well. I selected objects showing strong Hβ and [O III] lines, based on the criterion that the peak of each emission line has to be larger than 3·RMS. In this case, I found 38563 objects that having both emission lines.

I then calculated the FWHM of these emission lines. The Hβ line was fitted with three Gaussians (one narrow component and two broad components), the [O III] line was fitted with two Gaussians (one narrow component and one broad component), and both of them were corrected for instrumental resolution (300 km s^{-1} for the 6dFGS). The narrow component is the line core and the broad components are usually associated with the gas outflow. An example of continuum subtraction and emission lines Gaussian fitting is shown in Fig. 3.1.

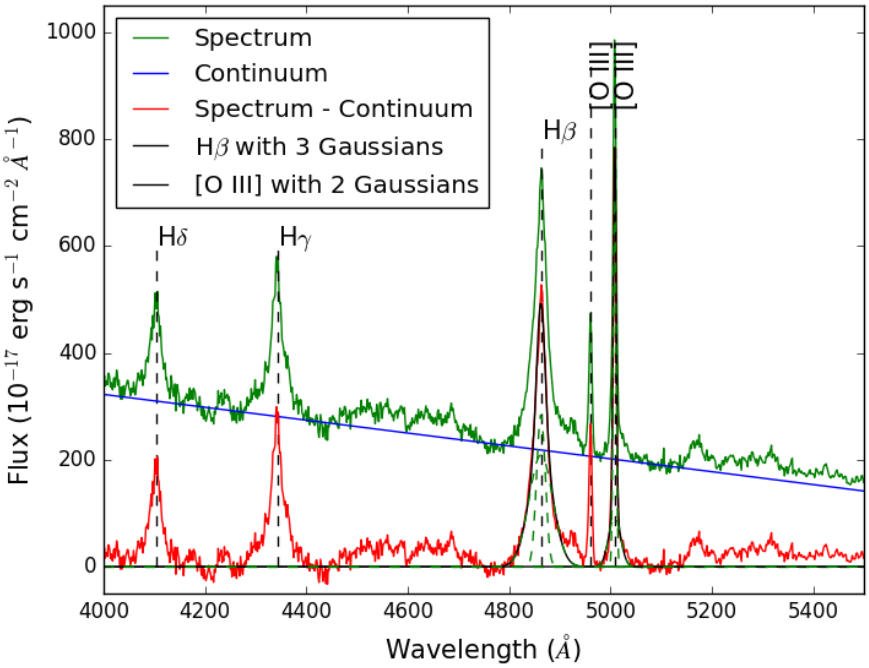

Figure 3.1: Spectrum of 6dFGS gJ135439.5-421457. The green line is the observed spectrum, the blue line is the continuum, the red line is the spectrum after the continuum subtraction, and the black line is the result of fitting Hβ with three Gaussians and [O III] with two Gaussians. Data are taken from the 6dFGS.

After reproducing the line profiles, I applied two additional conditions on the FWHM of lines. The first one was 600 km s^{-1} < FWHM(Hβ) < 2200 km s^{-1}. The lower limit is based on the mean FWHM of emission lines from the NLR measured by Vaona et al. (2012), and the upper limit was defined by the classic 2000 km s^{-1} criterion with a 10 % tolerance (Cracco et al., 2016). The second condition was 200 km s^{-1} < FWHM([O III])

< 2000 km s^{-1}. The lower limit avoids contamination by cosmic rays, while the upper limit avoids loss of objects with strong Fe II multiplets and relatively weak [O III] line (Osterbrock & Pogge, 1985; Mullaney et al., 2013). The FWHM distribution of Hβ and [O III] lines is plotted in Fig. 3.2. The fluxes of the Hβ and [O III] lines were measured by integrating the fitted profiles. I only focused on those objects with a flux ratio of [O III] / H$\beta < 3$, which is a main feature of NLS1s (Osterbrock & Pogge, 1985).

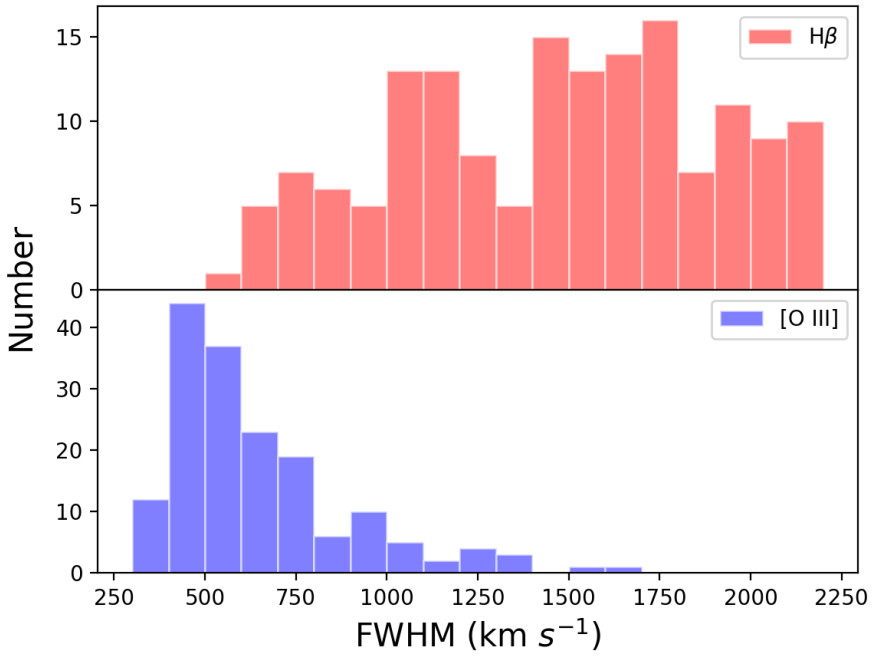

Figure 3.2: The FWHM distribution of Hβ and [O III] lines using a 100 bin width.

Based on the criteria mentioned above, I selected 2126 spectra and further analyzed them one by one to discern NLS1s from intermediate Seyfert galaxies and LINERs. Intermediate Seyfert galaxies and LINERs also have narrow emission lines and a flux ratio of [O III] / H$\beta < 3$ (Osterbrock, 1977; Veilleux & Osterbrock, 1987). However, there are two features in the spectra of NLS1s that distinguish them from the others. On one hand, Fe II multiplets are usually present in the spectra, because the BLR, where Fe II multiplets are originated, is directly visible in type I AGN. On the other hand, the Hβ line is broader than [O III] line and shows a Lorentzian profile caused by turbulence in the line emitting region (Kollatschny & Zetzl, 2013). The differences between NLS1s, intermediate Seyfert galaxies, and LINERs can be seen in Fig. 3.3. I included sources in my sample if one of these two features is present in the optical spectra.

In this way, I obtained a new sample of 167 NLS1s in the southern hemisphere. The object's name, coordinates, redshift, and luminosity distance are reported in Table 3.1; FWHM and flux of Hβ and [O III] lines are listed in Table 3.2. The range of redshift is

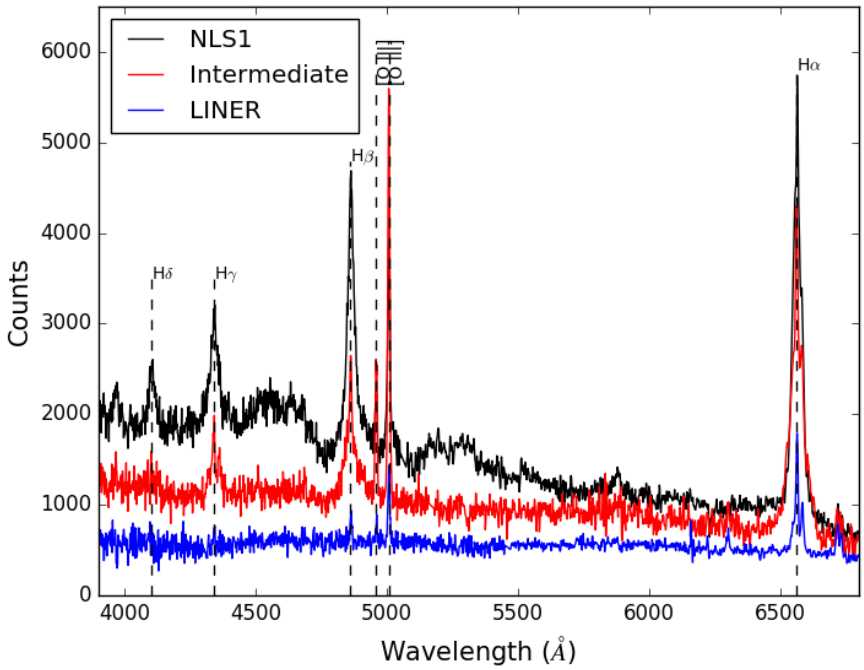

Figure 3.3: Three spectral examples showing the differences between a NLS1 6dFGS gJ123124.9-165350 (black line), an intermediate Seyfert galaxy 6dFGS gJ072957.1-654333 (red line), and a LINER 6dFGS gJ160558.2-263806 (blue line). Data are taken from the 6dFGS.

from $z = 0.01$ ($D_L = 44.49$ Mpc) to $z = 0.50$ ($D_L = 2825.63$ Mpc) with an average value of $z = 0.15$ ($D_L = 767.40$ Mpc). The redshift distribution of the sample is presented in Fig. 3.4.

3.2 Flux calibration

Spectra from the 6dFGS are not flux-calibrated, hence a method to calibrate the spectra in the sample is needed. I looked for NLS1s that are both in the 6dFGS sample and observed by the Sloan Digital Sky Survey (SDSS), based on a coordinates match between the 6dFGS and the SDSS spectroscopic database, within a tolerance radius of 0.1 arcmin. The images of the sources in both surveys were compared to make sure that the search resulted in the same sources that I was looking for. As a result, seven NLS1s observed by both the 6dFGS and the SDSS were selected for the flux calibration.

I also checked that these objects are not RL to reduce the effects of optical variability. This is because RL sources are found to have higher variability than RQ sources due to the presence of non-thermal emission coming from the relativistic jets along with thermal emission related to the accretion disk around the supermassive black hole in RL objects,

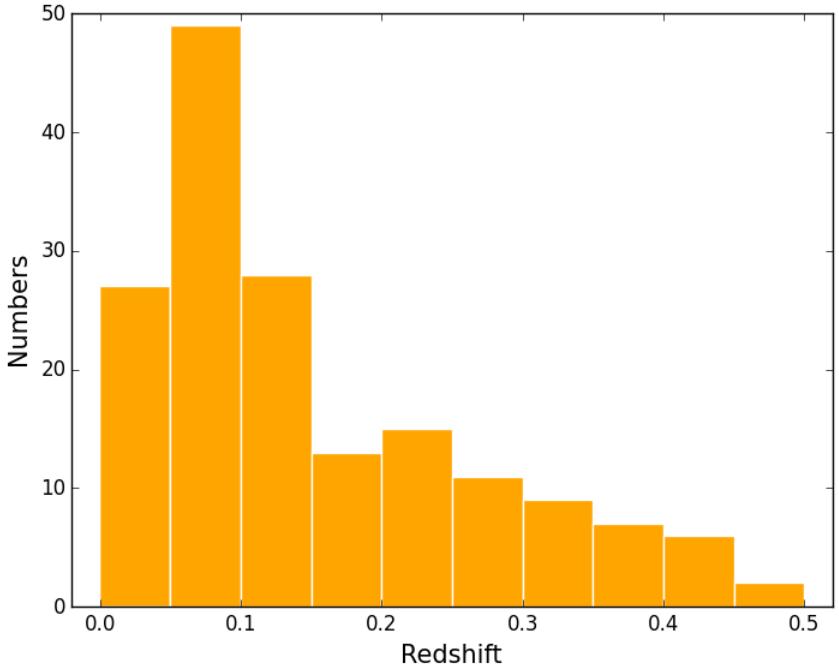

Figure 3.4: Redshift distribution of 167 NLS1s using a 0.05 bin width.

compared to the contribution of only thermal emission from the accretion disk in RQ objects (Rakshit & Stalin, 2017).

I calculated the ratio between counts and flux for each object, dividing the 6dFGS spectra by the SDSS spectra, then combined the results and averaged them using the IRAF V2.16 [3]. The sensitivity of the 6dFGS NLS1 sample was obtained by fitting the average ratio with a fifth order polynomial curve. The average $counts/flux$ ratio and the sensitivity are shown in Fig. 3.5. The airmass was considered in a crude correction for all data using the standard stars Feige 110 and EG274 in the 6dFGS observations (Jones et al., 2004). Hence, I calibrated the NLS1 spectra in the sample using the sensitivity obtained above. The spectra of these 167 NLS1s were then corrected for galactic extinction using the A_V extinction coefficients (Landolt V) (Schlafly & Finkbeiner, 2011) extracted from the NASA/IPAC [4] Extragalactic Database (NED) [5], and shifted to the rest frame. In this way I obtained flux-calibrated spectra for the NLS1 sample.

An issue with the method I used to calibrate the spectra is that the sensitivity was calculated on a limited number of objects, because of the small common sky coverage of the 6dFGS and the SDSS. In order to examine whether the flux calibration is acceptable, I compared the relation between the continuum flux and the optical magnitude of my 6dFGS

[3]http://iraf.noao.edu/

[4]The National Aeronautics and Space Administration / The Infrared Processing and Analysis Center.

[5]https://ned.ipac.caltech.edu/.

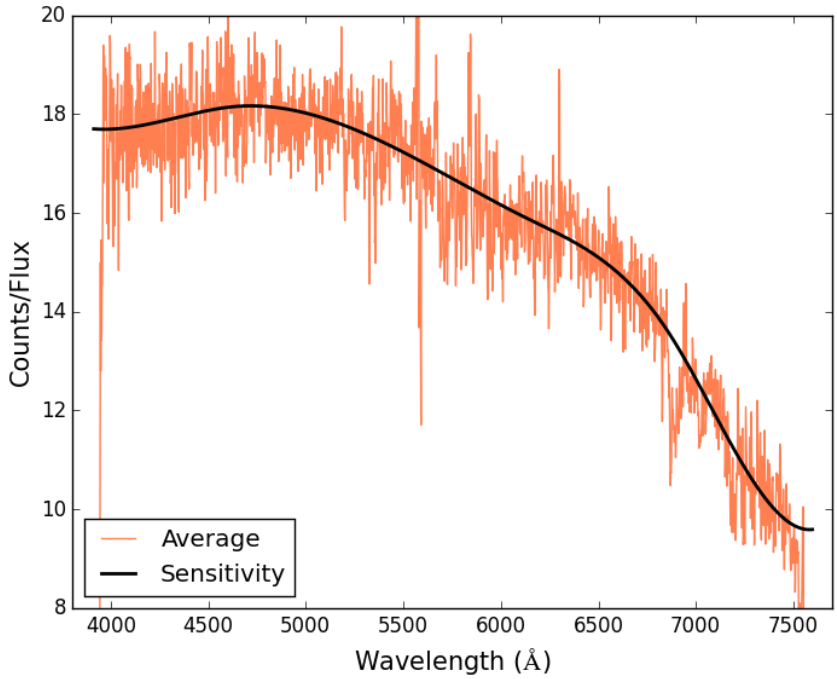

Figure 3.5: Average *counts*/*flux* ratio (red line) and sensitivity (black line) of the 6dFGS NLS1 sample.

re-calibrated spectra with that of NLS1s flux-calibrated spectra selected by Cracco et al. (2016), who investigated a sample of 296 NLS1s from the SDSS DR7.

I performed averaged flux measurements running on the wavelength range from 5050 Å to 5150 Å, to obtain the mean flux at 5100 Å for both the 6dFGS and SDSS samples. The magnitude on B-band of the 6dFGS sample is provided by the catalog. Instead the SDSS gives the magnitude of photometric measurements in the *ugriz* system. Hence I converted the magnitude on g and r bands for the objects in the SDSS sample into magnitude on B-band using the equation (Jester et al., 2005)

$$B = 1.28g - 0.28r + 0.09. \tag{3.1}$$

The magnitudes were also corrected for galactic extinction in both samples.

The relation between the mean flux at 5100 Å and the magnitude on B-band for the 6dFGS and SDSS samples is shown in Fig. 3.6. The best fit for the 6dFGS sample is

$$\log F(5100\text{Å}) = -(0.365 \pm 0.007)B + (8.117 \pm 0.147), \tag{3.2}$$

which is comparable with the one for the SDSS sample expressed by

$$\log F(5100\text{Å}) = -(0.376 \pm 0.003)B + (8.298 \pm 0.067). \tag{3.3}$$

Based on the consistent properties of my re-calibrated 6dFGS spectra with respect to the full flux-calibrated SDSS spectra, I inferred that the derived sensitivity provides a realistic

solution, though introducing a certain degree of uncertainty. The magnitude on B-band and the mean flux density at 5100 Å of the 6dFGS NLS1 sample are listed in Table 3.1.

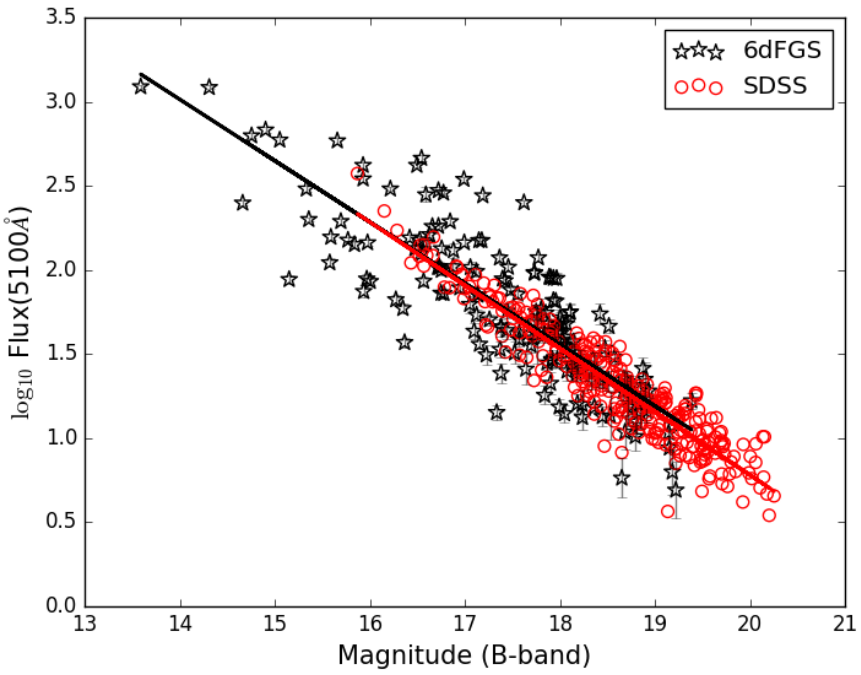

Figure 3.6: Relation of the mean flux at 5100 Å and the magnitude on B-band. The black stars and line are data from the 6dFGS sample, the red circles and line are data from the SDSS sample in Cracco et al. (2016).

I carried out an additional test for my flux calibration. Sources with a declination higher than $-15°$ and apparent magnitude brighter than 18 and 19 can be observed by the Asiago Astrophysical Observatory (Italy) 1.22 m and 1.82 m telescopes respectively. I observed 15 objects' optical spectra in the 6dFGS sample using these telescopes in October and November 2017 in the best seeing conditions of 1" (details are reported in Table 3.3). The observations were split into exposure times of 1200 s or 1800 s for each target to avoid strong contamination by cosmic rays and light pollution. The wavelength calibration was done by FeAr or NeHgAr lamps. Standard stars HR7596, HR9087, or HD2857, whose altitude close to the target, was used for the flux calibration. After the sky subtraction, I combined the spectra for each object, and corrected for galactic absorption and redshift.

I compared the flux-calibrated spectra obtained from the 6dFGS and the Asiago telescopes. Two examples are shown in Fig. 3.7. In spite of the fact that the sources used to create the sensitivity are not RL, I do expect some variations and the most critical effect on the thermal blue bump. On the other hand, differences on the red part can be well accounted for by the different aperture and seeing conditions. To estimate the uncertainty of my flux calibration, I computed the flux differences of [O III] line between the 6dFGS and

Table 3.3: Observational details of optical spectra from the Asiago Observatory.

Name	Observed date	Telescope	Exposure time
-	(yyyy-mm-dd)	-	(s)
6dFGS gJ000040.3-054101	2017-10-15	1.82 m	7200
6dFGS gJ002249.2-103956	2017-10-13	1.82 m	3600
6dFGS gJ013809.5-010920	2017-10-14	1.82 m	5400
6dFGS gJ015930.7-112859	2017-10-16	1.82 m	5400
6dFGS gJ020349.0-124717	2017-10-15	1.22 m	7200
6dFGS gJ021218.3-073720	2017-10-14	1.22 m	7200
6dFGS gJ021355.1-055121	2017-10-16	1.82 m	5400
6dFGS gJ034713.9-132547	2017-10-14	1.82 m	3600
6dFGS gJ042021.7-053054	2017-10-15	1.82 m	5400
6dFGS gJ043622.3-102234	2017-11-14	1.22 m	4800
6dFGS gJ044720.7-050814	2017-10-16	1.22 m	3600
6dFGS gJ045557.5-145641	2017-10-16	1.82 m	3600
6dFGS gJ193733.0-061305	2017-10-14	1.22 m	4800
6dFGS gJ211524.9-141706	2017-10-15	1.22 m	4800
6dFGS gJ213632.0-011626	2017-10-16	1.82 m	5400

Asiago spectra, finding an average uncertainty of 38.7%. Based on these properties, even though the uncertainties on the blue and red extremes of the spectral range are not negligible, the fluxes around Hβ line, [O III] lines, and 5100 Å continuum regions are consistent generally. Hence I supposed that for my purpose the flux calibration result is reliable and can be used to calculate black hole mass and Eddington ratio, though introducing a certain degree of uncertainty.

3.3 Luminosity correlation

Working with spectra produced by a multi-object spectrograph and fed by a system of fixed aperture entrance fibers, I have to account for the amount of light that enters the instrument. On one hand, I think about the nuclear active regions of external galaxies as unresolved point-like sources, the aperture of the 6dFGS instrument fibers is large enough to avoid the loss of significant amounts of light. On the other hand, the use of a fixed aperture implies that a varying amount of light from the AGN host galaxy, which can be an extended source with resolved structure, is also collected by the instrument. For strong type I AGN, which dominate over the host, this problem is not particularly relevant, but it can represent a significant issue in the case of nearby resolved Seyfert galaxies (Varisco et al., 2018). In general, this problem does not affect the spectral components that are purely originated by the AGN, such as the broad emission lines, while I have to take it

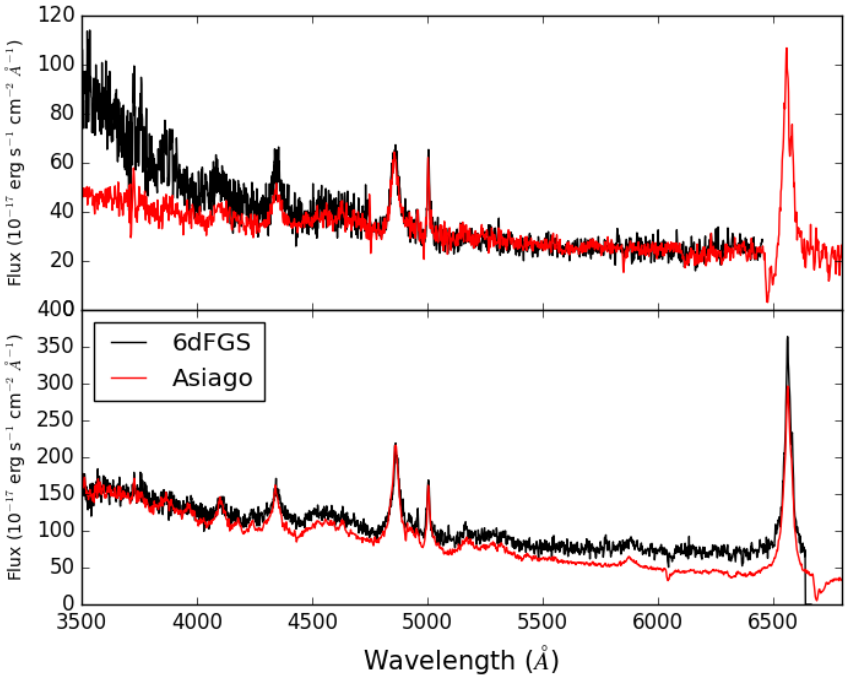

Figure 3.7: Top panel: Flux-calibrated spectra of 6dFGS gJ021218.3-073720 obtained from the 6dFGS (black line) and the Asiago 1.22 m Telescope (red line). Bottom panel: Flux-calibrated spectra of 6dFGS gJ045557.5-145641 obtained from the 6dFGS (black line) and the Asiago 1.82 m Telescope (red line).

into account when measuring the intensity of continuum, and to some extent the narrow emission lines.

In fact, estimating the host galaxy contribution in such spectra is not straightforward, because the relative amount of host galaxy stellar light with respect to the AGN signal, depends both on the AGN luminosity and on the fraction of the host surface that is subtended by the aperture that increases as a square of distance. To evaluate the contribution of stellar light from host galaxies in my sample, I applied a technique based on the principal component analysis (PCA), which was originally described in Connolly et al. (1995), and subsequently applied to a sample of type I AGN selected from the SDSS DR3 by La Mura et al. (2007). Following the strategy described in La Mura et al. (2007), I assumed that the observed spectra can be regarded as the linear combination of a set of spectral contributions, arising separately from the AGN and its host. If we call $S(\lambda)$ the amount of flux observed at a wavelength λ, this leads us to write

$$S(\lambda) = \sum_{i=1}^{n} a_i A_i(\lambda) + \sum_{j=1}^{m} h_j H_j(\lambda), \tag{3.4}$$

where $A_i(\lambda)$ and $H_j(\lambda)$ represent the spectral components produced by the AGN and its host respectively, a_i and h_j are their weight coefficients that do not depend on wavelength,

and n and m are the number of linear components used to model the AGN and its host. Using a proper set of base spectra, such as the list of eigenspectra provided by the low redshift collections in Yip et al. (2004a,b), Equation (3.4) expands to a system of algebraic equations that can be solved in terms of the weight coefficients. Thus I can estimate the contribution of AGN and host galaxy components in the spectra, after they have been corrected for galactic extinction and brought to their rest frame.

As the simple solution of Equation (3.4) may not always lead to a physically meaningful conclusion, because it introduces negative spectra or absorption features corresponding to forbidden lines, I developed an iterative fitting procedure written in Python. The algorithm looks for the solution of Equation (3.4), then it tests for the physical meaning of the separated AGN and host spectra. If either one of the components exhibits any inconsistency, its weight is reduced and the fit is run again leaving only the consistent parts free to vary. The algorithm then proceeds with an iteration fitting AGN and host alternatively, which are now forced to show only non-negative contributions, until the solution converges to a minimum chi-square χ^2 value or one of the components becomes undetected. After testing various configurations, I found that the best fit models leaving minimum residuals could be obtained from the combination of the first n AGN and the first m host galaxy components. Two examples of AGN and host galaxy decompositions are shown in Fig. 3.8.

The procedure is generally able to recover the host galaxy contribution, producing models with a median reduced residual of $\chi^2 = 1.45$ estimated over the sample. In a dozen cases, the host contribution turned out to be too faint to be distinguished. In all the other cases, I subtracted the host galaxy spectral models from my flux-calibrated spectra, in order to obtain an estimate of the light originally emitted by the AGN alone. After the host galaxy correction, the monochromatic luminosity at 5100 Å can be calculated by

$$L(\lambda) = 4\pi D_L^2 \cdot \lambda F(\lambda), \tag{3.5}$$

where D_L is the luminosity distance estimated by the cosmological redshift, $F(\lambda)$ is the averaged flux density on the wavelength range from 5050 Å to 5150 Å. I assume that the radiation from the sources is isotropic. The luminosity at 5100 Å may be overestimated in RL NLS1s due to the presence of relativistic jets can contaminate the continuum in RL sources. However, this impact is negligible, since only a small fraction of NLS1s are RL as mentioned above.

From the host galaxy subtractions, I noted that the stellar light has an important influence on the continuum. However, it only makes a minor contribution to the emission lines, since I did not see any strong emission or absorption line in the host galaxy components. Thus the luminosities of Hβ and [O III] lines can be estimated based on the flux-calibrated spectra. I first subtracted the continuum from the spectra, then fitted the Fe II multiplets and subtracted them from the continuum-subtracted spectra. The Fe II models were estimated using an online applet [6] described in Kovačević et al. (2010); Shapovalova et al. (2012). It reproduces 65 Fe II emission lines within the 4000-5500 Å range including five

[6] http://servo.aob.rs/FeII_AGN/.

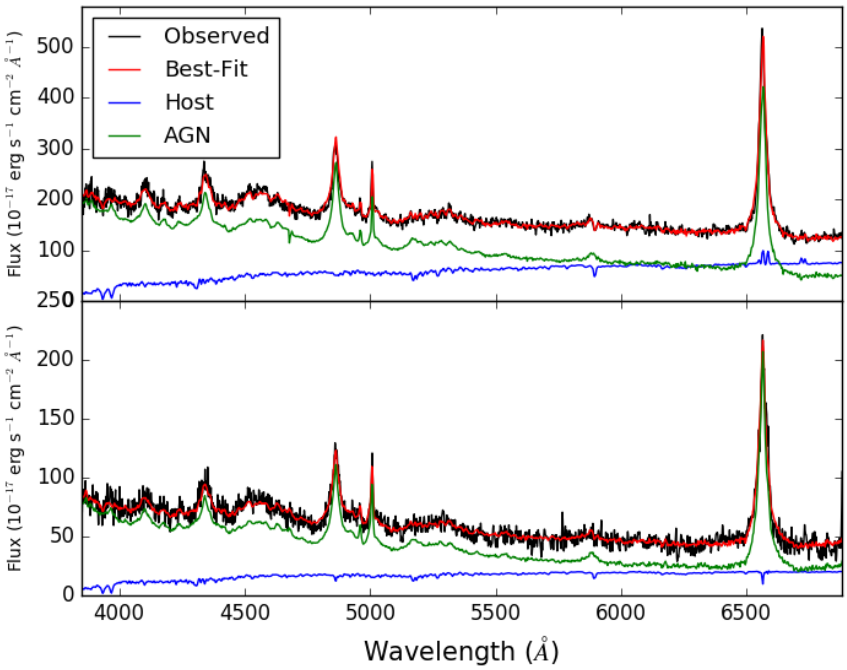

Figure 3.8: Decompositions of AGN and host galaxy in spectra 6dFGS gJ065017.5-380514 (top panel) and 6dFGS gJ084510.2-073205 (bottom panel). The black line shows the observed spectrum, the red line shows the best-fitted result, the green line shows the AGN component, and the blue line shows the stellar contribution.

line groups (F, S, G, P, I Zw 1), and fits each line with a single Gaussian. The free input parameters are temperature, Doppler width, shift, intensity of lines in each group, and iterations. The electron temperature of Fe II is shaping the line ratio within each group. While the intensity ratio between each of five groups depends on the concentration of Fe II. An example of Fe II multiplets fitting is shown in Fig. 3.9. During this procedure, I note that a certain degree of uncertainty could be introduced due to the Fe II lines blended with Hβ and [O III] lines, and the continuum subtraction combined with the noise in the spectra (Bon et al., 2018).

I used the spectra with both the continuum and the Fe II multiplets subtracted to estimate the fluxes and luminosities of Hβ and [O III] lines. The S/N ratio was computed from 5050 Å to 5150 Å wavelength range. If S/N $>$ 10, the Hβ line was fitted with three Gaussians (one narrow component and two broad components). Otherwise it was fitted with two Gaussians (one narrow component and one broad component), in order to avoid overfitting the noise in the case of low quality spectra. The [O III] line was fitted with two Gaussians. The luminosities of Hβ and [O III] lines is calculated by

$$L(line) = 4\pi D_L^2 \cdot F(line), \tag{3.6}$$

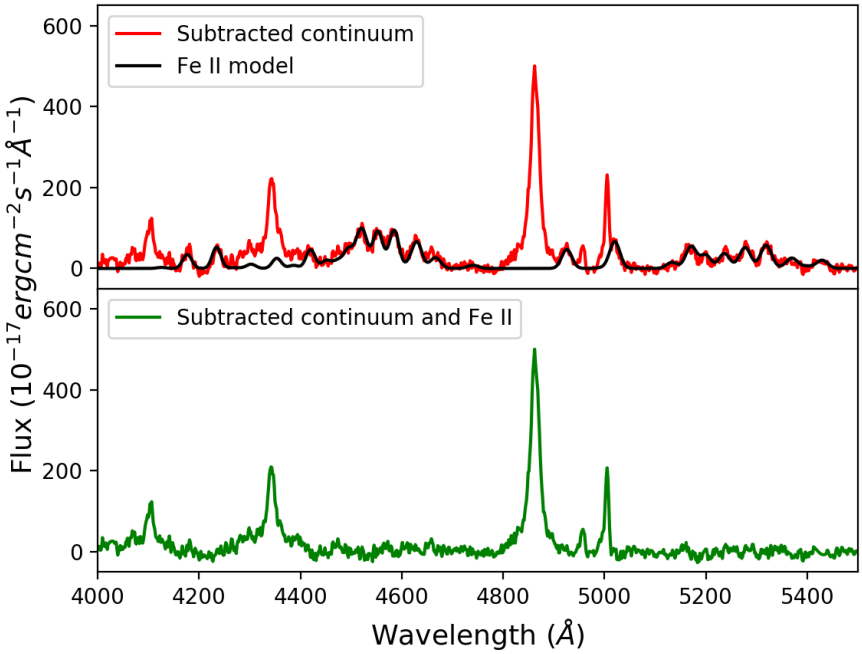

Figure 3.9: The Fe II multiplets fitting in spectrum 6dFGS gJ003915.9-511702. Top panel: The continuum-subtracted spectrum (red line) and the Fe II model (black line). Bottom panel: The spectrum after subtraction of both continuum and Fe II multiplets (green line). Data are taken from the 6dFGS.

where $F(line)$ is the flux derived by integrating the Hβ and [O III] line profiles.

The luminosity at 5100 Å, and the luminosities of Hβ and [O III] lines for the 6dFGS NLS1 sample are reported in Table 3.4. I plotted the monochromatic luminosity at 5100 Å against the luminosity of Hβ and [O III] lines and obtained strong correlations, as shown in Fig. 3.10. The linear regressions with a Bayesian method yield (Kelly, 2007)

$$\log L(H\beta) = (1.084 \pm 0.031) \log \lambda L_\lambda(5100\text{Å}) - (5.560 \pm 1.375), \tag{3.7}$$

and

$$\log L([OIII]) = (0.926 \pm 0.047) \log \lambda L_\lambda(5100\text{Å}) + (0.909 \pm 2.058). \tag{3.8}$$

I further plotted the FWHM against the luminosity of Hβ and [O III] lines and obtained weak correlations, as shown in Fig. 3.11. The linear regressions with a Bayesian method give (Kelly, 2007)

$$\log L(H\beta) = (1.396 \pm 0.347) \log FWHM(H\beta) + (37.567 \pm 1.096), \tag{3.9}$$

and

$$\log L([OIII]) = (1.600 \pm 0.324) \log FWHM([OIII]) + (37.027 \pm 0.903). \tag{3.10}$$

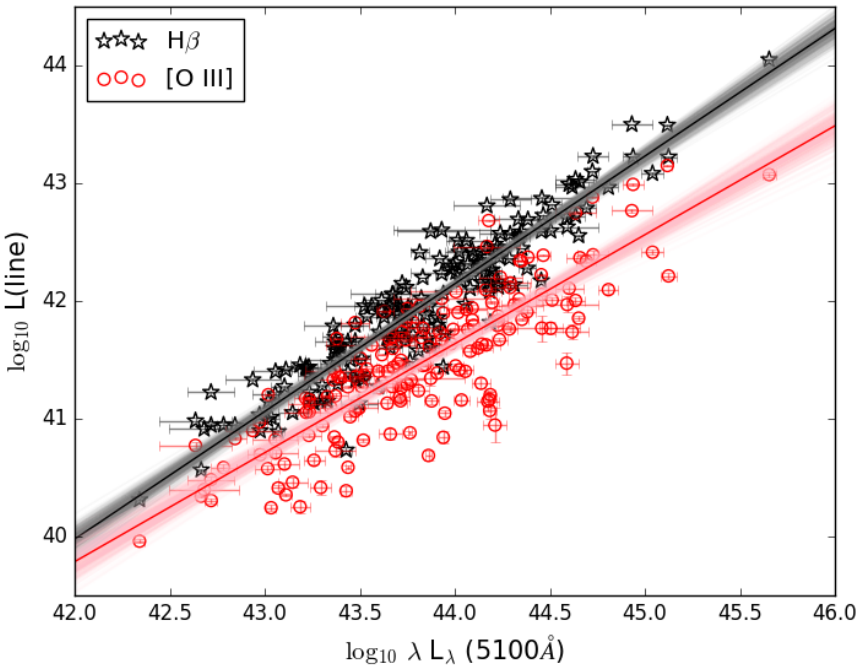

Figure 3.10: Relation of L (Hβ) - λL_λ (5100 Å) is shown in black stars and lines. Relation of L ([O III]) - λL_λ (5100 Å) is shown in red circles and lines.

A strong correlation between the luminosity of Balmer lines and the optical continuum was found by Greene & Ho (2005b); Greene et al. (2010), and supports the idea that the Balmer emission lines arise from recombination after photoionization by non-thermal continuum (Yee, 1980). Zhou et al. (2006) also found a correlation between the luminosity of [O III] line and the optical continuum, although not as tight as the L (Hβ) - λL_λ (5100 Å) correlation. This relation is useful for estimating the intrinsic luminosity of AGN, since the unobscured NLR, where the [O III] line comes from, can be reliably used to trace the central region properties (Zakamska et al., 2003). Additionally, the correlations between the luminosity and the FWHM of both emission lines are somehow expected even they are weak, as found by Véron-Cetty et al. (2001); Cracco et al. (2016). Since the luminosity of emission lines is proportional to the continuum luminosity, which in turn depends on the black hole mass. The black hole mass has an influence on the kinematics of the BLR and the NLR, thus affects the width of emission lines.

The errors of flux and luminosity of continuum were obtained by calculating their standard deviation σ in 5050-5150 Å wavelength range. The errors of FWHM, flux, and luminosity of emission lines were evaluated by the Monte Carlo method. This approach involves varying the line profiles with a random noise proportional to the RMS measured in the continuum range, then fitting the emission lines with Gaussians as previously mentioned, measuring FWHM, flux, and luminosity, and repeating the same process 100 times

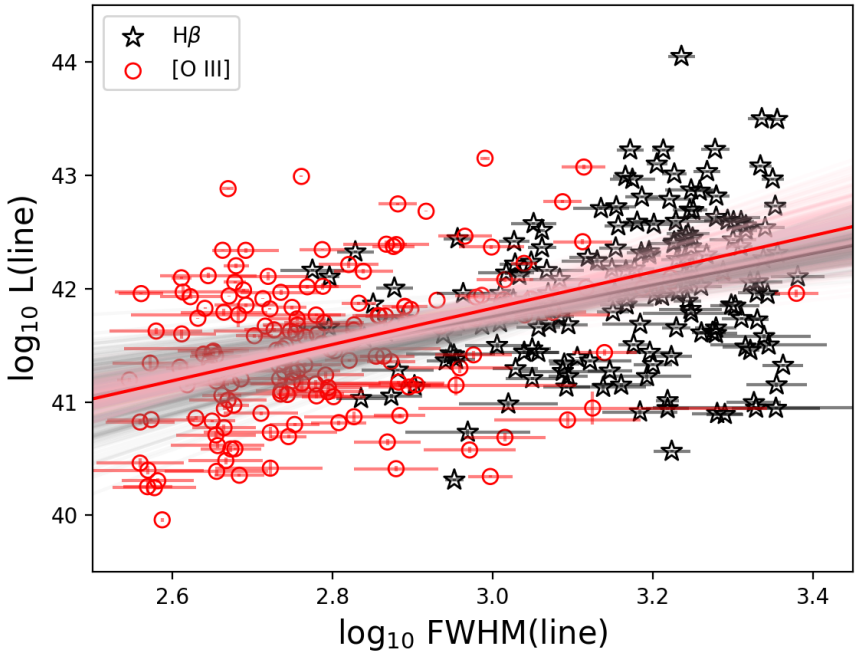

Figure 3.11: Relation of L(Hβ) - FWHM(Hβ) is shown in black stars and lines. Relation of L([O III]) - FWHM([O III]) is shown in red circles and lines.

to estimate their standard deviation. In this way, I obtained 1 σ errors for these parameters.

3.4 Black hole mass and Eddington ratio

I estimated the central black hole mass following the method in Foschini et al. (2015); Berton et al. (2015). For each NLS1 galaxy in the 6dFGS sample, the virial mass of central black hole is determined via Equation (1.1)

$$M_{BH} = f\left(\frac{R_{BLR}\sigma_{line}^2}{G}\right), \tag{3.11}$$

where I assumed $f = 4.31 \pm 1.05$ following Grier et al. (2013) who recalculated the mean virial factor for an entire sample of reverberation-mapped AGN. However, there could be a bias in the virial factor determination due to this value relied on the sample selection and the inclination and geometry of the BLR. The size of the BLR was calculated using the relation between the luminosity at 5100 Å $L_{5100\text{Å}}$ and the radius of the BLR R_{BLR} from Bentz et al. (2013) who updated the $R_{BLR} - L_{5100\text{Å}}$ relationship covering a wide range

luminosity,

$$\log\left(\frac{R_{BLR}}{1\,\text{light day}}\right) = 1.527^{+0.031}_{-0.031} + 0.533^{+0.035}_{-0.033}\log\left(\frac{\lambda L_\lambda(5100\text{Å})}{10^{44}\,\text{erg s}^{-1}}\right). \quad (3.12)$$

The line dispersion second-order moment σ_{line}, which is less affected by inclination and line profile than a FWHM measurement (Peterson et al., 2004; Collin et al., 2006), was measured from the Hβ broad components. If the Hβ line has two broad components, the $\sigma_{H\beta}$ is evaluated by

$$\sigma^2_{H\beta} = \frac{\int \lambda^2 P(\lambda) d\lambda}{\int P(\lambda) d\lambda} - \left(\frac{\int \lambda P(\lambda) d\lambda}{\int P(\lambda) d\lambda}\right)^2, \quad (3.13)$$

where $P(\lambda)$ is the Hβ line profile produced by two broad components. If it has only one broad component, then $\sigma_{H\beta} \simeq \text{FWHM}_{H\beta_{broad}}$ / 2.355.

The Eddington luminosity can be measured after obtaining the central black hole mass via Equation (1.4)

$$L_{Edd} = 1.3 \times 10^{38}\left(\frac{M_{BH}}{M_\odot}\right)\,\text{erg s}^{-1}. \quad (3.14)$$

The Eddington ratio $\epsilon_{Edd} = L_{bol}/L_{Edd}$ is calculated following Equation (1.5), where the bolometric luminosity is estimated assuming $L_{bol} = 9\lambda L_\lambda(5100\text{Å})$ (Kaspi et al., 2000).

The distributions of central black hole mass and Eddington ratio for 167 NLS1s in the 6dFGS sample are plotted in Fig. 3.12, and their estimated values are presented in Table 3.4. The masses of central black hole M_{BH} range from $8.1 \times 10^5 M_\odot$ to $7.8 \times 10^7 M_\odot$ with a median value of $8.6 \times 10^6 M_\odot$. The Eddington ratios ϵ_{Edd} span from 0.07 to 5.35 with a median value of 0.96. This result confirms that NLS1s have lower black hole mass and higher Eddington ratio than BLS1s. The errors of central black hole mass and Eddington ratio were evaluated by the Python uncertainties package following the error propagation theory. I obtained mean errors of 26.7% and 31.3% for the black hole mass and Eddington ratio measurements respectively.

3.5 Radio sources

With the aim of looking for radio sources in the 6dFGS sample, I subsequently cross-matched these 167 NLS1s with several important radio surveys covering the southern hemisphere, including the NRAO VLA [7] Sky Survey (NVSS), the Sydney University Molonglo Sky Survey (SUMSS), and the Australia Telescope 20 GHz Survey (AT20G), within a search radius of 5 arcsec. The NVSS covers the entire sky north of $-40°$ declination at 1.4 GHz with the flux density limit of 2.5 mJy (Condon et al., 1998), the SUMSS covers the sky south of $-30°$ declination at 843 MHz with the flux density limit of 8 mJy (Mauch et al., 2003), and the AT20G covers the whole sky south of 0° declination at 5 GHz, 8.4 GHz, and 22 GHz respectively, with the flux density limit of 40 mJy (Murphy et al., 2010).

[7] The National Radio Astronomy Observatory Very Large Array.

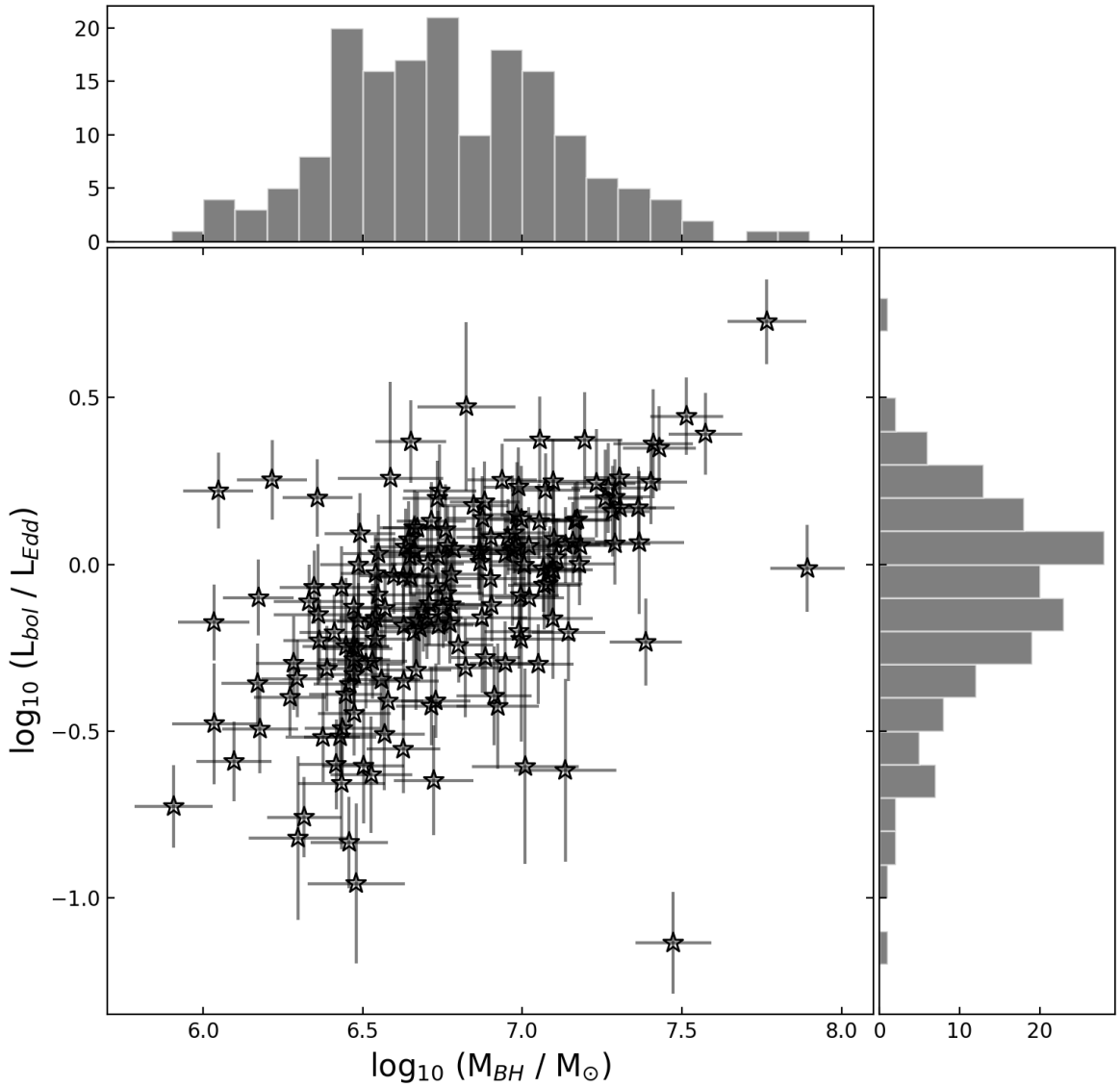

Figure 3.12: Distributions of central black hole mass and Eddington ratio in the 6dFGS NLS1 sample.

I found 18 sources only detected by the NVSS, three sources only detected by the SUMSS, one source detected by both the NVSS and the SUMSS, and one source detected by both the SUMSS and the AT20G. In total 23 (13.8%) sources have associated radio counterparts. The flux densities detected by the radio surveys for these 23 sources are listed in Table 3.5 respectively.

The radio loudness $R_L = F_{5GHz}/F_{B-band}$ was calculated using the radio flux at 5 GHz and the optical flux at B-band 4400 Å for each object. In most cases the radio flux was

Table 3.6: Mean values of redshift, black hole mass, radio luminosity at 5 GHz, and optical luminosity on B-band of the RL and RQ subsample

Subsample	Number	Redshift	$\log_{10}(M_{BH}/M_{\odot})$	$\log_{10} L_{radio}$	$\log_{10} L_{optical}$
All	23	0.14	6.71	39.55	43.94
RL	12	0.20	6.82	40.15	44.07
RQ	11	0.06	6.59	38.90	43.79

obtained at 1.4 GHz and 843 MHz instead of 5 GHz. I derived the radio flux at 5 GHz under the hypothesis that the radio spectrum can be described with a power-law model $F_\nu \propto \nu^{-\alpha}$, and I assumed a conservative spectral index of $\alpha = 0.5$ (Yuan et al., 2008). In this way I found 12 (7.0% of the whole sample) RL (including one very RL) NLS1s and 11 RQ NLS1s. If I suppose that the radio spectrum has a flat spectral index of $\alpha = 0$, 17 objects were found to be RL and six objects were found to be RQ. Instead assuming a steep radio spectral index of $\alpha = 1$, I found that seven objects are RL and 16 objects are RQ. In this paper, I classified my sources according to the results of $\alpha = 0.5$.

Williams et al. (2002) analyzed 150 NLS1s in the SDSS Early DR and found that only a dozen (8%) were detected at radio frequencies and only two (1.3%) were RL. Research by Zhou et al. (2006) based on the SDSS DR3 resulted in a sample of 2011 NLS1s and of those 142 (7.1%) objects had radio counterparts. Cracco et al. (2016) investigated a sample of 296 NLS1s from the SDSS DR7, 70 (23.6%) sources were detected at radio frequencies and 11 (3.7% of the total sample and 15.7% of those radio detected) of them were classified as RL. A recent study by Rakshit et al. (2017) proposed a new catalog from the SDSS DR12 that contains 11101 NLS1s, among them 555 (5%) objects were detected on radio band and 378 (3.4%) were RL.

The radio fraction is different in all these samples because the radio-loudness strongly depends on the spatial resolution of the radio and optical observations. The flux is different if the observations considered the whole galaxy (including the contribution of both AGN and host) or only the nuclear region. Then the evaluated R_L is different for the same galaxy. This situation happens both on radio and optical observations. Ho & Peng (2001) found that most Seyfert 1 nuclei were classified as RL AGN if only their nuclear luminosity was considered, which was in doubt later.

The flux densities and luminosities on radio and optical bands, radio-loudness, and radio type of the radio sample are reported in Table 3.5. The mean values of redshift, black hole mass, radio luminosity at 5 GHz, and optical luminosity on B-band of the RL and RQ subsamples are presented in Table 3.6. Their number and cumulative distributions are shown in Fig. 3.13. However, I note that the radio luminosity could be biased, because a single spectral index was used in the flux conversion, and the same observed frequency may correspond to different frequencies in the rest frame and different intrinsic components in the radio SED.

I used the two-sample Kolmogorov-Smirnov (K-S) test to examine whether the parent population of the RL and RQ subsample is the same. The null hypothesis is that two

Figure 3.13: The number (top panel) and cumulative (bottom panel) distributions of the RL (red) and RQ (blue) sources in our radio detected NLS1 sample

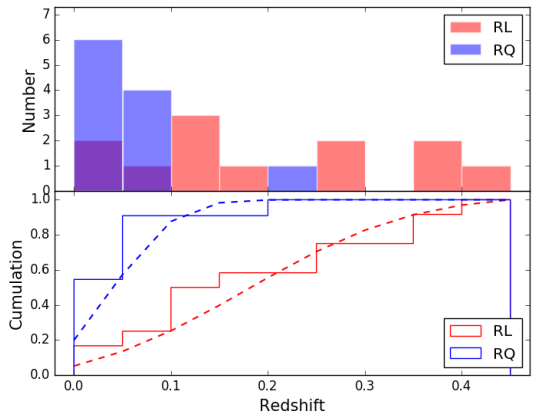

(a) Redshift distribution using a 0.05 bin width.

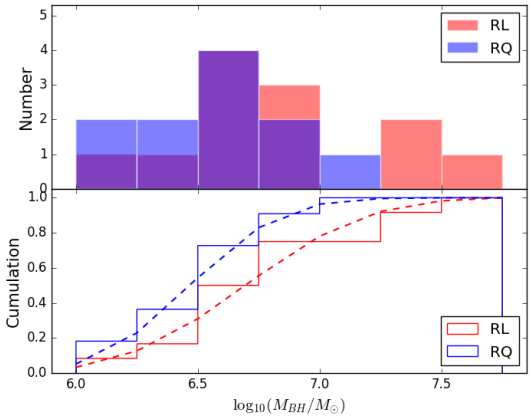

(b) Black hole mass distribution using a 0.25 bin width.

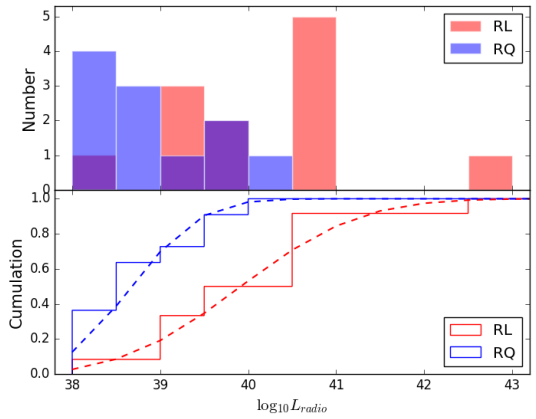

(c) Radio luminosity at 5 GHz distribution using a 0.5 bin width.

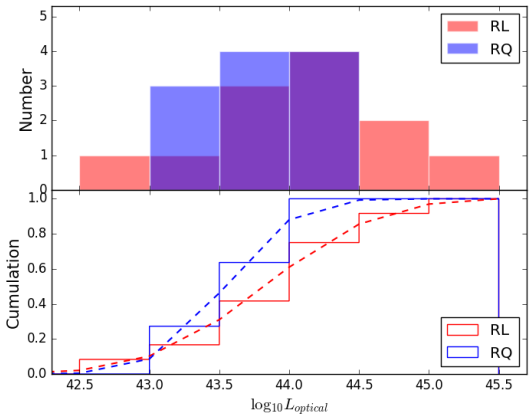

(d) Optical luminosity on B-band distribution using a 0.5 bin width.

distributions originated from the same population of sources. I applied the rejection of the null hypothesis at a 95% confidence level corresponding to a value of $p \leq 0.05$. The K-S tests of redshift ($p = 1.8 \times 10^{-3}$) and radio luminosity ($p = 2.0 \times 10^{-4}$) suggest that the RL and RQ NLS1s in the sample have different populations. However, the K-S tests of black hole mass ($p = 0.47$) and optical luminosity ($p = 0.055$) argue that these RL and RQ sources have the same origin.

This result is expected. The different redshift distribution may be caused by a selection effect. RL sources with high luminosity can be detected both at low and high redshift. Whereas, RQ sources are faint and can be observed only at low redshift due to the flux

density limit of radio surveys. The different radio luminosity distribution may be related to the presence of radio jets. RL NLS1s generally harbor relativistic jets, instead jets in RQ NLS1s are usually weak or absent. However, the optical luminosity and black hole mass distributions have the same origin, the possible reason is that the optical luminosity is emitted from the accretion disk and the black hole mass is derived from the optical continuum in this analysis. This result also implies that the presence of relativistic jets is not related to the central black hole mass.

The cumulative distributions of the radio sample show as well that RL sources tend to have higher redshift, a more massive black hole, and higher radio and optical luminosities than RQ sources on average. This may be related to the jet activity. RL NLS1s usually harbor relativistic jets emitting low-energy synchrotron radiation in radio frequency and high-energy inverse Compton radiation up to γ-ray energy. Instead jets are probably weak or absent in RQ NLS1s. The mass accretion rate of sources with jets is higher than that of sources without jets. Since the presence of jets enhances angular momentum transport, matter in the accretion disk loses angular momentum and falls into the central black hole faster. This can greatly increases the black hole mass growth rate, therefore RL sources have larger black hole masses and higher luminosities compared to RQ sources (Jolley & Kuncic, 2008). Finally, I remark that these results should be taken with cautions because of the small radio sample used in these analyses.

3.6 X-ray properties of radio sample [8]

With the aim of further investigating the X-ray properties of radio-emitting NLS1s in the 6dFGS sample, I carried out an observational campaign with the *Swift* X-Ray Telescope (XRT) (Burrows et al., 2005) from November 2017 to March 2018. These objects are strong candidates of harboring relativistic jet activity. The analysis of X-ray data might contribute to clarify the role of central black hole, because it directly probes the nature and intensity of the ionizing radiation continuum.

Data analysis was performed following standard procedures (XRTPIPELINE). I considered the data observed in photon counting (PC) mode. The channels with discarded data [9] and energies out of the broad-band range provided by the *Swift* XRT detector (below 0.3 keV and above 10.0 keV) were excluded from the fit. The XRT spectral counts were rebinned to have 20 counts per bin in order to apply the Chi-squared χ^2 statistics. When the number of counts was not enough to do this, I applied the unbinned likelihood and forced to use the Cash statistics (Cash, 1979). Each spectrum was fitted with an ISM grain absorption (tbabs) plus a redshifted power-law (zpowerlaw) model using the XSPEC

[8] This chapter is published on Chen et al. (2018a).

[9] Some are below the lower discriminator of the instrument and therefore do not contain valid data. Some have imperfect background subtraction at the margins of the pass band. Some may not contain enough counts for χ^2 to be strictly meaningful.

version 12.10.0 (Arnaud, 1996) [10]. The *Swift* XRT observational details and spectral fitting results are reported in Table 3.7. An example of the spectral modeling is shown in Fig. 3.14.

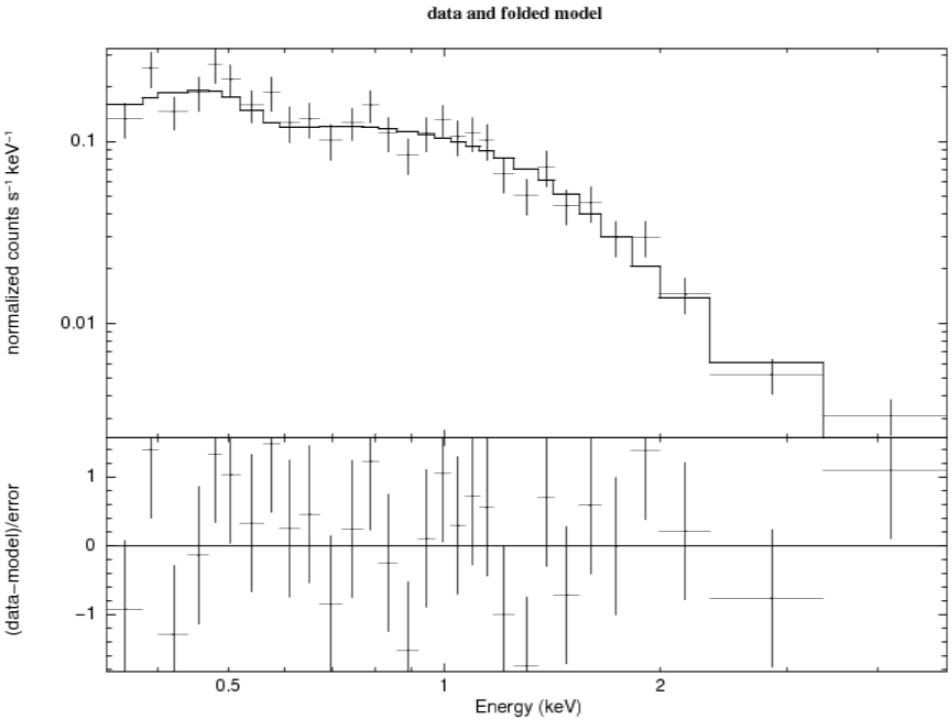

Figure 3.14: The *Swift* XRT spectrum of 6dFGS gJ084628.7-121409 fitted with a galactic absorption and a redshifted power-law model.

The average X-ray spectral index of these objects in the 0.3-10.0 keV energy band is $\alpha = 0.88 \pm 0.4$ (power-law model $\Gamma = \alpha + 1$). Compared to the mean values of FSRQs ($\alpha = 0.58$), BL Lacs ($\alpha = 1.3$), and BLS1s ($\alpha = 1.1$), the average X-ray spectral index of NLS1s is softer than FSRQs while harder than BL Lacs and BLS1s (Foschini et al., 2015). This could be because the X-ray emission in FSRQs is dominated by the inverse Compton radiation from a relativistic jet, while in NLS1s is mainly from the corona above the accretion disk (Ghisellini et al., 2010). However, I remark that these results should be taken with caution due to the small number of X-ray sources and the limited photon counts from the *Swift* observations.

3.7 Summary

In this work, I exploited the optical spectra from the 6dFGS DR3, which is currently the most extensive spectroscopic survey available in the southern hemisphere, to perform

[10] https://heasarc.nasa.gov/xanadu/xspec/manual/node1.html.

the first systematic selection of NLS1s in this sky region. The NLS1 sample was selected from this survey and flux calibration for the optical spectra in the sample was derived. The luminosity correlations of L (Hβ) - λL_λ (5100 Å) and L ([O III]) - λL_λ (5100 Å) were found. The central black hole mass and the Eddington ratio were estimated for each target. In addition, the radio counterparts were found for some sources by the radio surveys covering the southern hemisphere. The main results of this work are summarized as follows.

1. According to the criteria of 600 km s^{-1} < FWHM(Hβ) < 2200 km s^{-1} and a flux ratio of [O III] / Hβ < 3, as well as considering the visibility of Fe II multiplets and Hβ line profiles in the optical spectra, I created a new accurate sample of 167 NLS1s from the 6dFGS in the southern hemisphere.

2. The flux-calibrated spectra for these 167 NLS1s in the sample which were not provided by the 6dFGS were obtained. To evaluate the reliability of the flux calibration, the relation between the mean flux at 5100 Å and the magnitude on B-band was calculated for the 6dFGS sample, and the result is in good agreement with the SDSS NLS1 sample from Cracco et al. (2016). I further compared 15 flux-calibrated spectra in the 6dFGS sample with the new observations specifically carried out at the Asiago Observatory, and confirmed that my flux calibration of the 6dFGS spectra on Hβ line, [O III] lines, and 5100 Å continuum regions is consistent.

3. The monochromatic luminosity at 5100 Å, and the luminosities of Hβ and [O III] lines were estimated. Strong correlations of L (Hβ) - λL_λ (5100 Å) and L ([O III]) - λL_λ (5100 Å) could be confirmed.

4. The mass of central black hole and the Eddington ratio were calculated for each target, and found to lie in the ranges of $M_{BH} \sim 10^{5.91-7.89} M_\odot$ and $\epsilon_{Edd} \sim$ 0.07-5.35 respectively, with average values of $M_{BH} = 10^{6.93} M_\odot$ and $\epsilon_{Edd} = 0.96$, which are typical values for NLS1s. This result confirms that NLS1s have lower black hole mass and higher Eddington ratio than BLS1s.

5. Of the 167 NLS1s in the 6dFGS sample, 23 (13.8%) sources were found to have associated radio counterparts, including 12 (7.0%) RL NLS1s and 11 RQ NLS1s. RL sources tend to have higher redshift, a more massive black hole, and higher radio and optical luminosities than RQ sources.

6. In addition, I carried out an observational campaign of radio-emitting NLS1s in the 6dFGS sample with the *Swift* XRT. The X-ray spectra were fitted with a galactic absorption and a redshifted power-law models in the 0.3-10.0 keV energy range. The average spectral index of NLS1s is softer than FSRQs while harder than BL Lacs and BLS1s.

My conclusions increase the number of NLS1s and confirm some well known properties of this peculiar class of AGN. However, the number of NLS1s in the 6dFGS sample is still limited, in particular radio and X-ray sources. Further research with larger samples as well as higher resolution and sensitivity observations will be necessary, to understand the physical mechanism and evolution of NLS1s with respect to other types of AGN. I expect that the investigation of these sources with high performance observation facilities located in the southern sites, will help to clarify many of the fundamental questions that have not yet been solved on this class of galaxies. In the following work, I will investigate the multi-wavelength characterization of the NLS1 sample going from γ-ray, to X-ray, to radio

bands.

Table 3.1: Coordinates, redshift, luminosity distance, magnitude on B-band, and mean flux density at 5100 Å in the 6dFGS NLS1 sample.

Name	RA	Dec	Redshift	D_L	B	F (5100Å)
-	(hh:mm:ss)	(dd:mm:ss)	-	(Mpc)	(mag)	(10^{-17} erg s^{-1} cm^{-2} Å^{-1})
6dFGS gJ000040.3-054101	00:00:40.26	-05:41:0.9	0.0939	430.38	17.765	41.35 ± 16.79
6dFGS gJ001302.3-323830	00:13:2.25	-32:38:29.9	0.2593	1313.9	18.577	30.25 ± 2.75
6dFGS gJ001521.6-150951	00:15:21.63	-15:09:51.0	0.0788	357.38	18.717	15.33 ± 3.98
6dFGS gJ001641.9-312657	00:16:41.86	-31:26:56.9	0.3604	1921.63	18.063	33.69 ± 3.69
6dFGS gJ002121.6-205018	00:21:21.55	-20:50:17.6	0.183	887.91	17.697	35.59 ± 3.2
6dFGS gJ002249.2-103956	00:22:49.16	-10:39:55.8	0.4142	2263.79	18.425	23.21 ± 3.42
6dFGS gJ003000.5-202856	00:30:0.52	-20:28:56.2	0.2889	1486.83	18.652	5.8 ± 1.57
6dFGS gJ003211.0-324205	00:32:10.95	-32:42:5.1	0.3539	1881.14	18.667	18.87 ± 2.22
6dFGS gJ003740.0-542030	00:37:40.00	-54:20:29.9	0.1008	464.43	18.077	25.09 ± 3.4
6dFGS gJ003915.9-511702	00:39:15.85	-51:17:1.5	0.0286	125.22	16.776	286.77 ± 7.73
6dFGS gJ004039.2-371317	00:40:39.17	-37:13:16.8	0.036	158.25	15.969	88.41 ± 6.43
6dFGS gJ004324.9-165557	00:43:24.91	-16:55:57.1	0.3301	1734.66	17.851	55.46 ± 5.44
6dFGS gJ010313.2-480445	01:03:13.19	-48:04:45.1	0.4245	2330.15	18.895	22.4 ± 5.3
6dFGS gJ011442.5-513614	01:14:42.46	-51:36:13.8	0.2049	1007.2	19.146	10.76 ± 1.52
6dFGS gJ011730.6-382630	01:17:30.64	-38:26:29.9	0.2255	1121.13	18.214	30.35 ± 3.09
6dFGS gJ011935.7-282132	01:19:35.69	-28:21:31.5	0.3489	1849.87	18.068	47.88 ± 3.8
6dFGS gJ012237.5-264646	01:22:37.52	-26:46:45.9	0.4174	2284.63	19.184	6.3 ± 1.97
6dFGS gJ013117.1-395631	01:31:17.09	-39:56:30.7	0.4989	2825.63	18.515	21.99 ± 3.06
6dFGS gJ013137.9-294229	01:31:37.88	-29:42:29.2	0.2711	1382.43	19.154	8.76 ± 2.36
6dFGS gJ013335.0-210959	01:33:35.03	-21:09:59.0	0.1296	608.38	17.825	43.72 ± 2.56
6dFGS gJ013546.4-353915	01:35:46.35	-35:39:15.3	0.1373	647.83	17.888	90.71 ± 6.76
6dFGS gJ013809.5-010920	01:38:9.54	-01:09:20.1	0.2731	1393.86	17.88	47.83 ± 3.09
6dFGS gJ014222.3-352541	01:42:22.28	-35:25:41.4	0.094	430.8	17.733	96.6 ± 5.45
6dFGS gJ015251.6-523824	01:52:51.57	-52:38:24.3	0.0766	347.09	17.557	71.85 ± 4.33
6dFGS gJ015930.7-112859	01:59:30.69	-11:28:58.5	0.1609	770.02	18.423	54.78 ± 7.83
6dFGS gJ020039.1-084555	02:00:39.12	-08:45:55.0	0.4324	2381.84	18.531	13.58 ± 4.41
6dFGS gJ020349.0-124717	02:03:49.03	-12:47:16.6	0.0525	233.91	16.536	124.55 ± 7.58
6dFGS gJ021201.5-020154	02:12:1.47	-02:01:53.8	0.4376	2416.19	19.221	4.91 ± 1.87
6dFGS gJ021218.3-073720	02:12:18.34	-07:37:19.8	0.1739	839.16	17.865	28.02 ± 2.66
6dFGS gJ021355.1-055121	02:13:55.14	-05:51:21.2	0.1399	660.85	17.524	32.15 ± 4.88
6dFGS gJ021738.1-300448	02:17:38.10	-30:04:47.7	0.0803	364.65	17.227	31.31 ± 4.14
6dFGS gJ022219.4-533239	02:22:19.44	-53:32:39.1	0.0955	438.06	17.983	47.59 ± 9.3
6dFGS gJ022815.2-405715	02:28:15.23	-40:57:14.7	0.4934	2787.94	17.623	251.38 ± 9.49
6dFGS gJ023005.5-085953	02:30:5.53	-08:59:53.3	0.0161	69.86	14.904	679.75 ± 26.94
6dFGS gJ023927.6-534508	02:39:27.62	-53:45:7.9	0.3124	1627.12	18.795	10.24 ± 2.0
6dFGS gJ023956.2-111813	02:39:56.17	-11:18:12.6	0.2035	999.17	17.994	15.35 ± 1.64
6dFGS gJ025228.4-592243	02:52:28.38	-59:22:43.0	0.209	1029.6	18.185	16.07 ± 1.93
6dFGS gJ030735.3-725003	03:07:35.32	-72:50:2.5	0.0276	120.79	15.359	199.69 ± 5.28
6dFGS gJ031558.9-290126	03:15:58.92	-29:01:26.4	0.3067	1592.73	18.517	46.29 ± 4.21
6dFGS gJ034713.9-132547	03:47:13.90	-13:25:46.9	0.1918	935.29	18.308	25.3 ± 3.62
6dFGS gJ035056.7-102559	03:50:56.74	-10:25:58.8	0.1284	602.09	18.147	37.47 ± 4.4
6dFGS gJ035107.6-052637	03:51:7.60	-05:26:37.0	0.0678	305.19	16.751	72.79 ± 3.85
6dFGS gJ035432.8-134008	03:54:32.84	-13:40:7.8	0.0764	346.13	17.149	149.76 ± 8.39
6dFGS gJ040024.4-250044	04:00:24.40	-25:00:44.3	0.0974	447.78	17.139	70.89 ± 3.11
6dFGS gJ041307.1-005017	04:13:7.09	-00:50:16.6	0.0402	177.35	15.977	145.27 ± 5.65

Table 3.1: continued.

Name	RA	Dec	Redshift	D_L	B	Flux(5100Å)
-	(hh:mm:ss)	(dd:mm:ss)	-	(Mpc)	(mag)	(10^{-17} erg s^{-1} cm^{-2} Å^{-1})
6dFGS gJ042020.4-355100	04:20:20.40	-35:51:0.3	0.1961	958.7	18.474	34.29 ± 3.53
6dFGS gJ042021.7-053054	04:20:21.74	-05:30:54.4	0.1991	974.91	18.002	41.92 ± 4.23
6dFGS gJ042256.6-185442	04:22:56.56	-18:54:42.3	0.0641	287.89	16.877	104.6 ± 5.46
6dFGS gJ043526.5-164346	04:35:26.50	-16:43:46.0	0.0983	451.75	18.11	56.31 ± 5.26
6dFGS gJ043622.3-102234	04:36:22.30	-10:22:34.1	0.0352	154.62	14.757	627.88 ± 22.81
6dFGS gJ043659.1-301042	04:36:59.14	-30:10:41.9	0.0999	459.64	18.026	38.22 ± 5.35
6dFGS gJ044040.4-411044	04:40:40.35	-41:10:43.7	0.0327	143.58	17.19	276.32 ± 8.53
6dFGS gJ044720.7-050814	04:47:20.73	-05:08:14.0	0.0449	198.92	15.93	348.0 ± 15.53
6dFGS gJ044739.0-040330	04:47:38.97	-04:03:29.8	0.0815	370.46	16.723	296.74 ± 13.02
6dFGS gJ045230.1-295335	04:52:30.08	-29:53:35.2	0.2858	1468.46	17.336	14.22 ± 1.51
6dFGS gJ045557.5-145641	04:55:57.52	-14:56:41.2	0.1368	644.82	17.933	89.33 ± 6.16
6dFGS gJ050744.0-465231	05:07:43.97	-46:52:30.6	0.1207	563.37	18.934	19.08 ± 1.83
6dFGS gJ052210.1-422255	05:22:10.06	-42:22:54.7	0.2608	1322.19	18.744	20.48 ± 2.93
6dFGS gJ052349.5-330551	05:23:49.52	-33:05:50.5	0.2027	994.99	18.676	22.68 ± 2.25
6dFGS gJ053724.5-381759	05:37:24.48	-38:17:58.7	0.3315	1743.12	18.811	12.54 ± 2.48
6dFGS gJ054158.0-373837	05:41:58.03	-37:38:37.1	0.2237	1111.12	18.121	33.49 ± 2.63
6dFGS gJ054914.9-242552	05:49:14.91	-24:25:51.6	0.045	199.42	17.179	149.75 ± 5.89
6dFGS gJ055426.4-345341	05:54:26.42	-34:53:40.6	0.0818	372.09	17.903	90.21 ± 5.57
6dFGS gJ060917.5-560658	06:09:17.48	-56:06:58.4	0.0318	139.53	16.731	104.85 ± 6.89
6dFGS gJ061549.6-582605	06:15:49.59	-58:26:5.1	0.0549	245.05	16.78	72.49 ± 4.44
6dFGS gJ062233.5-231742	06:22:33.53	-23:17:41.7	0.0378	166.49	14.663	250.0 ± 8.04
6dFGS gJ063940.8-512515	06:39:40.77	-51:25:14.5	0.1085	502.06	16.275	66.6 ± 4.75
6dFGS gJ064157.7-431742	06:41:57.71	-43:17:41.8	0.0611	273.97	16.005	85.53 ± 3.72
6dFGS gJ065017.5-380514	06:50:17.46	-38:05:13.5	0.03	131.47	15.591	156.76 ± 6.49
6dFGS gJ065654.3-631536	06:56:54.25	-63:15:35.5	0.0355	156.23	15.84	141.76 ± 6.65
6dFGS gJ070841.5-493306	07:08:41.50	-49:33:6.4	0.0406	179.13	16.496	419.09 ± 12.79
6dFGS gJ071033.0-535752	07:10:32.99	-53:57:52.3	0.0481	213.78	16.476	133.95 ± 6.49
6dFGS gJ082003.1-174151	08:20:3.10	-17:41:50.9	0.0737	333.36	17.381	46.02 ± 3.35
6dFGS gJ084219.1-034931	08:42:19.11	-03:49:31.4	0.3566	1897.69	18.028	48.22 ± 4.8
6dFGS gJ084235.0-704249	08:42:34.99	-70:42:48.5	0.1096	507.67	17.38	45.4 ± 5.34
6dFGS gJ084510.2-073205	08:45:10.24	-07:32:5.3	0.1036	477.96	17.448	57.04 ± 5.97
6dFGS gJ084628.7-121409	08:46:28.67	-12:14:9.3	0.1078	498.71	17.099	43.25 ± 4.47
6dFGS gJ084951.7-235125	08:49:51.67	-23:51:25.3	0.1272	596.16	17.958	65.29 ± 4.35
6dFGS gJ085028.0-031817	08:50:27.96	-03:18:16.7	0.1623	777.36	17.967	89.12 ± 6.44
6dFGS gJ095219.1-013644	09:52:19.08	-01:36:43.5	0.0196	85.19	15.659	586.17 ± 23.05
6dFGS gJ101134.8-452830	10:11:34.82	-45:28:29.8	0.0574	256.34	17.372	33.76 ± 3.57
6dFGS gJ101420.7-041841	10:14:20.69	-04:18:40.5	0.0583	260.8	16.217	303.39 ± 7.56
6dFGS gJ101503.2-165214	10:15:3.20	-16:52:14.0	0.4317	2377.35	17.751	56.34 ± 5.75
6dFGS gJ103214.1-160960	10:32:14.13	-16:09:59.7	0.0529	235.6	15.936	74.59 ± 5.99
6dFGS gJ103257.0-270730	10:32:57.04	-27:07:30.3	0.0711	320.84	16.715	103.67 ± 6.21
6dFGS gJ104203.0-380058	10:42:3.00	-38:00:57.8	0.1169	544.12	17.155	36.2 ± 2.2
6dFGS gJ104208.9-400032	10:42:8.92	-40:00:31.6	0.386	2082.99	18.845	19.34 ± 2.19
6dFGS gJ104448.7-182653	10:44:48.72	-18:26:53.2	0.1132	525.59	17.933	65.9 ± 3.72
6dFGS gJ104833.8-390238	10:48:33.84	-39:02:37.9	0.0447	197.8	16.757	133.92 ± 6.11
6dFGS gJ105719.5-080541	10:57:19.45	-08:05:40.5	0.222	1101.66	18.125	27.63 ± 2.59
6dFGS gJ105727.9-403941	10:57:27.87	-40:39:40.6	0.3981	2160.24	18.006	52.02 ± 4.48
6dFGS gJ114353.8-361518	11:43:53.82	-36:15:18.4	0.1016	468.36	17.442	43.73 ± 5.4
6dFGS gJ114738.9-214508	11:47:38.87	-21:45:7.7	0.2191	1085.52	18.059	35.08 ± 3.38

Table 3.1: continued.

Name	RA	Dec	Redshift	D_L	B	Flux(5100Å)
-	(hh:mm:ss)	(dd:mm:ss)	-	(Mpc)	(mag)	(10^{-17} erg s^{-1} cm^{-2} Å^{-1})
6dFGS gJ120624.2-243548	12:06:24.23	-24:35:48.1	0.1602	766.41	18.051	39.72 ± 2.75
6dFGS gJ122417.5-181205	12:24:17.45	-18:12:4.9	0.107	494.91	18.049	14.0 ± 1.6
6dFGS gJ122527.2-041857	12:25:27.19	-04:18:57.3	0.1371	646.6	17.397	88.49 ± 4.38
6dFGS gJ123124.9-165350	12:31:24.89	-16:53:49.9	0.1026	473.03	17.122	97.98 ± 6.01
6dFGS gJ123817.2-344028	12:38:17.20	-34:40:28.2	0.0763	345.46	16.367	37.04 ± 2.6
6dFGS gJ125424.8-282632	12:54:24.82	-28:26:31.5	0.0697	314.17	16.349	59.08 ± 4.19
6dFGS gJ125706.4-443520	12:57:6.43	-44:35:20.0	0.0967	443.96	16.731	103.7 ± 5.93
6dFGS gJ125747.9-235044	12:57:47.93	-23:50:44.2	0.1194	556.54	17.366	118.01 ± 8.38
6dFGS gJ132158.2-310426	13:21:58.19	-31:04:25.7	0.0453	200.79	17.573	42.14 ± 6.3
6dFGS gJ132904.6-292556	13:29:4.60	-29:25:56.1	0.3021	1565.08	19.388	16.71 ± 1.78
6dFGS gJ133739.6-090228	13:37:39.59	-09:02:28.1	0.0802	364.42	17.381	24.29 ± 3.06
6dFGS gJ134054.2-352111	13:40:54.24	-35:21:11.0	0.2777	1420.67	18.153	29.79 ± 3.86
6dFGS gJ134524.7-025940	13:45:24.70	-02:59:39.7	0.0853	388.64	17.482	76.14 ± 5.44
6dFGS gJ135129.5-181347	13:51:29.51	-18:13:46.5	0.0122	52.82	15.696	194.4 ± 8.06
6dFGS gJ135439.5-421457	13:54:39.48	-42:14:56.5	0.0762	345.24	16.846	193.89 ± 9.74
6dFGS gJ140722.0-312058	14:07:22.00	-31:20:57.8	0.0747	337.77	17.052	62.45 ± 7.15
6dFGS gJ141048.7-364412	14:10:48.73	-36:44:11.9	0.0626	280.6	16.659	181.51 ± 6.01
6dFGS gJ142350.2-092318	14:23:50.16	-09:23:17.8	0.0682	307.34	17.124	54.0 ± 4.0
6dFGS gJ143438.4-425405	14:34:38.43	-42:54:5.3	0.1147	532.9	17.92	29.47 ± 3.57
6dFGS gJ144718.7-380222	14:47:18.72	-38:02:21.8	0.0638	286.61	16.948	78.35 ± 4.45
6dFGS gJ145712.7-131503	14:57:12.71	-13:15:3.4	0.2543	1284.95	17.724	49.11 ± 5.47
6dFGS gJ150012.8-724840	15:00:12.81	-72:48:40.3	0.1414	668.46	17.945	43.66 ± 3.77
6dFGS gJ151159.8-211902	15:11:59.79	-21:19:1.6	0.0445	196.86	15.333	303.24 ± 13.05
6dFGS gJ151222.5-333334	15:12:22.47	-33:33:34.2	0.0235	102.55	15.152	87.8 ± 4.74
6dFGS gJ151515.2-782012	15:15:15.20	-78:20:12.0	0.2586	1309.83	17.134	71.5 ± 3.62
6dFGS gJ152228.7-064441	15:22:28.72	-06:44:40.9	0.0831	378.25	16.595	144.74 ± 5.6
6dFGS gJ153846.6-102628	15:38:46.56	-10:26:27.9	0.1944	949.76	17.422	86.4 ± 4.77
6dFGS gJ161519.1-093613	16:15:19.08	-09:36:13.3	0.065	291.9	16.545	461.52 ± 20.46
6dFGS gJ161610.8-101406	16:16:10.78	-10:14:6.0	0.0775	351.51	17.059	103.58 ± 8.45
6dFGS gJ162848.4-030408	16:28:48.36	-03:04:7.8	0.0929	425.65	16.881	130.5 ± 13.86
6dFGS gJ163626.8-211835	16:36:26.79	-21:18:34.8	0.0266	116.23	16.591	280.02 ± 27.78
6dFGS gJ163830.9-205525	16:38:30.92	-20:55:24.6	0.0268	117.36	15.053	592.21 ± 26.32
6dFGS gJ164610.4-112404	16:46:10.39	-11:24:4.2	0.074	334.76	15.93	418.84 ± 19.75
6dFGS gJ172916.3-685442	17:29:16.25	-68:54:41.5	0.0483	214.58	16.525	150.4 ± 9.63
6dFGS gJ183450.8-572422	18:34:50.81	-57:24:22.1	0.0547	244.15	16.567	85.69 ± 5.32
6dFGS gJ184942.1-551310	18:49:42.12	-55:13:9.5	0.0502	223.14	16.754	99.67 ± 6.42
6dFGS gJ192631.1-191703	19:26:31.07	-19:17:3.3	0.0835	379.93	16.723	182.14 ± 9.86
6dFGS gJ193733.0-061305	19:37:33.01	-06:13:4.8	0.0103	44.49	13.59	1229.53 ± 34.68
6dFGS gJ193819.6-432646	19:38:19.58	-43:26:46.2	0.0791	358.98	16.995	145.23 ± 5.7
6dFGS gJ194335.3-163108	19:43:35.25	-16:31:8.2	0.0462	204.9	15.771	150.49 ± 5.22
6dFGS gJ194909.3-103425	19:49:9.28	-10:34:25.0	0.024	104.76	14.311	1216.09 ± 29.03
6dFGS gJ195705.3-414117	19:57:5.25	-41:41:16.9	0.3737	2005.21	18.335	22.23 ± 3.03
6dFGS gJ200553.0-413442	20:05:53.00	-41:34:42.1	0.0796	361.5	17.774	118.23 ± 5.55
6dFGS gJ202104.4-223518	20:21:4.38	-22:35:18.3	0.1849	897.99	17.26	50.67 ± 3.9
6dFGS gJ202557.4-482226	20:25:57.37	-48:22:26.4	0.0671	301.82	15.579	110.46 ± 6.84
6dFGS gJ203927.2-301852	20:39:27.19	-30:18:52.2	0.0791	358.88	17.573	38.74 ± 3.82
6dFGS gJ204513.1-301027	20:45:13.10	-30:10:26.9	0.1112	515.92	18.105	55.76 ± 6.72
6dFGS gJ205920.7-314735	20:59:20.74	-31:47:34.8	0.0734	331.71	16.42	155.37 ± 6.42

Table 3.1: continued.

Name	RA	Dec	Redshift	D_L	B	Flux(5100Å)
-	(hh:mm:ss)	(dd:mm:ss)	-	(Mpc)	(mag)	(10^{-17} erg s^{-1} cm^{-2} Å^{-1})
6dFGS gJ205933.0-513601	20:59:33.04	-51:36:0.5	0.3141	1637.32	18.238	13.29 ± 2.24
6dFGS gJ211224.6-412854	21:12:24.60	-41:28:53.8	0.3489	1850.06	18.44	22.06 ± 2.24
6dFGS gJ211524.9-141706	21:15:24.88	-14:17:5.7	0.2707	1379.57	17.836	41.04 ± 4.04
6dFGS gJ213333.4-355848	21:33:33.36	-35:58:48.4	0.3496	1854.58	18.235	15.83 ± 3.16
6dFGS gJ213529.5-623007	21:35:29.50	-62:30:7.2	0.061	273.14	16.629	162.3 ± 5.92
6dFGS gJ213632.0-011626	21:36:32.02	-01:16:26.1	0.2739	1398.35	18.912	14.5 ± 2.34
6dFGS gJ213748.0-111204	21:37:47.95	-11:12:3.6	0.1131	525.01	17.841	17.99 ± 2.25
6dFGS gJ214306.1-295817	21:43:6.10	-29:58:16.8	0.1203	561.22	17.458	103.87 ± 6.72
6dFGS gJ214505.8-692231	21:45:5.75	-69:22:30.9	0.089	406.75	17.804	58.25 ± 8.66
6dFGS gJ215526.7-121032	21:55:26.74	-12:10:31.7	0.086	392.02	18.874	25.99 ± 3.7
6dFGS gJ215723.2-312307	21:57:23.17	-31:23:6.5	0.0851	387.94	17.902	21.2 ± 3.07
6dFGS gJ220755.6-282406	22:07:55.62	-28:24:6.2	0.178	861.19	18.363	15.31 ± 1.18
6dFGS gJ221611.2-394734	22:16:11.23	-39:47:33.7	0.247	1242.77	18.351	29.64 ± 2.45
6dFGS gJ221653.2-445157	22:16:53.21	-44:51:57.0	0.1354	637.63	17.733	95.59 ± 6.56
6dFGS gJ221800.2-395723	22:18:0.19	-39:57:22.7	0.2443	1227.65	18.706	21.71 ± 2.77
6dFGS gJ222903.5-140106	22:29:3.51	-14:01:6.2	0.2358	1179.27	17.715	39.36 ± 3.36
6dFGS gJ224237.7-384516	22:42:37.66	-38:45:16.3	0.2204	1092.8	18.448	13.46 ± 1.88
6dFGS gJ224458.2-182250	22:44:58.19	-18:22:49.5	0.1977	967.42	17.974	29.41 ± 2.93
6dFGS gJ224520.3-465211	22:45:20.30	-46:52:11.4	0.2	980.17	16.991	345.8 ± 11.53
6dFGS gJ225014.1-115201	22:50:14.06	-11:52:0.8	0.1177	548.25	17.917	28.96 ± 2.68
6dFGS gJ225321.6-511802	22:53:21.60	-51:18:2.2	0.1147	533.02	18.841	14.32 ± 3.32
6dFGS gJ231103.4-202221	23:11:3.36	-20:22:20.6	0.1212	565.62	17.643	25.76 ± 5.26
6dFGS gJ234042.0-594132	23:40:42.00	-59:41:32.3	0.3789	2037.65	18.686	10.87 ± 2.58
6dFGS gJ234120.6-592359	23:41:20.64	-59:23:58.6	0.203	996.68	18.761	15.68 ± 2.3
6dFGS gJ234614.6-490952	23:46:14.64	-49:09:51.8	0.2028	995.67	18.181	26.43 ± 2.16
6dFGS gJ235808.5-102843	23:58:8.49	-10:28:42.8	0.1673	803.97	18.176	24.14 ± 2.2

Notes. Column (1) Name in the 6dFGS. (2) Right Ascension. (3) Declination. (4) Redshift. (5) Luminosity distance. (6) Magnitude on B-band. (7) Mean flux density at 5100 Å.

Table 3.2: FWHM and flux of Hβ and [O III] lines and their flux ratio in the 6dFGS NLS1 sample.

Name	FWHM(Hβ)	FWHM([O III])	Flux(Hβ)	Flux([O III])	Flux ratio [O III]/Hβ
-	(km s^{-1})	(km s^{-1})	(10^{-17} erg s^{-1} cm^{-2})	(10^{-17} erg s^{-1} cm^{-2})	-
6dFGS gJ000040.3-054101	1012.5 ± 93.0	714.9 ± 33.0	1428.91 ± 80.23	1143.99 ± 53.88	0.8 ± 0.06
6dFGS gJ001302.3-323830	2189.9 ± 124.4	586.5 ± 52.9	1671.05 ± 29.84	503.24 ± 18.57	0.3 ± 0.01
6dFGS gJ001521.6-150951	1120.1 ± 85.4	362.5 ± 36.3	1055.21 ± 40.33	435.65 ± 23.56	0.41 ± 0.03
6dFGS gJ001641.9-312657	2237.4 ± 72.5	950.4 ± 212.2	2106.58 ± 31.16	123.75 ± 17.77	0.06 ± 0.01
6dFGS gJ002121.6-205018	1533.2 ± 62.2	909.7 ± 137.3	2192.49 ± 35.24	212.2 ± 22.52	0.1 ± 0.01
6dFGS gJ002249.2-103956	1852.7 ± 71.3	761.1 ± 42.0	1763.16 ± 28.29	912.99 ± 20.65	0.52 ± 0.01
6dFGS gJ003000.5-202856	1172.9 ± 58.7	379.6 ± 50.6	342.54 ± 13.22	159.86 ± 10.4	0.47 ± 0.04
6dFGS gJ003211.0-324205	1124.7 ± 73.5	477.7 ± 17.4	886.78 ± 20.02	376.26 ± 15.64	0.42 ± 0.02
6dFGS gJ003740.0-542030	1558.5 ± 197.3	623.1 ± 59.7	651.08 ± 34.94	520.66 ± 21.84	0.8 ± 0.05
6dFGS gJ003915.9-511702	1275.2 ± 0.0	476.2 ± 0.0	13151.23 ± 86.59	2063.33 ± 58.66	0.16 ± 0.0
6dFGS gJ004039.2-371317	1653.5 ± 101.2	446.0 ± 30.0	2927.62 ± 73.38	2266.46 ± 50.91	0.77 ± 0.03
6dFGS gJ004324.9-165557	1895.5 ± 77.7	736.2 ± 91.3	4715.64 ± 74.52	685.55 ± 54.1	0.15 ± 0.01
6dFGS gJ010313.2-480445	1769.5 ± 132.5	481.1 ± 148.5	1146.12 ± 43.67	90.57 ± 22.7	0.08 ± 0.02
6dFGS gJ011442.5-513614	753.4 ± 39.7	406.4 ± 35.2	834.07 ± 15.62	166.91 ± 8.49	0.2 ± 0.01
6dFGS gJ011730.6-382630	903.7 ± 35.3	558.4 ± 123.0	1836.27 ± 42.93	281.85 ± 27.26	0.15 ± 0.02
6dFGS gJ011935.7-282132	1494.4 ± 96.3	1668.6 ± 295.0	2256.52 ± 33.42	304.93 ± 27.44	0.14 ± 0.01
6dFGS gJ012237.5-264646	1350.0 ± 136.2	1034.9 ± 84.1	281.06 ± 15.02	192.14 ± 9.25	0.68 ± 0.05

Table 3.2: continued.

Name	FWHM(Hβ)	FWHM([O III])	Flux(Hβ)	Flux([O III])	Flux ratio [O III]/Hβ
-	(km s^{-1})	(km s^{-1})	(10^{-17} erg s^{-1} cm^{-2})	(10^{-17} erg s^{-1} cm^{-2})	-
6dFGS gJ013117.1-395631	2159.6 ± 68.9	1295.1 ± 111.0	1269.64 ± 22.1	271.82 ± 14.31	0.21 ± 0.01
6dFGS gJ013137.9-294229	1743.8 ± 118.1	615.7 ± 70.9	500.31 ± 21.93	218.91 ± 13.48	0.44 ± 0.03
6dFGS gJ013335.0-210959	624.4 ± 54.1	519.7 ± 0.0	1035.05 ± 28.83	1055.68 ± 21.56	1.02 ± 0.04
6dFGS gJ013546.4-353915	1063.2 ± 46.0	946.3 ± 103.6	5187.55 ± 75.45	519.75 ± 40.28	0.1 ± 0.01
6dFGS gJ013809.5-010920	1902.4 ± 70.7	1308.4 ± 130.7	2830.4 ± 30.16	438.75 ± 25.07	0.16 ± 0.01
6dFGS gJ014222.3-352541	1105.6 ± 42.5	536.7 ± 15.3	3451.87 ± 72.2	1293.14 ± 43.85	0.37 ± 0.01
6dFGS gJ015251.6-523824	1499.5 ± 65.6	455.0 ± 0.0	2230.83 ± 49.32	1303.85 ± 26.95	0.58 ± 0.02
6dFGS gJ015930.7-112859	2071.0 ± 69.6	418.9 ± 36.3	4612.25 ± 93.1	1198.4 ± 61.06	0.26 ± 0.01
6dFGS gJ020039.1-084555	1901.7 ± 241.0	410.3 ± 81.1	628.51 ± 41.47	137.56 ± 21.09	0.22 ± 0.04
6dFGS gJ020349.0-124717	1235.9 ± 83.3	738.5 ± 70.4	2074.37 ± 76.63	678.21 ± 43.38	0.33 ± 0.02
6dFGS gJ021201.5-020154	1965.2 ± 133.9	613.3 ± 66.7	573.81 ± 15.3	150.37 ± 9.39	0.26 ± 0.02
6dFGS gJ021218.3-073720	2404.9 ± 184.0	583.8 ± 80.1	1516.71 ± 38.07	444.34 ± 30.53	0.29 ± 0.02
6dFGS gJ021355.1-055121	1770.4 ± 245.2	601.6 ± 42.2	1163.51 ± 49.09	1120.94 ± 30.14	0.96 ± 0.05
6dFGS gJ021738.1-300448	1585.8 ± 88.2	513.2 ± 55.3	1347.61 ± 33.81	500.23 ± 18.68	0.37 ± 0.02
6dFGS gJ022219.4-533239	1750.5 ± 68.2	626.2 ± 44.2	3381.65 ± 59.58	1277.71 ± 35.68	0.38 ± 0.01
6dFGS gJ022815.2-405715	1720.8 ± 67.4	1299.5 ± 81.7	12057.81 ± 93.54	1272.52 ± 55.88	0.11 ± 0.0
6dFGS gJ023005.5-085953	894.2 ± 0.0	482.4 ± 34.4	44669.93 ± 175.5	3872.29 ± 111.05	0.09 ± 0.0
6dFGS gJ023927.6-534508	1999.2 ± 77.9	373.3 ± 40.6	1231.39 ± 19.27	69.53 ± 10.35	0.06 ± 0.01
6dFGS gJ023956.2-111813	2096.6 ± 194.5	570.0 ± 70.3	955.39 ± 22.76	157.29 ± 16.92	0.16 ± 0.02
6dFGS gJ025228.4-592243	918.3 ± 70.7	567.4 ± 25.4	713.67 ± 21.04	320.71 ± 11.51	0.45 ± 0.02
6dFGS gJ030735.3-725003	2258.6 ± 286.5	381.4 ± 39.5	5052.64 ± 99.51	1157.73 ± 52.21	0.23 ± 0.01
6dFGS gJ031558.9-290126	1464.6 ± 51.6	523.9 ± 60.1	3228.77 ± 46.07	422.91 ± 36.75	0.13 ± 0.01
6dFGS gJ034713.9-132547	2268.5 ± 80.1	734.2 ± 41.6	1963.12 ± 32.73	547.91 ± 20.7	0.28 ± 0.01
6dFGS gJ035056.7-102559	1420.4 ± 97.8	1379.1 ± 127.8	2137.87 ± 60.42	629.53 ± 41.93	0.29 ± 0.02
6dFGS gJ035107.6-052637	1228.3 ± 52.3	642.2 ± 50.9	1940.85 ± 43.76	590.15 ± 27.52	0.3 ± 0.02
6dFGS gJ035432.8-134008	2140.4 ± 71.3	632.5 ± 57.5	3702.18 ± 69.13	777.66 ± 41.29	0.21 ± 0.01
6dFGS gJ040024.4-250044	1094.7 ± 109.8	1240.0 ± 260.5	1145.56 ± 40.43	289.75 ± 34.12	0.25 ± 0.03
6dFGS gJ041307.1-005017	2133.2 ± 634.7	470.7 ± 41.3	2351.74 ± 93.51	1023.88 ± 59.15	0.44 ± 0.03
6dFGS gJ042020.4-355100	1769.2 ± 99.6	899.8 ± 311.7	2128.37 ± 42.87	128.13 ± 27.0	0.06 ± 0.01
6dFGS gJ042021.7-053054	673.4 ± 35.5	408.6 ± 40.0	1857.92 ± 44.72	350.89 ± 31.39	0.19 ± 0.02
6dFGS gJ042256.6-185442	1223.3 ± 157.0	730.9 ± 64.8	1881.12 ± 66.8	2555.7 ± 48.98	1.36 ± 0.05
6dFGS gJ043526.5-164346	2204.6 ± 80.6	446.0 ± 27.9	3654.91 ± 47.57	1124.34 ± 25.7	0.31 ± 0.01
6dFGS gJ043622.3-102234	2144.4 ± 47.5	851.8 ± 0.0	40238.4 ± 233.95	27610.53 ± 144.74	0.69 ± 0.01
6dFGS gJ043659.1-301042	1373.8 ± 169.9	622.5 ± 64.4	533.68 ± 48.01	487.06 ± 32.69	0.91 ± 0.1
6dFGS gJ044040.4-411044	873.6 ± 48.6	471.2 ± 0.0	9375.99 ± 104.32	5905.82 ± 88.69	0.63 ± 0.01
6dFGS gJ044720.7-050814	772.5 ± 57.4	562.5 ± 13.1	11500.86 ± 241.52	3862.63 ± 157.28	0.34 ± 0.02
6dFGS gJ044739.0-040330	1212.2 ± 105.2	543.2 ± 98.4	7368.81 ± 218.55	715.85 ± 116.32	0.1 ± 0.02
6dFGS gJ045230.1-295335	1168.0 ± 125.3	680.4 ± 33.3	562.19 ± 13.53	288.52 ± 7.95	0.51 ± 0.02
6dFGS gJ045557.5-145641	2039.8 ± 69.7	861.1 ± 45.1	4740.1 ± 51.52	944.02 ± 36.41	0.2 ± 0.01
6dFGS gJ050744.0-465231	899.8 ± 49.0	611.6 ± 35.6	625.55 ± 16.94	860.5 ± 11.69	1.38 ± 0.04
6dFGS gJ052210.1-422255	1039.4 ± 83.3	543.4 ± 63.3	657.98 ± 32.0	444.06 ± 24.03	0.67 ± 0.05
6dFGS gJ052349.5-330551	1424.4 ± 67.3	569.5 ± 46.9	1932.02 ± 25.67	456.86 ± 17.42	0.24 ± 0.01
6dFGS gJ053724.5-381759	1589.7 ± 125.9	441.0 ± 61.0	1018.4 ± 26.16	358.3 ± 18.91	0.35 ± 0.02
6dFGS gJ054158.0-373837	1152.2 ± 46.7	719.2 ± 53.1	1558.73 ± 23.84	392.2 ± 19.79	0.25 ± 0.01
6dFGS gJ054914.9-242552	1446.9 ± 124.8	561.9 ± 23.9	2967.37 ± 104.33	3232.01 ± 64.35	1.09 ± 0.04
6dFGS gJ055426.4-345341	1211.0 ± 50.5	452.2 ± 12.7	3428.2 ± 73.14	1105.67 ± 38.0	0.32 ± 0.01
6dFGS gJ060917.5-560658	684.5 ± 48.9	474.7 ± 20.7	4616.59 ± 87.36	4033.98 ± 54.23	0.87 ± 0.02
6dFGS gJ061549.6-582605	1242.3 ± 69.1	463.9 ± 49.7	2337.32 ± 41.22	423.21 ± 29.31	0.18 ± 0.01
6dFGS gJ062233.5-231742	1067.7 ± 69.1	565.5 ± 40.8	5941.16 ± 102.68	1910.81 ± 68.13	0.32 ± 0.01
6dFGS gJ063940.8-512515	1820.9 ± 108.0	795.6 ± 50.7	3488.25 ± 39.2	1624.59 ± 26.58	0.47 ± 0.01
6dFGS gJ064157.7-431742	761.3 ± 78.9	462.0 ± 0.0	2133.57 ± 37.4	974.92 ± 28.88	0.46 ± 0.02
6dFGS gJ065017.5-380514	1653.6 ± 54.3	377.8 ± 45.3	4979.88 ± 68.42	848.82 ± 46.39	0.17 ± 0.01
6dFGS gJ065654.3-631536	1949.5 ± 103.6	757.1 ± 92.1	2665.89 ± 67.48	883.7 ± 46.06	0.33 ± 0.02
6dFGS gJ070841.5-493306	969.6 ± 0.0	1035.6 ± 120.8	12451.54 ± 152.94	1270.95 ± 110.91	0.1 ± 0.01
6dFGS gJ071033.0-535752	2305.4 ± 134.8	746.1 ± 51.6	3865.88 ± 96.86	4161.1 ± 80.35	1.08 ± 0.03
6dFGS gJ082003.1-174151	1400.1 ± 89.9	453.2 ± 61.0	1413.22 ± 37.65	310.51 ± 19.57	0.22 ± 0.02
6dFGS gJ084219.1-034931	1484.8 ± 58.1	576.7 ± 0.0	3896.91 ± 52.49	2269.55 ± 33.23	0.58 ± 0.01
6dFGS gJ084235.0-704249	2183.0 ± 294.9	618.2 ± 68.5	1227.42 ± 59.94	561.56 ± 36.16	0.46 ± 0.04
6dFGS gJ084510.2-073205	2008.9 ± 141.9	443.3 ± 55.9	2575.61 ± 40.83	720.96 ± 34.54	0.28 ± 0.01
6dFGS gJ084628.7-121409	904.2 ± 48.6	526.8 ± 0.0	1726.71 ± 39.2	2227.03 ± 29.38	1.29 ± 0.03
6dFGS gJ084951.7-235125	1066.3 ± 46.8	776.5 ± 29.6	3882.67 ± 45.79	1624.23 ± 31.19	0.42 ± 0.01
6dFGS gJ085028.0-031817	2254.0 ± 72.2	757.6 ± 23.3	7390.12 ± 87.95	3385.72 ± 58.3	0.46 ± 0.01
6dFGS gJ095219.1-013644	691.1 ± 43.3	671.0 ± 46.0	42605.1 ± 236.43	55271.96 ± 177.38	1.3 ± 0.01
6dFGS gJ101134.8-452830	1907.3 ± 137.6	555.6 ± 28.3	1008.35 ± 43.41	630.02 ± 26.3	0.62 ± 0.04
6dFGS gJ101420.7-041841	1704.2 ± 87.2	551.6 ± 38.2	11550.44 ± 179.5	3107.02 ± 93.69	0.27 ± 0.01
6dFGS gJ101503.2-165214	2168.6 ± 84.5	1222.6 ± 67.6	4675.71 ± 48.52	865.04 ± 28.03	0.19 ± 0.01

Table 3.2: continued.

Name	FWHM(Hβ)	FWHM([O III])	Flux(Hβ)	Flux([O III])	Flux ratio [O III]/Hβ
-	(km s^{-1})	(km s^{-1})	(10^{-17} erg s^{-1} cm^{-2})	(10^{-17} erg s^{-1} cm^{-2})	-
6dFGS gJ103214.1-160960	1045.8 ± 149.0	461.5 ± 42.7	1448.84 ± 93.05	894.26 ± 52.98	0.62 ± 0.05
6dFGS gJ103257.0-270730	1242.8 ± 69.9	603.4 ± 8.6	3916.27 ± 61.92	3216.93 ± 40.38	0.82 ± 0.02
6dFGS gJ104203.0-380058	1022.1 ± 50.3	661.6 ± 45.7	2566.56 ± 27.58	658.1 ± 16.89	0.26 ± 0.01
6dFGS gJ104208.9-400032	1662.3 ± 117.8	491.2 ± 47.2	1184.9 ± 22.76	419.9 ± 19.46	0.35 ± 0.02
6dFGS gJ104448.7-182653	1079.8 ± 32.1	436.8 ± 0.0	3960.84 ± 42.88	2028.83 ± 31.46	0.51 ± 0.01
6dFGS gJ104833.8-390238	1822.7 ± 49.7	442.4 ± 0.0	8707.91 ± 97.01	4763.48 ± 64.82	0.55 ± 0.01
6dFGS gJ105719.5-080541	1734.4 ± 182.7	561.3 ± 22.6	906.59 ± 32.7	470.79 ± 19.82	0.52 ± 0.03
6dFGS gJ105727.9-403941	1633.1 ± 52.0	660.7 ± 56.5	2998.11 ± 40.71	292.64 ± 20.59	0.1 ± 0.01
6dFGS gJ114353.8-361518	1900.1 ± 115.9	670.9 ± 96.7	1533.17 ± 47.79	282.63 ± 30.74	0.18 ± 0.02
6dFGS gJ114738.9-214508	1314.4 ± 71.0	1116.7 ± 63.5	1347.79 ± 30.71	573.57 ± 20.14	0.43 ± 0.02
6dFGS gJ120624.2-243548	1466.9 ± 73.1	670.3 ± 49.0	2047.74 ± 27.6	613.34 ± 19.03	0.3 ± 0.01
6dFGS gJ122417.5-181205	2262.8 ± 195.4	527.3 ± 79.2	484.54 ± 22.03	89.0 ± 13.07	0.18 ± 0.03
6dFGS gJ122527.2-041857	1151.9 ± 8.8	1032.4 ± 39.8	6558.02 ± 42.58	1596.03 ± 32.98	0.24 ± 0.01
6dFGS gJ123124.9-165350	1738.4 ± 63.2	533.0 ± 45.4	6925.55 ± 85.71	1619.67 ± 55.26	0.23 ± 0.01
6dFGS gJ123817.2-344028	930.6 ± 166.7	451.8 ± 67.2	379.68 ± 25.09	171.25 ± 16.33	0.45 ± 0.05
6dFGS gJ125424.8-282632	1695.6 ± 70.6	548.8 ± 0.0	3828.44 ± 39.63	1582.87 ± 25.91	0.41 ± 0.01
6dFGS gJ125706.4-443520	734.9 ± 74.2	802.7 ± 62.2	1754.71 ± 44.3	601.06 ± 31.18	0.34 ± 0.02
6dFGS gJ125747.9-235044	2071.6 ± 79.4	612.2 ± 40.1	9683.5 ± 80.95	5965.45 ± 54.32	0.62 ± 0.01
6dFGS gJ132158.2-310426	2119.9 ± 166.5	935.6 ± 123.5	2048.8 ± 64.69	782.66 ± 46.06	0.38 ± 0.03
6dFGS gJ132904.6-292556	1780.4 ± 44.8	751.6 ± 45.1	1674.22 ± 14.63	804.12 ± 10.54	0.48 ± 0.01
6dFGS gJ133739.6-090228	746.7 ± 66.5	362.5 ± 45.6	710.73 ± 32.57	182.01 ± 17.03	0.26 ± 0.03
6dFGS gJ134054.2-352111	1813.8 ± 66.3	689.1 ± 58.4	3011.46 ± 45.55	589.24 ± 26.93	0.2 ± 0.01
6dFGS gJ134524.7-025940	1020.6 ± 52.2	450.4 ± 32.9	2789.83 ± 57.79	1402.49 ± 30.99	0.5 ± 0.02
6dFGS gJ135129.5-181347	895.2 ± 24.4	386.3 ± 0.0	6144.27 ± 112.09	2736.41 ± 95.71	0.45 ± 0.02
6dFGS gJ135439.5-421457	1685.3 ± 45.9	363.6 ± 23.2	18089.01 ± 122.71	6346.19 ± 74.25	0.35 ± 0.0
6dFGS gJ140722.0-312058	886.0 ± 113.0	602.2 ± 62.3	1955.55 ± 81.24	830.0 ± 49.7	0.42 ± 0.03
6dFGS gJ141048.7-364412	1413.0 ± 64.6	548.8 ± 12.8	6635.38 ± 80.47	2598.59 ± 51.44	0.39 ± 0.01
6dFGS gJ142350.2-092318	1322.8 ± 157.5	458.7 ± 25.9	2043.07 ± 63.62	1013.35 ± 33.11	0.5 ± 0.02
6dFGS gJ143438.4-425405	1085.1 ± 70.8	790.2 ± 0.0	1841.03 ± 49.54	1929.53 ± 35.57	1.05 ± 0.03
6dFGS gJ144718.7-380222	1882.0 ± 69.5	548.2 ± 0.0	4193.37 ± 53.98	2299.31 ± 30.54	0.55 ± 0.01
6dFGS gJ145712.7-131503	1365.1 ± 109.8	545.7 ± 248.8	2581.56 ± 63.41	150.12 ± 31.8	0.06 ± 0.01
6dFGS gJ150012.8-724840	1503.4 ± 84.7	601.1 ± 112.9	2793.59 ± 36.49	269.9 ± 22.69	0.1 ± 0.01
6dFGS gJ151159.8-211902	1061.0 ± 80.1	468.3 ± 0.0	17158.49 ± 134.2	18599.7 ± 87.02	1.08 ± 0.01
6dFGS gJ151222.5-333334	1673.4 ± 88.6	992.9 ± 63.4	2925.65 ± 69.87	1749.77 ± 42.69	0.6 ± 0.02
6dFGS gJ151515.2-782012	1603.2 ± 48.1	467.0 ± 7.7	6132.02 ± 44.45	3716.8 ± 33.74	0.61 ± 0.01
6dFGS gJ152228.7-064441	1116.7 ± 20.3	813.2 ± 15.4	10016.59 ± 69.5	2730.89 ± 47.4	0.27 ± 0.01
6dFGS gJ153846.6-102628	1434.8 ± 55.0	491.7 ± 44.7	3330.42 ± 39.42	662.8 ± 27.15	0.2 ± 0.01
6dFGS gJ161519.1-093613	1514.9 ± 61.9	459.6 ± 0.0	37935.63 ± 257.69	21406.16 ± 186.36	0.56 ± 0.01
6dFGS gJ161610.8-101406	2045.3 ± 115.0	451.3 ± 44.4	3700.27 ± 89.35	1035.62 ± 50.99	0.28 ± 0.02
6dFGS gJ162848.4-030408	1567.8 ± 54.6	447.7 ± 45.8	9771.04 ± 103.64	1298.0 ± 64.58	0.13 ± 0.01
6dFGS gJ163626.8-211835	1571.2 ± 104.8	762.8 ± 45.0	17033.57 ± 391.3	9262.67 ± 274.88	0.54 ± 0.02
6dFGS gJ163830.9-205525	1471.4 ± 36.4	666.7 ± 38.8	49508.88 ± 563.89	21256.9 ± 385.12	0.43 ± 0.01
6dFGS gJ164610.4-112404	1408.7 ± 77.4	1094.2 ± 41.8	11104.11 ± 229.24	12463.73 ± 149.09	1.12 ± 0.03
6dFGS gJ172916.3-685442	2211.6 ± 369.4	466.8 ± 51.8	5792.05 ± 176.5	1887.08 ± 126.39	0.33 ± 0.02
6dFGS gJ183450.8-572422	1527.4 ± 165.0	370.8 ± 59.8	1147.02 ± 57.33	350.88 ± 31.38	0.31 ± 0.03
6dFGS gJ184942.1-551310	2098.0 ± 54.6	370.4 ± 26.1	4799.39 ± 69.03	300.58 ± 36.93	0.06 ± 0.01
6dFGS gJ192631.1-191703	1766.4 ± 160.9	541.6 ± 47.9	3807.59 ± 74.21	927.21 ± 42.19	0.24 ± 0.01
6dFGS gJ193733.0-061305	798.3 ± 36.4	484.4 ± 0.0	58814.44 ± 512.04	67554.88 ± 360.92	1.15 ± 0.01
6dFGS gJ193819.6-432646	1773.5 ± 32.3	634.4 ± 24.6	10272.83 ± 57.11	1837.66 ± 36.47	0.18 ± 0.0
6dFGS gJ194335.3-163108	867.2 ± 47.2	374.2 ± 47.0	7916.24 ± 49.94	1393.39 ± 31.53	0.18 ± 0.0
6dFGS gJ194909.3-103425	2068.7 ± 135.5	765.2 ± 56.6	23323.21 ± 400.82	5792.11 ± 209.67	0.25 ± 0.01
6dFGS gJ195705.3-414117	1685.9 ± 60.0	996.4 ± 93.1	2137.95 ± 28.14	484.34 ± 21.33	0.23 ± 0.01
6dFGS gJ200553.0-413442	1940.0 ± 53.0	428.1 ± 0.0	9028.26 ± 66.41	3506.04 ± 31.83	0.39 ± 0.0
6dFGS gJ202104.4-223518	595.1 ± 54.5	825.5 ± 0.0	1511.16 ± 34.05	4997.54 ± 25.04	3.31 ± 0.08
6dFGS gJ202557.4-482226	1986.3 ± 68.7	551.0 ± 0.0	6603.67 ± 58.45	2879.57 ± 38.78	0.44 ± 0.01
6dFGS gJ203927.2-301852	1120.1 ± 61.2	543.8 ± 39.7	1910.46 ± 49.02	811.07 ± 31.18	0.42 ± 0.02
6dFGS gJ204513.1-301027	1627.4 ± 120.7	582.1 ± 60.8	2698.68 ± 85.0	670.78 ± 35.17	0.25 ± 0.02
6dFGS gJ205920.7-314735	708.8 ± 0.0	516.2 ± 0.0	5563.13 ± 80.59	6198.95 ± 46.15	1.11 ± 0.02
6dFGS gJ205933.0-513601	1995.9 ± 136.0	969.0 ± 74.1	840.39 ± 22.92	272.14 ± 16.48	0.32 ± 0.02
6dFGS gJ211224.6-412854	1693.4 ± 209.1	1096.1 ± 268.5	962.27 ± 25.7	143.29 ± 17.86	0.15 ± 0.02
6dFGS gJ211524.9-141706	1426.8 ± 79.6	1539.2 ± 151.2	2324.36 ± 49.21	444.01 ± 31.17	0.19 ± 0.01
6dFGS gJ213333.4-355848	1762.6 ± 87.1	2396.0 ± 151.1	1202.56 ± 23.09	221.11 ± 18.02	0.18 ± 0.02
6dFGS gJ213529.5-623007	1140.8 ± 71.8	553.8 ± 16.0	5109.97 ± 66.76	1304.4 ± 50.5	0.26 ± 0.01
6dFGS gJ213632.0-011626	1742.3 ± 80.4	461.4 ± 57.6	1227.53 ± 26.71	264.72 ± 20.15	0.22 ± 0.02
6dFGS gJ213748.0-111204	1176.6 ± 56.8	351.5 ± 12.3	1496.0 ± 33.91	474.77 ± 23.09	0.32 ± 0.02
6dFGS gJ214306.1-295817	1698.9 ± 75.3	577.3 ± 237.3	4804.26 ± 60.86	388.18 ± 53.43	0.08 ± 0.01

Table 3.2: continued.

Name	FWHM(Hβ)	FWHM([O III])	Flux(Hβ)	Flux([O III])	Flux ratio [O III]/Hβ
-	(km s^{-1})	(km s^{-1})	(10^{-17} erg s^{-1} cm^{-2})	(10^{-17} erg s^{-1} cm^{-2})	-
6dFGS gJ214505.8-692231	1019.6 ± 64.9	540.0 ± 67.4	3100.44 ± 76.64	1083.49 ± 51.02	0.35 ± 0.02
6dFGS gJ215526.7-121032	1671.7 ± 99.8	450.9 ± 51.6	1369.52 ± 40.31	278.85 ± 19.71	0.2 ± 0.02
6dFGS gJ215723.2-312307	1139.8 ± 66.1	425.7 ± 12.0	1525.14 ± 30.72	401.33 ± 18.71	0.26 ± 0.01
6dFGS gJ220755.6-282406	2137.3 ± 118.0	415.0 ± 49.9	1033.67 ± 20.01	159.99 ± 10.03	0.15 ± 0.01
6dFGS gJ221611.2-394734	1754.0 ± 107.1	1332.8 ± 668.0	1644.38 ± 25.93	47.86 ± 16.21	0.03 ± 0.01
6dFGS gJ221653.2-445157	1777.2 ± 38.2	776.5 ± 50.3	5745.1 ± 45.9	1435.62 ± 30.79	0.25 ± 0.01
6dFGS gJ221800.2-395723	1681.9 ± 112.2	1187.6 ± 114.8	1383.84 ± 27.87	344.03 ± 18.64	0.25 ± 0.01
6dFGS gJ222903.5-140106	2042.9 ± 76.9	476.1 ± 15.5	2350.66 ± 26.18	684.14 ± 19.1	0.29 ± 0.01
6dFGS gJ224237.7-384516	1569.2 ± 48.7	721.7 ± 50.0	1393.21 ± 16.24	401.95 ± 10.37	0.29 ± 0.01
6dFGS gJ224458.2-182250	1850.1 ± 138.9	408.2 ± 11.4	1777.97 ± 36.62	1114.15 ± 25.07	0.63 ± 0.02
6dFGS gJ224520.3-465211	2266.4 ± 53.9	978.0 ± 13.9	27117.95 ± 124.47	12304.27 ± 112.9	0.45 ± 0.0
6dFGS gJ225014.1-115201	1165.2 ± 89.0	435.1 ± 14.8	2054.24 ± 53.68	735.97 ± 34.25	0.36 ± 0.02
6dFGS gJ225321.6-511802	1900.7 ± 113.3	527.3 ± 101.0	1324.76 ± 37.1	158.39 ± 18.47	0.12 ± 0.01
6dFGS gJ231103.4-202221	1528.2 ± 167.2	785.6 ± 91.0	1270.4 ± 46.19	354.37 ± 30.41	0.28 ± 0.03
6dFGS gJ234042.0-594132	1535.7 ± 73.1	923.0 ± 71.7	1296.06 ± 23.59	584.62 ± 16.01	0.45 ± 0.01
6dFGS gJ234120.6-592359	1593.4 ± 106.4	570.0 ± 56.5	745.86 ± 25.59	402.31 ± 20.08	0.54 ± 0.03
6dFGS gJ234614.6-490952	2178.5 ± 127.0	488.1 ± 8.1	1551.47 ± 24.87	819.61 ± 14.77	0.53 ± 0.01
6dFGS gJ235808.5-102843	1469.7 ± 113.1	503.6 ± 26.3	932.08 ± 27.44	496.59 ± 19.85	0.53 ± 0.03

Notes. Column (1) Name in the 6dFGS. (2) FWHM of Hβ line fitted with three Gaussians. (3) FWHM of [O III] line fitted with two Gaussians. (4) Flux of Hβ line. (5) Flux of [O III] line. (6) Flux ratio of [O III] / Hβ.

Table 3.4: Luminosity at 5100 Å, luminosities of Hβ and [O III] lines, mass of central black hole, and Eddington ratio in the 6dFGS NLS1 sample.

Name	L (5100 Å)	L (Hβ)	L ([O III])	M_{BH}	ϵ_{Edd}
-	(10^{43} erg s^{-1})	(10^{40} erg s^{-1})	(10^{40} erg s^{-1})	(10^{6} $M_{\odot}$)	-
6dFGS gJ000040.3-054101	2.34 ± 0.86	31.67 ± 1.78	25.35 ± 1.19	2.3 ± 0.73	0.71 ± 0.34
6dFGS gJ001302.3-323830	21.81 ± 2.77	345.16 ± 6.16	103.95 ± 3.84	15.08 ± 3.86	1.0 ± 0.29
6dFGS gJ001521.6-150951	1.14 ± 0.31	16.13 ± 0.62	6.66 ± 0.36	3.37 ± 0.99	0.23 ± 0.09
6dFGS gJ001641.9-312657	41.47 ± 8.2	930.74 ± 13.77	54.68 ± 7.85	18.21 ± 4.95	1.58 ± 0.53
6dFGS gJ002121.6-205018	13.75 ± 1.53	206.82 ± 3.32	20.02 ± 2.12	8.85 ± 2.24	1.08 ± 0.3
6dFGS gJ002249.2-103956	43.18 ± 10.6	1081.12 ± 17.35	559.82 ± 12.66	17.08 ± 4.83	1.75 ± 0.66
6dFGS gJ003000.5-202856	3.65 ± 2.02	90.6 ± 3.5	42.28 ± 2.75	10.22 ± 3.94	0.25 ± 0.17
6dFGS gJ003211.0-324205	17.37 ± 4.53	375.46 ± 8.48	159.31 ± 6.62	12.52 ± 3.54	0.96 ± 0.37
6dFGS gJ003740.0-542030	1.71 ± 0.43	16.8 ± 0.9	13.44 ± 0.56	5.28 ± 1.51	0.22 ± 0.09
6dFGS gJ003915.9-511702	2.74 ± 0.07	24.67 ± 0.16	3.87 ± 0.11	2.23 ± 0.56	0.85 ± 0.21
6dFGS gJ004039.2-371317	0.7 ± 0.1	8.77 ± 0.22	6.79 ± 0.15	1.51 ± 0.41	0.32 ± 0.1
6dFGS gJ004324.9-165557	53.39 ± 10.06	1697.78 ± 26.83	246.82 ± 19.48	15.68 ± 4.26	2.36 ± 0.78
6dFGS gJ010313.2-480445	28.7 ± 13.42	744.58 ± 28.37	58.84 ± 14.75	6.68 ± 2.35	2.97 ± 1.74
6dFGS gJ011442.5-513614	4.12 ± 0.94	101.24 ± 1.9	20.26 ± 1.03	3.53 ± 0.97	0.81 ± 0.29
6dFGS gJ011730.6-382630	14.63 ± 2.38	276.16 ± 6.46	42.39 ± 4.1	11.69 ± 3.05	0.87 ± 0.27
6dFGS gJ011935.7-282132	64.34 ± 7.73	923.92 ± 13.68	124.85 ± 11.24	25.26 ± 6.62	1.76 ± 0.51
6dFGS gJ012237.5-264646	10.13 ± 5.54	175.53 ± 9.38	119.99 ± 5.78	3.87 ± 1.47	1.81 ± 1.21
6dFGS gJ013117.1-395631	109.78 ± 14.54	1212.9 ± 21.11	259.67 ± 13.67	78.21 ± 21.03	0.97 ± 0.29
6dFGS gJ013137.9-294229	4.74 ± 2.43	114.4 ± 5.01	50.06 ± 3.08	13.62 ± 5.02	0.24 ± 0.15
6dFGS gJ013335.0-210959	5.5 ± 0.58	45.84 ± 1.28	46.75 ± 0.95	3.54 ± 0.9	1.08 ± 0.29
6dFGS gJ013546.4-353915	10.56 ± 1.8	260.49 ± 3.79	26.1 ± 2.02	5.75 ± 1.51	1.27 ± 0.4
6dFGS gJ013809.5-010920	32.5 ± 3.83	657.96 ± 7.01	101.99 ± 5.83	19.51 ± 5.01	1.15 ± 0.33
6dFGS gJ014222.3-352541	7.0 ± 0.61	76.65 ± 1.6	28.71 ± 0.97	4.3 ± 1.08	1.13 ± 0.3
6dFGS gJ015251.6-523824	3.23 ± 0.32	32.16 ± 0.71	18.79 ± 0.39	4.65 ± 1.18	0.48 ± 0.13
6dFGS gJ015930.7-112859	11.51 ± 2.81	327.21 ± 6.6	85.02 ± 4.33	9.88 ± 2.75	0.81 ± 0.3
6dFGS gJ020039.1-084555	39.04 ± 14.72	426.63 ± 28.15	93.37 ± 14.31	23.25 ± 7.46	1.16 ± 0.58

Table 3.4: continued.

Name	L(5100Å)	L(Hβ)	L([O III])	M_{BH}	ϵ_{Edd}
-	(10^{43} erg s^{-1})	(10^{40} erg s^{-1})	(10^{40} erg s^{-1})	(10^6 $M_\odot$)	-
6dFGS gJ020349.0-124717	1.82 ± 0.23	13.58 ± 0.5	4.44 ± 0.28	2.88 ± 0.75	0.44 ± 0.13
6dFGS gJ021201.5-020154	8.53 ± 4.99	400.81 ± 10.68	105.04 ± 6.56	9.91 ± 3.93	0.6 ± 0.42
6dFGS gJ021218.3-073720	12.04 ± 1.14	127.79 ± 3.21	37.44 ± 2.57	10.51 ± 2.64	0.79 ± 0.21
6dFGS gJ021355.1-055121	6.83 ± 1.31	60.8 ± 2.57	58.57 ± 1.58	5.79 ± 1.54	0.82 ± 0.27
6dFGS gJ021738.1-300448	0.86 ± 0.29	21.44 ± 0.54	7.96 ± 0.3	2.72 ± 0.86	0.22 ± 0.1
6dFGS gJ022219.4-533239	5.03 ± 0.64	77.64 ± 1.37	29.34 ± 0.82	5.04 ± 1.29	0.69 ± 0.2
6dFGS gJ022815.2-405715	450.97 ± 35.92	11213.6 ± 86.99	1183.42 ± 51.97	58.39 ± 16.5	5.35 ± 1.57
6dFGS gJ023005.5-085953	1.29 ± 0.09	26.08 ± 0.1	2.26 ± 0.06	1.97 ± 0.51	0.45 ± 0.12
6dFGS gJ023927.6-534508	7.47 ± 3.02	390.07 ± 6.1	22.03 ± 3.28	7.47 ± 2.44	0.69 ± 0.36
6dFGS gJ023956.2-111813	4.7 ± 0.97	114.12 ± 2.72	18.79 ± 2.02	6.65 ± 1.8	0.49 ± 0.17
6dFGS gJ025228.4-592243	7.33 ± 1.26	90.52 ± 2.67	40.68 ± 1.46	5.05 ± 1.33	1.0 ± 0.32
6dFGS gJ030735.3-725003	0.52 ± 0.04	8.82 ± 0.17	2.02 ± 0.09	2.07 ± 0.56	0.17 ± 0.05
6dFGS gJ031558.9-290126	39.96 ± 6.71	980.02 ± 13.98	128.36 ± 11.15	19.18 ± 5.1	1.44 ± 0.45
6dFGS gJ034713.9-132547	11.72 ± 1.94	205.47 ± 3.43	57.35 ± 2.17	7.34 ± 1.92	1.1 ± 0.34
6dFGS gJ035056.7-102559	4.75 ± 0.99	92.73 ± 2.62	27.31 ± 1.82	8.17 ± 2.21	0.4 ± 0.14
6dFGS gJ035107.6-052637	3.3 ± 0.22	21.63 ± 0.49	6.58 ± 0.31	3.39 ± 0.85	0.67 ± 0.17
6dFGS gJ035432.8-134008	8.86 ± 0.59	53.07 ± 0.99	11.15 ± 0.59	9.75 ± 2.42	0.63 ± 0.16
6dFGS gJ040024.4-250044	8.7 ± 0.41	27.48 ± 0.97	6.95 ± 0.82	4.69 ± 1.16	1.28 ± 0.32
6dFGS gJ041307.1-005017	0.61 ± 0.09	8.85 ± 0.35	3.85 ± 0.22	2.87 ± 0.79	0.15 ± 0.05
6dFGS gJ042020.4-355100	14.9 ± 1.98	234.06 ± 4.71	14.09 ± 2.97	7.51 ± 1.92	1.37 ± 0.4
6dFGS gJ042021.7-053054	13.24 ± 2.44	211.29 ± 5.09	39.9 ± 3.57	5.52 ± 1.46	1.66 ± 0.54
6dFGS gJ042256.6-185442	3.96 ± 0.27	18.65 ± 0.66	25.34 ± 0.49	3.71 ± 0.93	0.74 ± 0.19
6dFGS gJ043526.5-164346	5.69 ± 0.64	89.25 ± 1.16	27.45 ± 0.63	5.93 ± 1.5	0.66 ± 0.18
6dFGS gJ043622.3-102234	8.71 ± 0.33	115.11 ± 0.67	78.98 ± 0.41	8.01 ± 1.97	0.75 ± 0.19
6dFGS gJ043659.1-301042	3.14 ± 0.68	13.49 ± 1.21	12.31 ± 0.83	29.7 ± 8.15	0.07 ± 0.03
6dFGS gJ044040.4-411044	1.71 ± 0.1	23.13 ± 0.26	14.57 ± 0.22	1.49 ± 0.38	0.79 ± 0.21
6dFGS gJ044720.7-050814	4.01 ± 0.34	54.45 ± 1.14	18.29 ± 0.74	4.25 ± 1.07	0.65 ± 0.17
6dFGS gJ044739.0-040330	15.28 ± 1.17	121.0 ± 3.59	11.75 ± 1.91	7.04 ± 1.76	1.5 ± 0.39
6dFGS gJ045230.1-295335	16.92 ± 2.0	145.05 ± 3.49	74.44 ± 2.05	9.42 ± 2.39	1.24 ± 0.35
6dFGS gJ045557.5-145641	17.19 ± 1.54	235.82 ± 2.56	46.96 ± 1.81	10.49 ± 2.63	1.13 ± 0.3
6dFGS gJ050744.0-465231	3.19 ± 0.36	23.76 ± 0.64	32.68 ± 0.44	2.97 ± 0.76	0.74 ± 0.21
6dFGS gJ052210.1-422255	20.54 ± 3.12	137.63 ± 6.69	92.88 ± 5.03	24.37 ± 6.33	0.58 ± 0.18
6dFGS gJ052349.5-330551	8.34 ± 1.4	228.86 ± 3.04	54.12 ± 2.06	5.45 ± 1.42	1.06 ± 0.33
6dFGS gJ053724.5-381759	19.55 ± 4.59	370.24 ± 9.51	130.26 ± 6.87	9.61 ± 2.66	1.41 ± 0.51
6dFGS gJ054158.0-373837	19.37 ± 1.89	230.25 ± 3.52	57.94 ± 2.92	12.79 ± 3.23	1.05 ± 0.28
6dFGS gJ054914.9-242552	2.13 ± 0.13	14.12 ± 0.5	15.38 ± 0.31	3.8 ± 0.96	0.39 ± 0.1
6dFGS gJ055426.4-345341	5.22 ± 0.49	56.79 ± 1.21	18.32 ± 0.63	2.28 ± 0.57	1.58 ± 0.43
6dFGS gJ060917.5-560658	0.94 ± 0.08	10.75 ± 0.2	9.4 ± 0.13	1.48 ± 0.39	0.44 ± 0.12
6dFGS gJ061549.6-582605	0.52 ± 0.15	16.79 ± 0.3	3.04 ± 0.21	1.08 ± 0.33	0.33 ± 0.14
6dFGS gJ062233.5-231742	2.43 ± 0.12	19.7 ± 0.34	6.34 ± 0.23	2.96 ± 0.75	0.57 ± 0.15
6dFGS gJ063940.8-512515	6.66 ± 0.72	105.2 ± 1.18	49.0 ± 0.8	5.37 ± 1.36	0.86 ± 0.24
6dFGS gJ064157.7-431742	2.01 ± 0.16	19.16 ± 0.34	8.76 ± 0.26	2.97 ± 0.76	0.47 ± 0.13
6dFGS gJ065017.5-380514	1.08 ± 0.06	10.3 ± 0.14	1.76 ± 0.1	1.87 ± 0.49	0.4 ± 0.11
6dFGS gJ065654.3-631536	1.18 ± 0.09	7.79 ± 0.2	2.58 ± 0.13	2.69 ± 0.7	0.3 ± 0.08
6dFGS gJ070841.5-493306	7.27 ± 0.26	47.8 ± 0.59	4.88 ± 0.43	4.6 ± 1.14	1.09 ± 0.27
6dFGS gJ071033.0-535752	3.01 ± 0.18	21.14 ± 0.53	22.75 ± 0.44	5.35 ± 1.34	0.39 ± 0.1
6dFGS gJ082003.1-174151	1.27 ± 0.22	18.79 ± 0.5	4.13 ± 0.26	2.73 ± 0.74	0.32 ± 0.1
6dFGS gJ084219.1-034931	86.68 ± 10.5	1679.12 ± 22.62	977.92 ± 14.32	26.87 ± 7.12	2.23 ± 0.65

Table 3.4: continued.

Name	L(5100Å)	L(Hβ)	L([O III])	M_{BH}	ϵ_{Edd}
-	(10^{43} erg s^{-1})	(10^{40} erg s^{-1})	(10^{40} erg s^{-1})	(10^6 $M_\odot$)	-
6dFGS gJ084235.0-704249	6.45 ± 0.85	37.85 ± 1.85	17.32 ± 1.12	8.85 ± 2.26	0.5 ± 0.15
6dFGS gJ084510.2-073205	5.63 ± 0.74	70.4 ± 1.12	19.71 ± 0.94	5.11 ± 1.31	0.76 ± 0.22
6dFGS gJ084628.7-121409	6.03 ± 0.68	51.38 ± 1.17	66.27 ± 0.87	5.65 ± 1.43	0.74 ± 0.2
6dFGS gJ084951.7-235125	12.37 ± 0.93	165.11 ± 1.95	69.07 ± 1.33	5.42 ± 1.35	1.58 ± 0.41
6dFGS gJ085028.0-031817	29.22 ± 2.34	534.33 ± 6.36	244.8 ± 4.22	14.87 ± 3.75	1.36 ± 0.36
6dFGS gJ095219.1-013644	2.39 ± 0.1	37.0 ± 0.21	48.0 ± 0.15	2.15 ± 0.54	0.77 ± 0.2
6dFGS gJ101134.8-452830	0.95 ± 0.14	7.93 ± 0.34	4.95 ± 0.21	2.61 ± 0.71	0.25 ± 0.08
6dFGS gJ101420.7-041841	11.37 ± 0.31	94.0 ± 1.46	25.28 ± 0.76	7.3 ± 1.8	1.08 ± 0.27
6dFGS gJ101503.2-165214	85.47 ± 20.83	3161.86 ± 32.81	584.97 ± 18.95	25.74 ± 7.41	2.3 ± 0.87
6dFGS gJ103214.1-160960	0.43 ± 0.19	9.62 ± 0.62	5.94 ± 0.35	1.98 ± 0.71	0.15 ± 0.09
6dFGS gJ103257.0-270730	4.7 ± 0.38	48.24 ± 0.76	39.62 ± 0.5	3.47 ± 0.87	0.94 ± 0.25
6dFGS gJ104203.0-380058	3.35 ± 0.4	90.92 ± 0.98	23.31 ± 0.6	2.72 ± 0.7	0.85 ± 0.24
6dFGS gJ104208.9-400032	49.27 ± 5.81	615.13 ± 11.82	217.99 ± 10.1	23.07 ± 5.99	1.48 ± 0.42
6dFGS gJ104448.7-182653	5.54 ± 0.66	130.92 ± 1.42	67.06 ± 1.04	3.1 ± 0.79	1.24 ± 0.35
6dFGS gJ104833.8-390238	2.51 ± 0.14	40.77 ± 0.45	22.3 ± 0.3	3.39 ± 0.85	0.51 ± 0.13
6dFGS gJ105719.5-080541	16.96 ± 1.91	131.65 ± 4.75	68.37 ± 2.88	7.62 ± 1.93	1.54 ± 0.43
6dFGS gJ105727.9-403941	133.22 ± 12.33	1674.03 ± 22.73	163.4 ± 11.5	37.47 ± 9.98	2.46 ± 0.69
6dFGS gJ114353.8-361518	4.58 ± 0.64	40.24 ± 1.25	7.42 ± 0.81	4.68 ± 1.21	0.68 ± 0.2
6dFGS gJ114738.9-214508	24.01 ± 2.42	190.03 ± 4.33	80.87 ± 2.84	9.74 ± 2.47	1.71 ± 0.47
6dFGS gJ120624.2-243548	13.87 ± 0.99	143.91 ± 1.94	43.11 ± 1.34	7.97 ± 1.98	1.2 ± 0.31
6dFGS gJ122417.5-181205	1.97 ± 0.24	14.2 ± 0.65	2.61 ± 0.38	2.31 ± 0.6	0.59 ± 0.17
6dFGS gJ122527.2-041857	10.41 ± 1.13	328.06 ± 2.13	79.84 ± 1.65	7.95 ± 2.01	0.91 ± 0.25
6dFGS gJ123124.9-165350	9.56 ± 1.09	185.41 ± 2.29	43.36 ± 1.48	5.83 ± 1.48	1.14 ± 0.32
6dFGS gJ123817.2-344028	2.68 ± 0.19	5.42 ± 0.36	2.45 ± 0.23	1.12 ± 0.28	1.66 ± 0.44
6dFGS gJ125424.8-282632	2.74 ± 0.25	45.21 ± 0.47	18.69 ± 0.31	4.25 ± 1.08	0.45 ± 0.12
6dFGS gJ125706.4-443520	7.55 ± 0.71	41.38 ± 1.04	14.17 ± 0.74	4.41 ± 1.11	1.19 ± 0.32
6dFGS gJ125747.9-235044	21.97 ± 1.58	358.87 ± 3.0	221.08 ± 2.01	11.31 ± 2.83	1.35 ± 0.35
6dFGS gJ132158.2-310426	1.04 ± 0.15	9.88 ± 0.31	3.78 ± 0.22	2.37 ± 0.64	0.3 ± 0.09
6dFGS gJ132904.6-292556	24.27 ± 2.66	490.68 ± 4.29	235.67 ± 3.09	14.4 ± 3.66	1.17 ± 0.32
6dFGS gJ133739.6-090228	1.4 ± 0.25	11.29 ± 0.52	2.89 ± 0.27	1.92 ± 0.52	0.51 ± 0.16
6dFGS gJ134054.2-352111	19.6 ± 4.74	727.23 ± 11.0	142.3 ± 6.5	9.94 ± 2.77	1.36 ± 0.5
6dFGS gJ134524.7-025940	4.45 ± 0.49	50.42 ± 1.04	25.35 ± 0.56	4.78 ± 1.21	0.64 ± 0.18
6dFGS gJ135129.5-181347	0.22 ± 0.01	2.05 ± 0.04	0.91 ± 0.03	0.81 ± 0.23	0.19 ± 0.05
6dFGS gJ135439.5-421457	6.54 ± 0.73	257.97 ± 1.75	90.5 ± 1.06	5.98 ± 1.51	0.76 ± 0.21
6dFGS gJ140722.0-312058	1.65 ± 0.43	26.7 ± 1.11	11.33 ± 0.68	3.7 ± 1.07	0.31 ± 0.12
6dFGS gJ141048.7-364412	8.08 ± 0.29	62.51 ± 0.76	24.48 ± 0.48	6.0 ± 1.48	0.93 ± 0.23
6dFGS gJ142350.2-092318	1.72 ± 0.23	23.09 ± 0.72	11.45 ± 0.37	2.45 ± 0.64	0.49 ± 0.14
6dFGS gJ143438.4-425405	2.99 ± 0.52	62.56 ± 1.68	65.56 ± 1.21	3.47 ± 0.92	0.6 ± 0.19
6dFGS gJ144718.7-380222	2.45 ± 0.22	41.21 ± 0.53	22.6 ± 0.3	3.04 ± 0.77	0.56 ± 0.15
6dFGS gJ145712.7-131503	38.77 ± 5.5	509.99 ± 12.53	29.66 ± 6.28	11.35 ± 2.97	2.36 ± 0.7
6dFGS gJ150012.8-724840	10.84 ± 1.04	149.36 ± 1.95	14.43 ± 1.21	7.39 ± 1.85	1.02 ± 0.27
6dFGS gJ151159.8-211902	5.63 ± 0.3	79.56 ± 0.62	86.24 ± 0.4	4.24 ± 1.05	0.92 ± 0.23
6dFGS gJ151222.5-333334	0.46 ± 0.03	3.68 ± 0.09	2.2 ± 0.05	1.25 ± 0.34	0.26 ± 0.07
6dFGS gJ151515.2-782012	53.0 ± 3.72	1258.77 ± 9.12	762.98 ± 6.93	20.17 ± 5.15	1.82 ± 0.48
6dFGS gJ152228.7-064441	8.53 ± 0.65	171.47 ± 1.19	46.75 ± 0.81	4.58 ± 1.14	1.29 ± 0.34
6dFGS gJ153846.6-102628	44.84 ± 2.64	359.45 ± 4.25	71.54 ± 2.93	19.52 ± 4.94	1.59 ± 0.41
6dFGS gJ161519.1-093613	22.33 ± 1.06	386.75 ± 2.63	218.23 ± 1.9	8.64 ± 2.15	1.79 ± 0.45
6dFGS gJ161610.8-101406	5.13 ± 0.61	54.71 ± 1.32	15.31 ± 0.75	4.89 ± 1.25	0.73 ± 0.2

Table 3.4: continued.

Name	L(5100Å)	L(Hβ)	L([O III])	M_{BH}	ϵ_{Edd}
-	(10^{43} erg s^{-1})	(10^{40} erg s^{-1})	(10^{40} erg s^{-1})	(10^6 $M_\odot$)	-
6dFGS gJ162848.4-030408	10.11 ± 0.99	211.81 ± 2.25	28.14 ± 1.4	5.19 ± 1.3	1.35 ± 0.36
6dFGS gJ163626.8-211835	1.64 ± 0.23	27.53 ± 0.63	14.97 ± 0.44	2.8 ± 0.74	0.41 ± 0.12
6dFGS gJ163830.9-205525	4.14 ± 0.21	81.58 ± 0.93	35.03 ± 0.63	4.57 ± 1.14	0.63 ± 0.16
6dFGS gJ164610.4-112404	28.5 ± 1.35	148.89 ± 3.07	167.12 ± 2.0	11.81 ± 2.95	1.67 ± 0.42
6dFGS gJ172916.3-685442	2.82 ± 0.25	31.91 ± 0.97	10.4 ± 0.7	5.19 ± 1.32	0.38 ± 0.1
6dFGS gJ183450.8-572422	0.48 ± 0.2	8.18 ± 0.41	2.5 ± 0.22	3.02 ± 1.06	0.11 ± 0.06
6dFGS gJ184942.1-551310	1.53 ± 0.19	28.59 ± 0.41	1.79 ± 0.22	2.98 ± 0.78	0.36 ± 0.1
6dFGS gJ192631.1-191703	15.38 ± 0.88	65.76 ± 1.28	16.01 ± 0.73	9.52 ± 2.36	1.12 ± 0.28
6dFGS gJ193733.0-061305	1.04 ± 0.04	13.93 ± 0.12	16.0 ± 0.09	1.08 ± 0.28	0.67 ± 0.18
6dFGS gJ193819.6-432646	6.78 ± 0.41	158.39 ± 0.88	28.33 ± 0.56	4.45 ± 1.1	1.06 ± 0.27
6dFGS gJ194335.3-163108	2.32 ± 0.15	39.77 ± 0.25	7.0 ± 0.16	2.58 ± 0.65	0.62 ± 0.16
6dFGS gJ194909.3-103425	5.81 ± 0.17	30.62 ± 0.53	7.61 ± 0.28	7.66 ± 1.89	0.53 ± 0.13
6dFGS gJ195705.3-414117	45.57 ± 7.43	1028.56 ± 13.54	233.01 ± 10.26	18.6 ± 4.94	1.7 ± 0.53
6dFGS gJ200553.0-413442	5.29 ± 0.45	141.17 ± 1.04	54.82 ± 0.5	3.96 ± 0.99	0.92 ± 0.25
6dFGS gJ202104.4-223518	15.09 ± 1.91	145.8 ± 3.29	482.18 ± 2.42	4.48 ± 1.14	2.33 ± 0.66
6dFGS gJ202557.4-482226	5.21 ± 0.37	71.98 ± 0.64	31.39 ± 0.42	6.31 ± 1.57	0.57 ± 0.15
6dFGS gJ203927.2-301852	2.23 ± 0.3	29.44 ± 0.76	12.5 ± 0.48	2.97 ± 0.78	0.52 ± 0.15
6dFGS gJ204513.1-301027	5.9 ± 1.01	85.94 ± 2.71	21.36 ± 1.12	4.47 ± 1.17	0.91 ± 0.29
6dFGS gJ205920.7-314735	4.26 ± 0.44	73.24 ± 1.06	81.61 ± 0.61	1.64 ± 0.42	1.79 ± 0.49
6dFGS gJ205933.0-513601	12.36 ± 3.64	269.56 ± 7.35	87.29 ± 5.29	12.45 ± 3.63	0.69 ± 0.28
6dFGS gJ211224.6-412854	31.97 ± 4.42	394.07 ± 10.53	58.68 ± 7.31	12.5 ± 3.25	1.77 ± 0.52
6dFGS gJ211524.9-141706	43.19 ± 4.79	529.3 ± 11.21	101.11 ± 7.1	20.24 ± 5.22	1.48 ± 0.41
6dFGS gJ213333.4-355848	21.62 ± 6.43	494.89 ± 9.5	90.99 ± 7.41	12.57 ± 3.69	1.19 ± 0.5
6dFGS gJ213529.5-623007	2.99 ± 0.22	45.61 ± 0.6	11.64 ± 0.45	3.06 ± 0.77	0.68 ± 0.18
6dFGS gJ213632.0-011626	16.76 ± 2.8	287.19 ± 6.25	61.93 ± 4.72	12.2 ± 3.19	0.95 ± 0.3
6dFGS gJ213748.0-111204	2.35 ± 0.38	49.34 ± 1.12	15.66 ± 0.76	3.24 ± 0.86	0.5 ± 0.16
6dFGS gJ214306.1-295817	15.2 ± 1.27	181.05 ± 2.29	14.63 ± 2.01	12.03 ± 3.01	0.87 ± 0.23
6dFGS gJ214505.8-692231	2.3 ± 0.81	61.38 ± 1.52	21.45 ± 1.01	2.8 ± 0.88	0.57 ± 0.27
6dFGS gJ215526.7-121032	1.14 ± 0.31	25.18 ± 0.74	5.13 ± 0.36	3.18 ± 0.94	0.25 ± 0.1
6dFGS gJ215723.2-312307	1.71 ± 0.26	27.46 ± 0.55	7.23 ± 0.34	4.23 ± 1.12	0.28 ± 0.08
6dFGS gJ220755.6-282406	5.18 ± 0.53	91.73 ± 1.78	14.2 ± 0.89	5.47 ± 1.38	0.66 ± 0.18
6dFGS gJ221611.2-394734	16.27 ± 2.31	303.87 ± 4.79	8.84 ± 3.0	11.63 ± 2.99	0.97 ± 0.29
6dFGS gJ221653.2-445157	22.56 ± 1.62	279.47 ± 2.23	69.84 ± 1.5	13.67 ± 3.42	1.14 ± 0.3
6dFGS gJ221800.2-395723	12.57 ± 2.5	249.54 ± 5.03	62.04 ± 3.36	13.94 ± 3.73	0.62 ± 0.21
6dFGS gJ222903.5-140106	28.57 ± 2.05	391.13 ± 4.36	113.84 ± 3.18	14.64 ± 3.68	1.35 ± 0.35
6dFGS gJ224237.7-384516	9.81 ± 1.37	199.07 ± 2.32	57.43 ± 1.48	6.11 ± 1.57	1.11 ± 0.32
6dFGS gJ224458.2-182250	14.57 ± 1.66	199.1 ± 4.1	124.76 ± 2.81	10.14 ± 2.57	0.99 ± 0.28
6dFGS gJ224520.3-465211	131.38 ± 6.5	3117.23 ± 14.31	1414.39 ± 12.98	32.71 ± 8.6	2.78 ± 0.74
6dFGS gJ225014.1-115201	3.46 ± 0.48	73.88 ± 1.93	26.47 ± 1.23	3.47 ± 0.9	0.69 ± 0.2
6dFGS gJ225321.6-511802	2.35 ± 0.57	45.03 ± 1.26	5.38 ± 0.63	3.62 ± 1.02	0.45 ± 0.17
6dFGS gJ231103.4-202221	4.41 ± 1.03	48.63 ± 1.77	13.56 ± 1.16	3.07 ± 0.85	1.0 ± 0.36
6dFGS gJ234042.0-594132	14.76 ± 5.98	643.87 ± 11.72	290.43 ± 7.95	9.3 ± 3.04	1.1 ± 0.57
6dFGS gJ234120.6-592359	4.54 ± 1.42	88.65 ± 3.04	47.82 ± 2.39	8.38 ± 2.5	0.37 ± 0.16
6dFGS gJ234614.6-490952	15.7 ± 1.31	184.03 ± 2.95	97.22 ± 1.75	9.0 ± 2.25	1.21 ± 0.32
6dFGS gJ235808.5-102843	8.14 ± 0.87	72.08 ± 2.12	38.41 ± 1.53	11.23 ± 2.83	0.5 ± 0.14

Notes. Column (1) Name in the 6dFGS. (2) Luminosity at 5100 Å. (3) Luminosity of Hβ line. (4) Luminosity of [O III] line. (5) Mass of central black hole. (6) Eddington ratio.

Table 3.5: Flux densities and luminosities on radio and optical bands, radio-loudness, and radio type in the radio sample.

Name	S_{843MHz}	$S_{1.4GHz}$	S_{5GHz}	$S_{8.4GHz}$	S_{22GHz}	F (4400Å)	L (Radio)	L (4400Å)	R_L	R_L	R_L	Type
-	(mJy)	(mJy)	(mJy)	(mJy)	(mJy)	(10^{-17} erg s^{-1} cm^{-2} Å^{-1})	(10^{38} erg s^{-1})	(10^{43} erg s^{-1})	($\alpha = 0$)	($\alpha = 0.5$)	($\alpha = 1$)	-
6dFGS gJ012237.5-264646	-	3.8 ± 0.5	-	-	-	4.0 ± 1.97	332.24 ± 43.72	10.99 ± 5.42	147.1	77.9	41.2	RL
6dFGS gJ042256.6-185442	-	2.8 ± 0.5	-	-	-	78.9 ± 9.66	3.89 ± 0.69	3.44 ± 0.42	5.5	2.9	1.5	RQ
6dFGS gJ043622.3-102234	-	17.0 ± 0.7	-	-	-	869.95 ± 120.41	6.81 ± 0.28	10.95 ± 1.52	3.0	1.6	0.8	RQ
6dFGS gJ045230.1-295335	-	9.5 ± 0.5	-	-	-	16.29 ± 1.94	343.15 ± 18.06	18.49 ± 2.21	90.3	47.8	25.3	RL
6dFGS gJ054914.9-242552	-	2.4 ± 0.5	-	-	-	118.9 ± 12.51	1.6 ± 0.33	2.49 ± 0.26	3.1	1.7	0.9	RQ
6dFGS gJ062233.5-231742	-	4.3 ± 0.5	-	-	-	238.19 ± 26.21	2.0 ± 0.23	3.48 ± 0.38	2.8	1.5	0.8	RQ
6dFGS gJ084628.7-121409	-	15.3 ± 0.7	-	-	-	60.24 ± 6.78	63.74 ± 2.92	7.89 ± 0.89	39.3	20.8	11.0	RL
6dFGS gJ095219.1-013644	-	62.2 ± 1.9	-	-	-	634.94 ± 104.25	7.56 ± 0.23	2.43 ± 0.4	15.2	8.0	4.2	RQ
6dFGS gJ104208.9-400032	-	5.7 ± 0.5	-	-	-	18.75 ± 2.31	414.27 ± 36.34	42.83 ± 5.27	47.1	24.9	13.2	RL
6dFGS gJ105727.9-403941	437.5 ± 13.2	-	244 ± 11	164 ± 8	155 ± 7	74.16 ± 8.41	68120.14 ± 3070.99	182.2 ± 20.67	509.5	509.5	509.5	RL
6dFGS gJ114738.9-214508	-	5.7 ± 0.5	-	-	-	50.53 ± 5.15	112.51 ± 9.87	31.35 ± 3.19	17.5	9.2	4.9	RQ
6dFGS gJ143438.4-425405	10.5 ± 1.2	-	-	-	-	28.08 ± 6.09	30.08 ± 3.44	4.2 ± 0.91	57.9	23.8	9.8	RL
6dFGS gJ150012.8-724840	20.1 ± 1.5	-	-	-	-	67.45 ± 8.45	90.59 ± 6.76	15.87 ± 1.99	46.1	18.9	7.8	RL
6dFGS gJ151159.8-211902	-	46.9 ± 1.5	-	-	-	299.76 ± 37.46	30.44 ± 0.97	6.12 ± 0.76	24.2	12.8	6.8	RL
6dFGS gJ151222.5-333334	12.0 ± 1.6	9.0 ± 0.6	-	-	-	72.95 ± 10.91	1.59 ± 0.11	0.4 ± 0.06	19.1	10.1	5.3	RL
6dFGS gJ151515.2-782012	33.0 ± 1.8	-	-	-	-	80.71 ± 12.71	571.06 ± 31.15	72.9 ± 11.48	63.3	26.0	10.7	RL
6dFGS gJ152228.7-064441	-	14.6 ± 0.6	-	-	-	148.74 ± 27.95	34.99 ± 1.44	11.2 ± 2.11	15.2	8.0	4.3	RQ
6dFGS gJ163830.9-205525	-	6.8 ± 0.5	-	-	-	992.5 ± 150.57	1.57 ± 0.12	7.2 ± 1.09	1.1	0.6	0.3	RQ
6dFGS gJ164610.4-112404	-	38.3 ± 1.6	-	-	-	450.9 ± 31.46	71.9 ± 3.0	26.6 ± 1.86	13.2	7.0	3.7	RQ
6dFGS gJ193733.0-061305	-	42.2 ± 1.7	-	-	-	1253.46 ± 127.85	1.4 ± 0.06	1.31 ± 0.13	5.2	2.8	1.5	RQ
6dFGS gJ202104.4-223518	-	24.6 ± 0.9	-	-	-	43.99 ± 4.88	332.29 ± 12.16	18.68 ± 2.07	86.6	45.8	24.2	RL
6dFGS gJ203927.2-301852	-	5.8 ± 0.5	-	-	-	41.01 ± 6.41	12.51 ± 1.08	2.78 ± 0.43	21.9	11.6	6.1	RL
6dFGS gJ205920.7-314735	-	9.6 ± 0.6	-	-	-	112.76 ± 15.45	17.69 ± 1.11	6.53 ± 0.9	13.2	7.0	3.7	RQ

Notes. Column (1) Name in the 6dFGS. (2) Flux density detected by the SUMSS at 843 MHz. (3) Flux density detected by the NVSS at 1.4 GHz. Columns (4, 5, 6) Flux densities detected by the AT20G at 5 GHz, 8.4 GHz, and 22 GHz respectively. (7) Optical flux density on B-band. (8) Radio luminosity at 5 GHz. (9) Optical luminosity on B-band. Columns (10, 11, 12) Radio-loudness assuming a spectral index of α=0, α=0.5, and α=1 respectively. (13) Radio type according to the R_L (α=0.5).

Table 3.7: The *Swift* XRT observational details and spectral fitting results of the radio sample.

Name	Count rate	Exp. time	n_H	Γ	$F_{0.3-10.0\,keV}$	$L_{0.3-10.0\,keV}$	Stat.	Val./d.o.f.
-	(10^{-2} cts s^{-1})	(sec)	(10^{20} cm^{-2})	-	(10^{-12} ergs cm^{-2} s^{-1})	(10^{43} ergs s^{-1})	-	-
6dFGS gJ012237.5-264646	2.99	2308	1.21	2.52 ± 0.4	0.80	56.13	C	36.13/44
6dFGS gJ042256.6-185442	0.19	13020	3.18	0.74 ± 0.5	0.20	0.18	C	44.62/20
6dFGS gJ084628.7-121409	17.73	3943	6.04	2.81 ± 0.3	6.09	18.52	χ^2	25.82/27
6dFGS gJ104208.9-400032	1.04	15810	6.67	2.61 ± 0.3	0.39	20.34	χ^2	3.10/5
6dFGS gJ114738.9-214508	0.19	7827	3.69	0.90 ± 0.8	0.12	1.33	C	13.68/9
6dFGS gJ143438.4-425405	7.65	5309	5.38	1.74 ± 0.3	3.07	10.04	χ^2	13.72/15
6dFGS gJ150012.8-724840	3.87	8626	10.01	1.83 ± 0.3	1.56	7.88	χ^2	9.03/12
6dFGS gJ151222.5-333334	0.16	7347	12.60	1.08 ± 0.9	0.11	0.01	C	10.24/8
6dFGS gJ151515.2-782012	4.46	3878	7.09	1.87 ± 0.3	1.63	30.97	χ^2	5.70/5
6dFGS gJ152228.7-064441	19.86	3681	5.89	2.59 ± 0.1	6.70	11.50	χ^2	19.08/29
6dFGS gJ164610.4-112404	31.90	5549	10.22	1.59 ± 0.1	15.55	19.99	χ^2	91.79/73
6dFGS gJ205920.7-314735	8.28	6548	9.38	2.31 ± 0.3	2.71	3.49	χ^2	13.35/21

Notes. Column (1) Name in the 6dFGS. (2) Count rate. (3) Exposure time. (4) Column density. (5) Photon index. (6) Flux in 0.3-10.0 keV energy range. (7) Luminosity in 0.3-10.0 keV energy range. (8) χ^2: Chi-squared statistics, C: Cash statistics. (9) Value / degrees of freedom.

Chapter 4

Searching for γ-ray NLS1s in the 6dFGS catalog

The first γ-ray NLS1 PMN J0948+0022 ($z = 0.585$) was detected by the *Fermi* LAT in 2009 (Abdo et al., 2009a). A multi-wavelength campaign was immediately carried out to monitor this object, which confirmed that the γ-ray emission was indeed associated with the NLS1 and its multi-wavelength behavior was typical of a source harboring a beamed relativistic jet, like Blazars (Abdo et al., 2009b). At that time, this object was an exception, as relativistic jets are usually launched in powerful Blazars instead of Seyfert galaxies. In 2010, PMN J0948+0022 underwent a strong γ-ray outburst reaching an energy of $\sim 10^{48}$ erg s^{-1} in 0.1-100 GeV compared to that of FSRQ (Foschini et al., 2011). In addition, other γ-ray NLS1s were discovered later (Abdo et al., 2009c; Yao et al., 2015; Liao et al., 2015; D'Ammando et al., 2015, 2016; Paliya & Stalin, 2016; Berton et al., 2017; Paliya et al., 2018; Lähteenmäki et al., 2018; Yao et al., 2019). A full list of γ-ray NLS1s can be seen in Romano et al. (2018). This confirmed that NLS1s are a new class of AGN emitting γ-ray from relativistic jets. However, γ-ray NLS1s are rare, only 20 sources are identified by the *Fermi* LAT until now. It is of great importance to find new γ-ray NLS1s, since they are ideal laboratories in revealing the formation and evolution of relativistic jets and understanding their parent population in the AGN family. With the aim of identifying more γ-ray NLS1s, I take advantage of the new NLS1 sample in the 6dFGS, which includes 167 NLS1s in the southern hemisphere and 23 of them having a radio detection.

4.1 Data analysis

The *Fermi* LAT is a pair-conversion telescope operated in all-sky survey from below 20 MeV to above 300 GeV. It has collected more than 10 years data released to the public through the LAT data archive at the Fermi Science Support Center (FSSC) [1]. The FSSC also supports a suite of public software tools, the *ScienceTools* [2], for reduction and analysis of the LAT data. I cross-matched the optical position of all NLS1s in the 6dFGS sample with the LAT 8-year Point Source Catalog (4FGL) (The Fermi-LAT collaboration, 2019) [3] within a search radius of 10 arcmin. Since more than 90% of the sources in the 4FGL have a statistical source localization error less than 10 arcmin. Unfortunately, no object was found to be detected in γ-ray.

In order to confirm if there is an additional source nearby the optical location, I generated a test statistic (TS) map for each radio-detected NLS1, since γ-ray NLS1s are very likely to be radio emitters. The TS is defined as

$$TS = -2\ln(L_{max,0}/L_{max,1}), \tag{4.1}$$

where $L_{max,0}$ is the maximum likelihood value for a model without an additional source and $L_{max,1}$ is the maximum likelihood value for a model with the additional source at a specified location. The software I used is the *Fermipy* [4], which is an open-source python framework that facilitates analysis of data collected by the *Fermi* LAT (Wood et al., 2017). *Fermipy* is built on the *ScienceTools* and a suite of softwares for the LAT mission. It provides a high-level interface for the LAT data analysis. *Fermipy* also relies on a number of scientific python libraries including *Numpy*, *Scipy*, *Matplotlib*, and *Astropy*. It currently supports a number of high-level analysis methods for extracting spectral energy distributions and lightcurves, generating TS maps, finding new source candidates, and fitting source position and extension.

The analysis is started by composing a configuration file that defines different parameters to initialize the analysis object. The data set was collected from 2008/09 to 2018/09 in the energy range of 0.1-500 GeV. I analyzed a region-of-interest (ROI) of 15 degree radius centered at the optical position with a spatial bin size of 0.1 degree. I also defined the galactic diffuse emission model for a likelihood analysis and the isotropic model for a point

[1] https://fermi.gsfc.nasa.gov/ssc/.
[2] https://fermi.gsfc.nasa.gov/ssc/data/analysis/.
[3] https://fermi.gsfc.nasa.gov/ssc/data/access/lat/8yr_catalog/.
[4] https://fermipy.readthedocs.io/en/latest/.

source analysis. The other parameters are set as default. This analysis is executed by creating an instance of *GTAnalysis* with the configuration file as its argument and calling its analysis methods to perform different analysis tasks. The *setup* method is called to run the data and model preparation by executing the appropriate gt-tools in the binned likelihood analysis of *ScienceTools* [5]: *gtselect* (data selection), *gtmktime* (data filtering), *gtbin* (data binning), *gtltcube* (livetime calculation), *gtexpcube2* (exposure calculation), and *gtsrcmaps* (calculation of spatial templates for individual model components).

Once the analysis object is initialized, the *optimize* method is used to find best-fit values of the spectral parameters for all components of the model. This typically involves optimizing the parameters of the background model, generating a TS or residual map of the region to assess the quality of the model, and extracting the characteristics (flux, TS, spectral fit parameters, SED, etc.) of a source of interest. By default, all parameters of the model are initially fixed. I freed the normalization of catalog sources within 5 degree of the ROI center and freed the galactic and isotropic components. After freeing parameters of the model, I called the *fit* method to execute a global spectral fit over the entire energy range of the analysis. This will fit the sources using a power-law model with a photon index of $\Gamma_\gamma = 2$ and maximize the likelihood with respect to the model parameters.

Once the model is optimized, I called the *tsmap* method to look for new sources, which is similar to the *gttsmap* of *ScienceTools*. This method generates a TS map for an additional source centered at each spatial bin in the ROI using a point source power-law model with $\Gamma_\gamma = 2$ and calculates the maximum likelihood TS value for each spatial bin. If a new source candidate is identified in the vicinity of the optical location, a bright peak will appear in the center of the TS map. The TS maps of 23 radio-detected NLS1s are shown in Fig. 4.1. It is noted that no additional source is around the optical position. Therefore, no γ-ray NLS1 seems to be present in the radio-detected subsample. However, I can not rule out that γ-ray sources might be among the radio-silent subsample, or fast γ-ray flares from one or more of the sources are present.

4.2 Results

In this work, I tried to search for γ-ray NLS1s in the 6dFGS catalog. The results are summarized as follows.

[5] https://fermi.gsfc.nasa.gov/ssc/data/analysis/scitools/binned_likelihood_tutorial.html.

1. I cross-matched the optical position of all NLS1s with the 4FGL within a search radius of 10 arcmin finding no γ-ray source detected.

2. I further analyzed the *Fermi* 10 years data set for 23 radio-detected NLS1s. I generated their TS maps to confirm if there is an additional source nearby the optical location using the *Fermipy*, finding that no γ-ray NLS1 seems to be present in the radio-detected subsample.

However, I can not rule out that γ-ray sources might be present in the radio-silent subsample. A dedicated analysis will be carried out in the future.

Figure 4.1: The TS maps of 23 radio-detected NLS1s. The green circles center on the optical position with a radius of 0.5 degree.

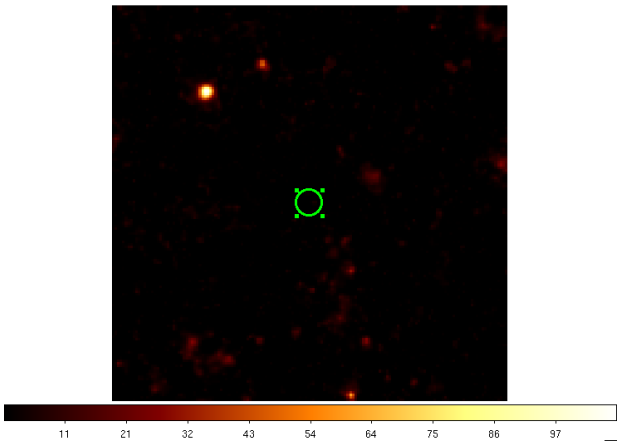

(a) 6dFGS gJ012237.5-264646

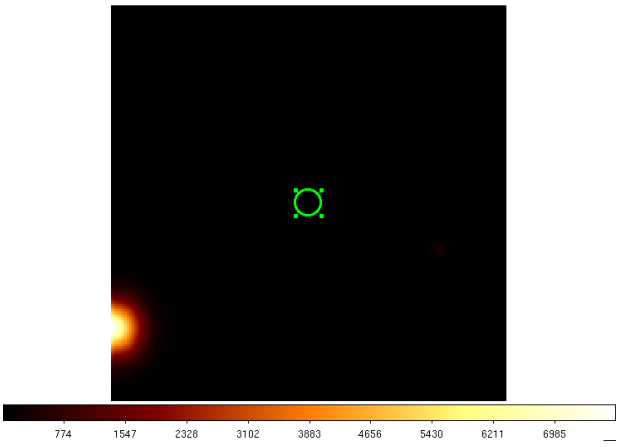

(b) 6dFGS gJ042256.6-185442

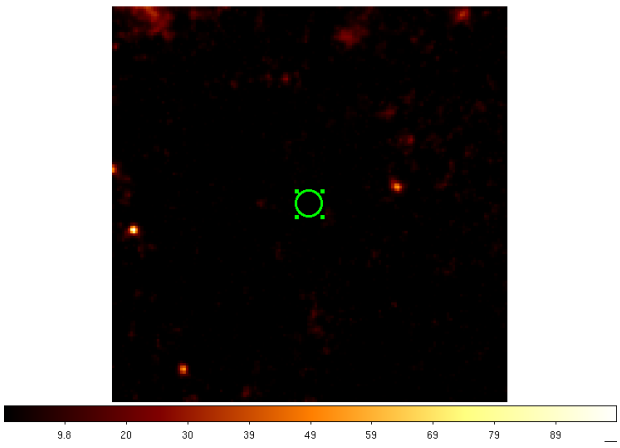

(c) 6dFGS gJ043622.3-102234

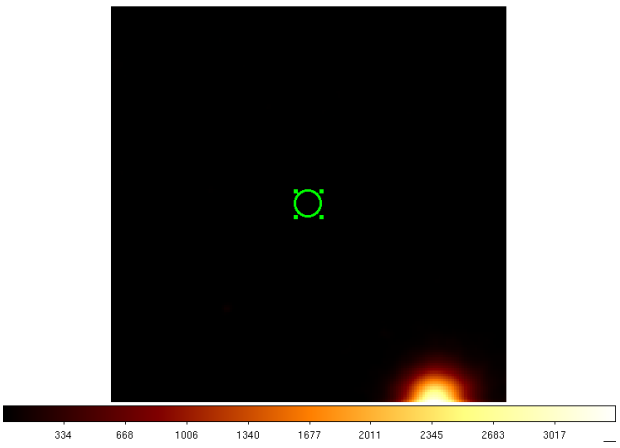

(d) 6dFGS gJ045230.1-295335

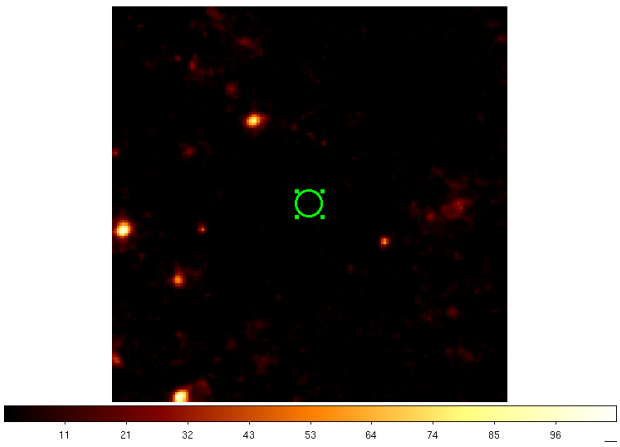

(e) 6dFGS gJ054914.9-242552

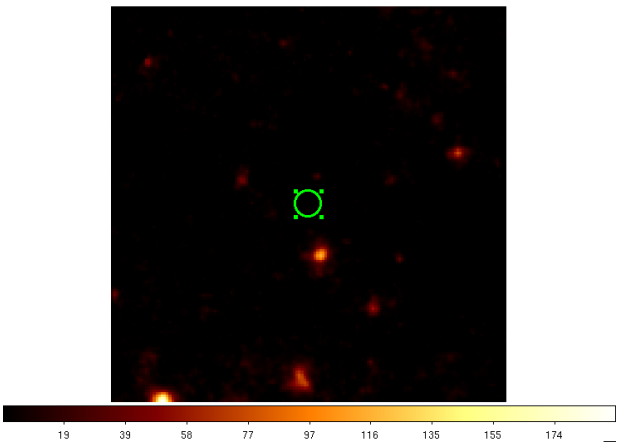

(f) 6dFGS gJ062233.5-231742

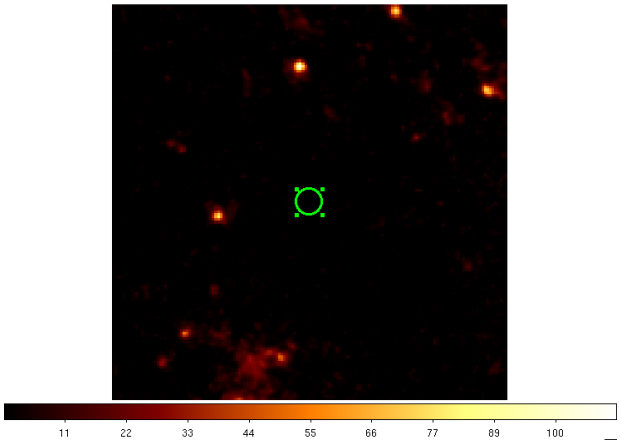

(g) 6dFGS gJ084628.7-121409

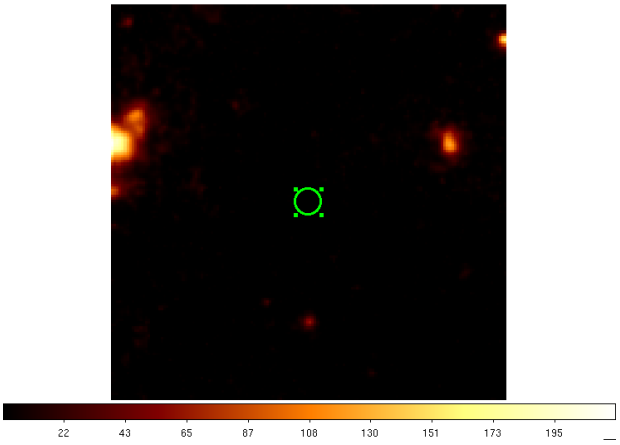

(h) 6dFGS gJ095219.1-013644

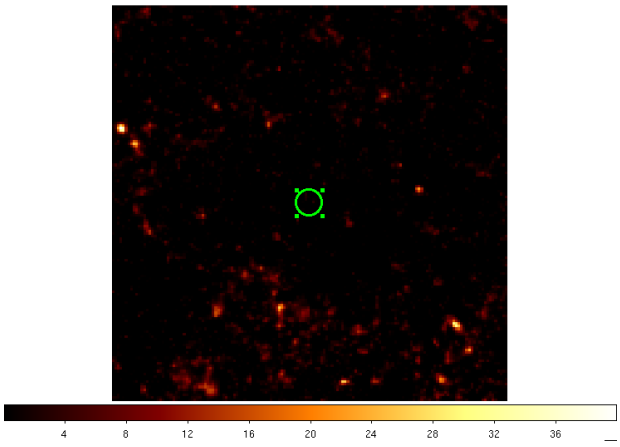

(i) 6dFGS gJ104208.9-400032

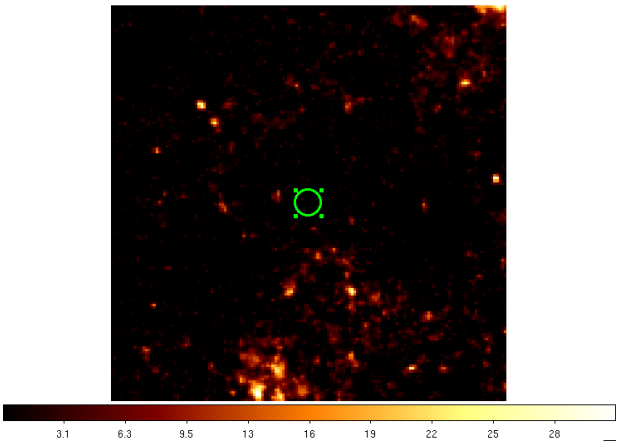

(j) 6dFGS gJ105727.9-403941

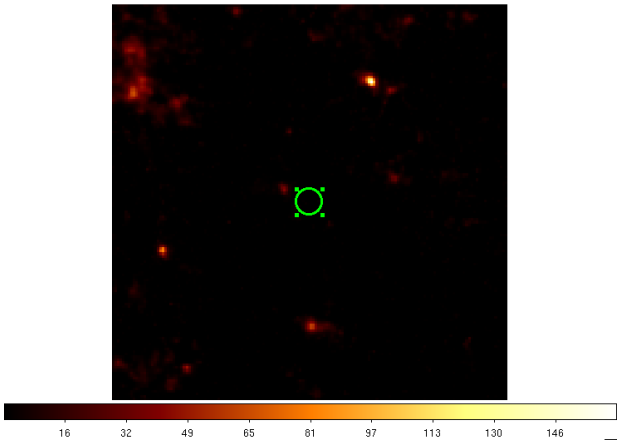

(k) 6dFGS gJ114738.9-214508

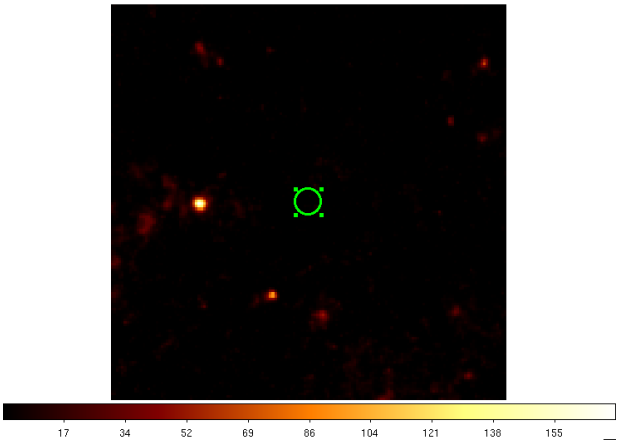

(l) 6dFGS gJ143438.4-425405

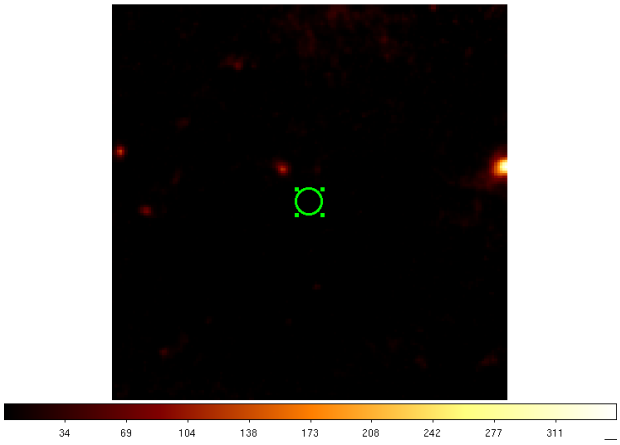

(m) 6dFGS gJ150012.8-724840

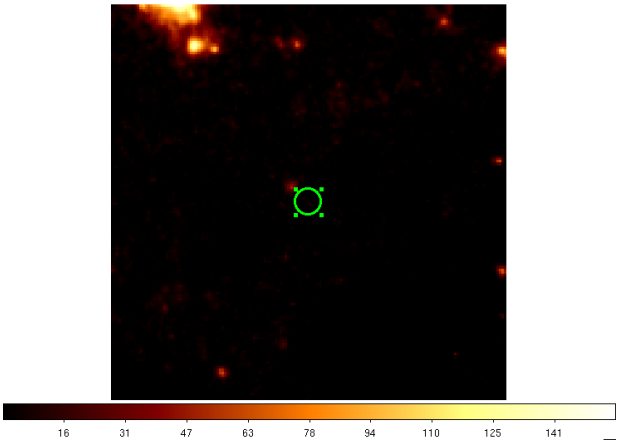

(n) 6dFGS gJ151159.8-211902

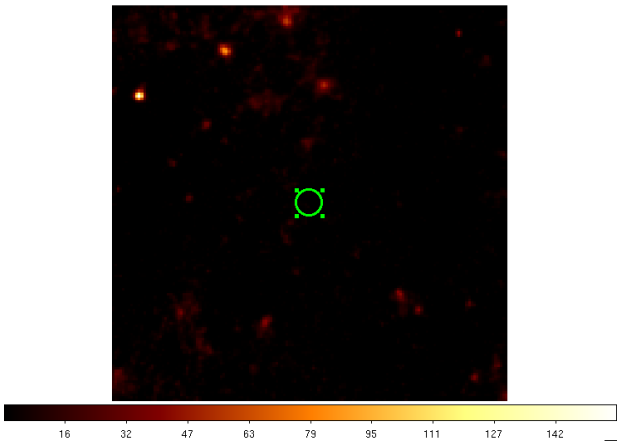

(o) 6dFGS gJ151222.5-333334

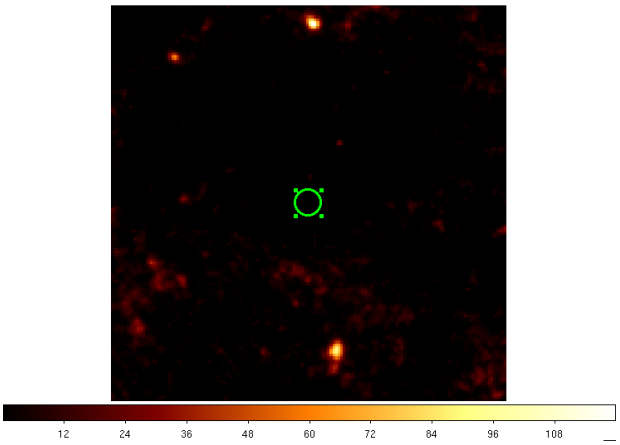

(p) 6dFGS gJ151515.2-782012

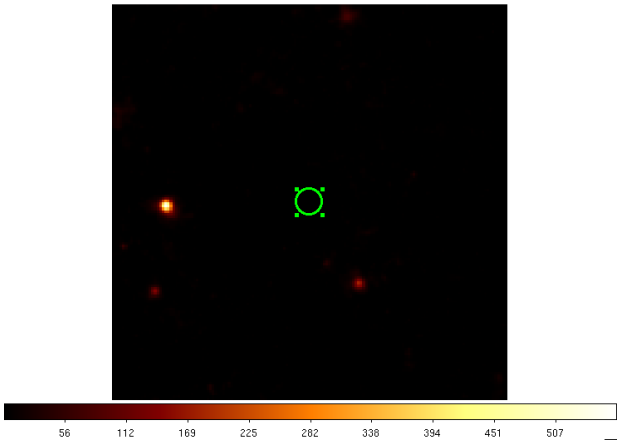

(q) 6dFGS gJ152228.7-064441

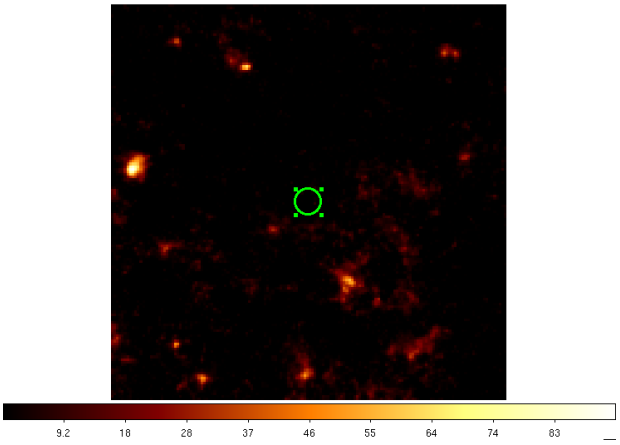

(r) 6dFGS gJ163830.9-205525

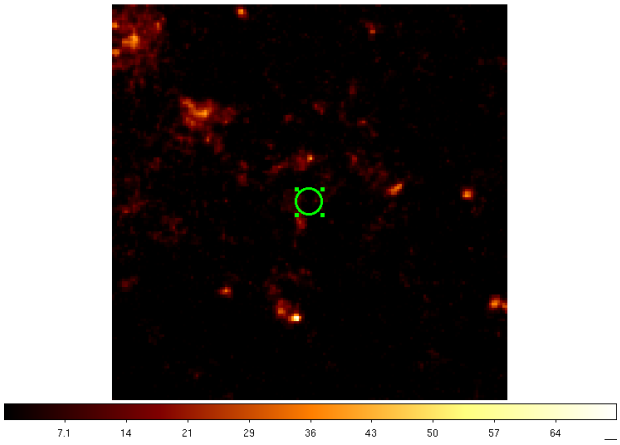

(s) 6dFGS gJ164610.4-112404

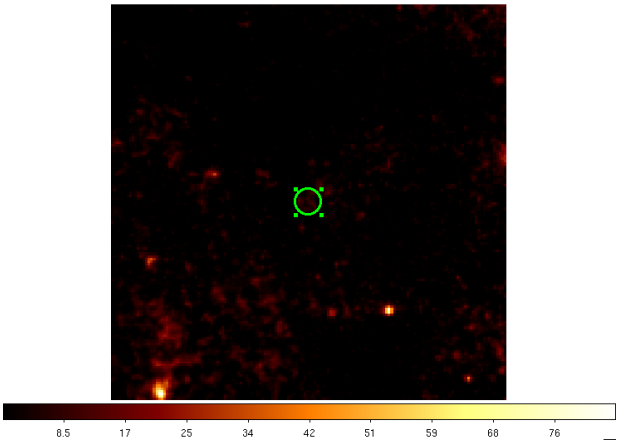

(t) 6dFGS gJ193733.0-061305

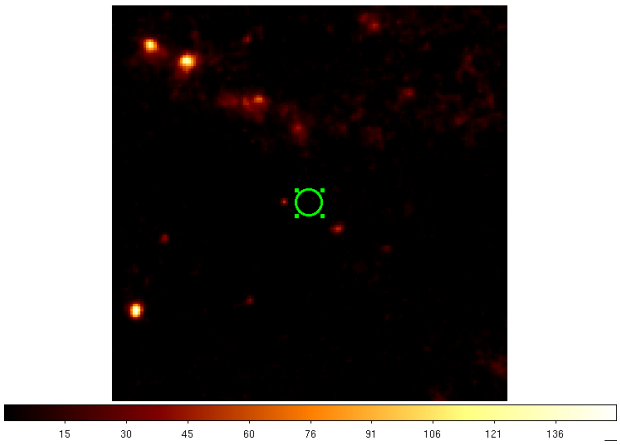

(u) 6dFGS gJ202104.4-223518

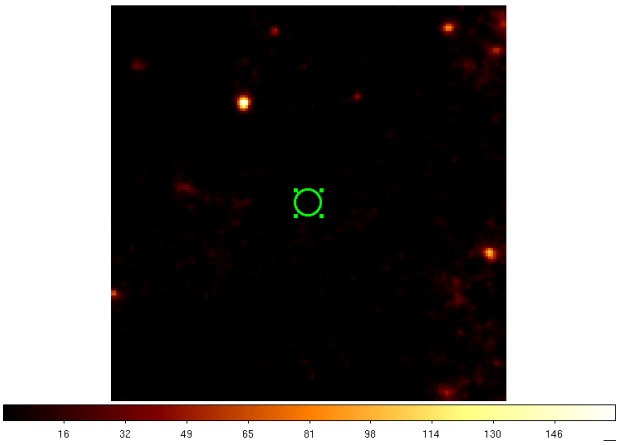

(v) 6dFGS gJ203927.2-301852

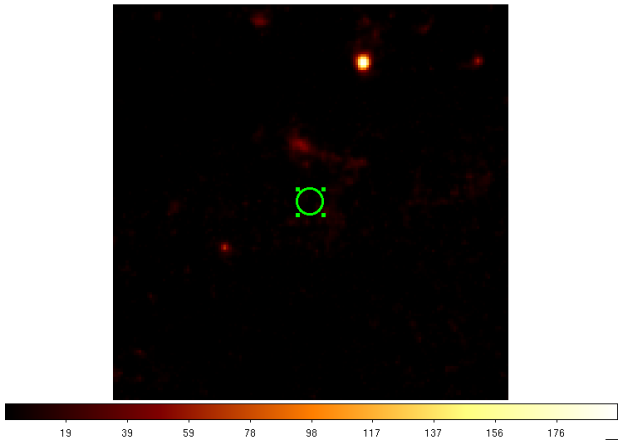

(w) 6dFGS gJ205920.7-314735

Chapter 5

X-ray spectral complexity of NLS1s in the 6dFGS catalog

5.1 Sample selection

Understanding the X-ray spectral properties of NLS1s and the difference between simple and complex NLS1s would be a breakthrough for revealing the X-ray emission mechanism of this peculiar class of AGN. From the previous *Swift* observations, it is evident that the XRT spectra do not have a S/N good enough to detect the complex features in X-ray band. Thus in the following, I decided to focus only on the *XMM-Newton* data, which have a significantly better resolution and sensitivity to study this peculiar feature of NLS1s.

In this work, I selected sources both having optical spectroscopic observations and X-ray observations by the *XMM-Newton* with published data on the *XMM-Newton* Science Archive (XSA). I firstly searched the 6dFGS NLS1 sample (Chen et al., 2018b) in the XSA and selected objects having an EPIC [1] pointed observation within a search radius of 10 arcmin. I excluded some sources with a total counts of PN camera less than 3000. Because if the X-ray spectrum does not have many counts, the complex features will probably not be displayed, this will lead to a misclassification of the source as a simple one. Additionally, I selected sources having an optical spectroscopic observation. In total, there are 11 NLS1s used in this work. I try to link the properties between the optical and X-ray spectroscopy, to better study the nature of NLS1s.

[1] The European Photon Imaging Camera.

5.2 Data reduction

5.2.1 Optical data reduction

I collected the optical spectra for these 11 NLS1s. Nine objects have new observations by the IMACS instrument of the 6.5-meter Walter Baade telescope and the WFCCD instrument of the 2.5-meter Du Pont telescope at the Las Campanas Observatory (LCO) in Chile. I performed a standard spectroscopic reduction using IRAF, with bias and flat-field correction, followed by wavelength, flux calibration, and sky subtraction. Standard stars EG21, LTT2415, and LTT7987 were used for the flux calibration. The spectra of two more objects were obtained from the archive of the 2.54-meter Isaac Newton telescope in La Palma (Spain) and the 1.22-meter Galileo telescope in Asiago (Italy). All these spectra were corrected for galactic extinction using the A_V extinction coefficients (Landolt V) (Schlafly & Finkbeiner, 2011) extracted from the NASA/IPAC Extragalactic Database (NED). For the redshift correction, I used the low ionization forbidden lines, such as [O I] λ6300, [S II] $\lambda\lambda$6716,6731, and [O II] λ3727 as reference (Komossa et al., 2008; Berton et al., 2016). If these lines were not visible, I brought the optical spectra to the rest frame according to the redshift in the NED. The spectroscopic observation details are listed in Table 5.1.

Table 5.1: The spectroscopic observation details of the 11 NLS1s.

6dFGS name	Short name	Telescope	Observed date	Exp. time
-	-	-	(yyyy-mm)	(s)
6dF J0228152-405715	J0228	Du Pont	2019-02	3 × 900
6dF J0230055-085953	J0230	Isaac Newton	1996-08	2 × 900
6dF J0436223-102234	J0436	Galileo	2017-11	4 × 1200
6dF J0452301-295335	J0452	Du Pont	2019-02	3 × 900
6dF J0708415-493306	J0708	Walter Baade	2019-01	3 × 900
6dF J1325194-382453	J1325	Walter Baade	2019-01	1 × 600
6dF J1511598-211902	J1511	Du Pont	2018-07	3 × 900
6dF J1638309-205525	J1638	Du Pont	2018-07	3 × 600
6dF J1937330-061305	J1937	Du Pont	2018-07	3 × 900
6dF J2135295-623007	J2135	Du Pont	2018-07	3 × 900
6dF J2245203-465211	J2245	Du Pont	2018-07	3 × 900

5.2.2 X-ray data reduction

The observation data files (ODFs) of these 11 NLS1s were processed with the *XMM-Newton* Science Analysis System (SAS) [2] version 16.1.0 with the latest current calibration files [3]. The PN camera was operated in full-frame mode, and the two MOS cameras were in large-window mode. I followed the standard prescriptions of the PN and MOS spectral extraction from point-like sources [4]. Spectra were extracted from the PN+MOS1+MOS2 CCDs. I filtered event lists for flaring particle background, and chose time intervals with low and steady background during the observations. Source photons were extracted in a circle with a radius of 30 arcsec centered on the source from the PN+MOS1+MOS2 images, and background was selected from a source-free region with a radius of 60 arcsec. For each source, ancillary response (arf) and redistribution matrix (rmf) files were created. Spectra were then rebinned to have at least 25 counts per bin. The *XMM-Newton* observation details of these 11 NLS1s are listed in Table 5.2.

5.3 Spectral analysis

5.3.1 Optical spectra

The new optical spectra of the 11 NLS1s have a higher signal-to-noise (S/N) ratio than those from the 6dFGS, thus allowed us to analyze their emission line profiles in detail. I subtracted the continuum and the Fe II multiplets from the observed spectra. The Fe II templates were reproduced using the procedure described in Kovačević et al. (2010); Shapovalova et al. (2012). An example of Fe II subtraction is shown in Fig. 5.1. After these subtractions, I fitted the [O III] $\lambda\lambda$4959,5007 double lines with two Gaussian (one narrow and one broad) components and corrected for the instrumental resolution. An example of the [O III] lines fitting is displayed in Fig. 5.2. The narrow and broad Gaussian components are associated with the line core and the blue wing, respectively.

I measured the velocity of the blue wing using the central wavelength of narrow component which represents the line core, minus that of broad component which represents the blue wing, as listed in Table 5.3. Although the fitting procedure has been carried out on both [O III] lines, I measured the velocity of the blue wing only for [O III] λ5007. The

[2]https://www.cosmos.esa.int/web/xmm-newton/sas.

[3]https://www.cosmos.esa.int/web/xmm-newton/current-calibration-files.

[4]https://www.cosmos.esa.int/web/xmm-newton/sas-threads.

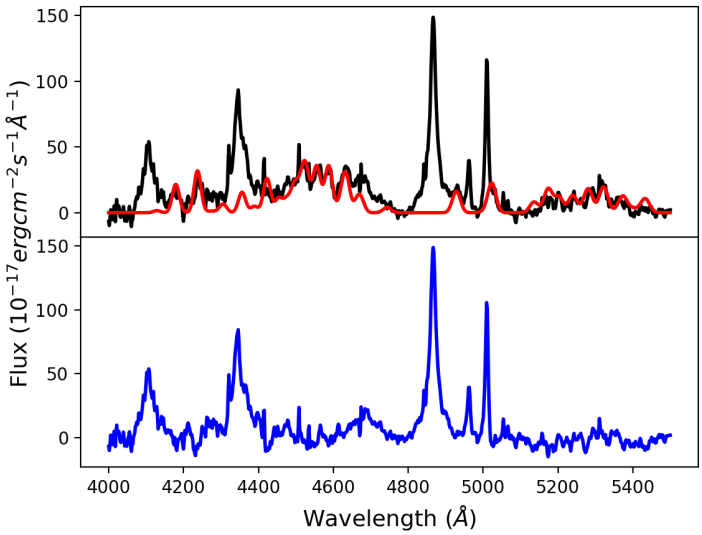

Figure 5.1: The Fe II subtraction of IRAS F21325-6237. *Top panel:* the observed spectrum with continuum subtracted (black line) and the Fe II model (red line). *Bottom panel:* the spectrum with continuum and Fe II subtracted (blue line).

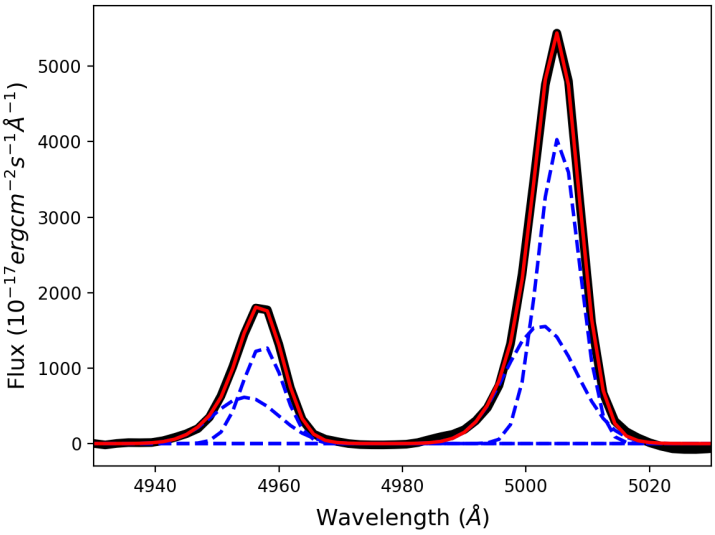

Figure 5.2: The [O III] lines fitting of IGR J19378-0617. The black line indicates the observed spectrum with continuum and Fe II subtracted. The red line indicates the sum of the resulting fit. The dashed blue line indicates the Gaussian components.

velocity measurements of [O III] λ5007 indeed should be more precise than those of [O III] λ4959, due to the weak intensity of [O III] λ4959 compared to that of [O III] λ5007. I also note that three sources do not have a wing velocity measurement. The [O III] lines in J0228 and J0708 are not detected, as common among sources with strong Fe II (Marziani et al., 2018). In J1325 instead the [O III] λ5007 line can be fitted with only one Gaussian component, possibly because of the poor S/N of the optical spectrum.

The errors were evaluated using a Monte Carlo method. I varied the line profile by adding a random Gaussian noise proportional to the root-mean-square (RMS) measured in the continuum. I then fitted the [O III] line with two Gaussian components as previously described, measuring the central wavelength and velocity again, and repeating the same process 100 times to estimate the standard deviation of each measurement. In this way, I obtained 1σ errors for these parameters. The wing velocity has a large average uncertainty of 61.6%.

Table 5.3: The central wavelength of [O III]λ5007 line components and the velocity of blue wing measurements.

Short name	Redshift	Line core	Blue wing	Velocity	Type
-	-	(Å)	(Å)	(km s^{-1})	(C/S)
J0228	0.493	-	-	-	S
J0230	0.016	5006.84 ± 1.66	5003.07 ± 2.41	226.06 ± 175.30	C
J0436	0.036	5007.85 ± 1.16	5002.22 ± 5.42	336.64 ± 331.73	S
J0452	0.247	5007.06 ± 0.05	4999.51 ± 0.68	452.12 ± 40.74	S
J0708	0.041	-	-	-	C
J1325	0.066	-	-	-	C
J1511	0.045	5007.14 ± 0.96	5003.78 ± 1.37	201.02 ± 100.47	S
J1638	0.026	5006.57 ± 2.09	5002.30 ± 3.37	255.51 ± 237.55	C
J1937	0.010	5005.28 ± 1.26	5002.42 ± 2.59	171.08 ± 172.31	C
J2135	0.061	5010.50 ± 2.28	5004.51 ± 2.90	358.41 ± 220.80	S
J2245	0.200	5007.62 ± 0.02	4998.07 ± 0.23	571.65 ± 13.58	S

Columns: (1) short name, (2) redshift, (3) central wavelength of the line core, (4) central wavelength of the blue wing, (5) velocity of the blue wing, (6) X-ray classification, complex (C) or simple (S).

5.3.2 X-ray spectra

I modeled the PN, MOS1, and MOS2 spectra simultaneously using the XSPEC version 12.10.0 (Arnaud, 1996). To identify the simple and complex NLS1s, I fitted the 2-12 keV spectra with a baseline model composing of a power-law continuum modified by Galactic absorption (Gallo, 2006). Sources whose 2-12 keV spectra do not strongly deviate from a simple power-law continuum with a null hypothesis of the baseline model greater than 0.10 are marked as S-NLS1s. Instead, sources that exhibit high-energy complexity with a null hypothesis of the baseline model less than 0.10 are marked as C-NLS1s. In total, there are six S-NLS1s and five C-NLS1s as listed in Table 5.4. However, it is worth noting that some objects might be misclassified due to the limited counts in the X-ray spectra.

Table 5.4: The X-ray spectral classification, reduced Chi-squared and null hypothesis of the baseline model fitting.

Short name	Type	χ^2_ν	Null hypothesis
J0228	S	1.05	0.315
J0230	C	1.76	< 0.10
J0436	S	1.05	0.284
J0452	S	0.72	0.995
J0708	C	1.83	< 0.10
J1325	C	1.39	< 0.10
J1511	S	1.02	0.401
J1638	C	1.20	< 0.10
J1937	C	3.25	< 0.10
J2135	S	1.09	0.213
J2245	S	0.94	0.566

Columns: (1) short name, (2) X-ray classification, complex (C) or simple (S), (3) reduced Chi-squared of the baseline model fitting, (4) null hypothesis of the baseline model fitting.

I further collected the black hole mass from Chen et al. (2018b) and the X-ray flux in 0.2-12.0 keV from the 3XMM-DR8 catalog (Rosen et al., 2016). The X-ray luminosity in 0.2-12.0 keV is calculated using

$$L_X = 4\pi D_L^2 \cdot F_X, \tag{5.1}$$

where D_L is the luminosity distance estimated by the cosmological redshift. Five sources have a harder X-ray flux and luminosity detection in 14-195 keV by the *Swift* BAT 105-month survey (Oh et al., 2018). These values are listed in Table 5.5.

J0228 (IRAS 02262-4110)

I reproduced the spectrum of J0228 between 2-12 keV with a simple power-law model and obtained a $\chi^2_\nu = 1.05$. This indicates that a power-law represents the data very well and thus it is classified as a S-NLS1. The *XMM-Newton* EPIC (PN+MOS1+MOS2) spectra of J0228 in the range of 0.2-12.0 keV can be modeled by two power-law components plus an iron line at the rest frame, as seen in Krumpe et al. (2010).

J0230 (Mrk 1044)

The spectral fitting of J0230 between 2-12 keV reveals that a simple power-law is not a good representation for the data giving a $\chi^2_\nu = 1.76$. Indeed, I classify it as a C-NLS1, as it exhibits a relativistic reflection from a high-density accretion disk with the presence of a strong soft X-ray excess below 1.5 keV, Fe Kα emission complex at 6-7 keV, and a Compton hump at 15-30 keV in its broad-band (0.3-50.0 keV) spectrum (Mallick et al., 2018). This object had been analyzed by Mallick et al. (2018) in detail. The combined *XMM-Newton* EPIC-PN (0.3−10.0 keV), *Swift* XRT (0.3−6.0 keV), and *NuSTAR* FPMA+FPMB (3.0−50.0 keV) spectra of J0230 can be reproduced by a Galactic absorption, a primary power-law emission, an ionized high-density relativistic disk reflection, a neutral distant reflection, and a Gaussian absorption line. I note that J0230 was classified as a S-NLS1 in Gallo (2006), whereas I consider it as a C-NLS1. If the flux state scenario is true, this object might have undergone a flux change from normal to low state.

J0436 (Mrk 618)

A simple power-law modeling in the range of 2-12 keV leads to a $\chi^2_\nu = 1.05$, indicating that J0436 is classified as a S-NLS1. The *XMM-Newton* EPIC-PN spectrum in 0.2-12.0 keV range can be fitted by a Galactic absorption, a weak intrinsic absorption, a power-law continuum, a blackbody component, and a Fe Kα emission line, as reported in Laha et al. (2018).

J0452 (IRAS 04505-2958)

I fitted the spectrum of J0452 between 2-12 keV with a simple power-law component reaching a $\chi^2_\nu = 0.72$, which reveals that J0452 is a S-NLS1. Its *XMM-Newton* EPIC (PN+MOS1+MOS2) spectra in 0.3-10.0 keV can be reproduced by a power-law

plus blackbody model or a relativistically blurred photoionized disk reflection model, with additionally a weak intrinsic absorption, an O VII absorption edge, and a Fe Kα emission line. Both models give acceptable fits, as analyzed by Zhou et al. (2007).

J0708 (1H 0707-495)

J0708 is a well-known C-NLS1s. The spectral fitting in the range of 2-12 keV gives a χ^2_ν = 1.83, indicating that a simple power-law model is not a good representation of the data. Indeed, its X-ray spectrum exhibits evident complex features, such as a sharp drop around 7 keV at the rest frame (Boller et al., 2002) and/or broad iron K and L emission lines (Fabian et al., 2009), which are usually explained as a relativistically blurred reflection from an iron-rich accretion disk. The *XMM-Newton* EPIC-PN time-integrated spectrum of J0708 in 0.3-10.0 keV had been modeled by Kara et al. (2013) in detail, including components: a Galactic absorption, an intrinsic absorption, a blackbody component, two power-law continua, a relativistically blurred component, and two reflectors irradiated by two power-law components. The hard power-law component is originated from a region close to the center with short time-scale variability, and the soft power-law component is produced in an extended region with long variation. Both power-law continua likely contribute to the reflection.

J1325 (IRAS 13224-3809)

J1325 is also a C-NLS1s since a simple power-law fitting between 2-12 keV gives a χ^2_ν = 1.39 which is not an acceptable fit. Its X-ray spectrum indeed shows a remarkable sharp drop at around 8 keV and a significant ionized Fe L absorption feature at around 1.2 keV (Boller et al., 2003). The *XMM-Newton* EPIC (PN+MOS1+MOS2) time-averaged spectra of J1325 in 0.3-10.0 keV can be reproduced by a Galactic absorption, a power-law continuum, a blackbody component either directly originated from the accretion disk or reprocessed the thermal emission, and two relativistically blurred reflections. Details are analyzed by Chiang et al. (2015).

J1511 (IRAS 15091-2107)

A simple power-law is a very good reproduction of the data between 2-12 keV obtaining a χ^2_ν = 1.02, which reveals that J1511 is a S-NLS1s. Its combined *XMM-Newton* EPIC-PN (0.3-10.0 keV) and *INTEGRAL* IBIS (20-100 keV) spectra can be modeled by a partially covering absorption, a power-law continuum, and an iron Kα emission line, as seen in Panessa et al. (2011).

J1638 (IRAS 16355-2049)

The spectral fitting of J1638 gives a $\chi^2_\nu = 1.20$ using a simple power-law between 2-12 keV. Even though the complex feature is not as evident as in some well-know C-NLS1s, considering the confidence level of the null hypothesis, I classified this source as a C-NLS1. This is in agreement with what was found in Panessa et al. (2011), who modeled the combined *XMM-Newton* EPIC-PN (0.3-10.0 keV) and *INTEGRAL* IBIS (20-100 keV) spectra of J1638 by a power-law continuum, a soft emission from plasmas, a multi-blackbody component, and two iron K-shell emission lines.

J1937 (IRAS 19348-0619)

I classify J1937 as a C-NLS1 since a simple power-law can not reproduce the data between 2-12 keV resulting in a very bad spectral fit of $\chi^2_\nu = 3.25$. Indeed, its broad-band X-ray spectrum (0.3-60.0 keV) exhibits extremely complex features, such as dramatic X-ray variability, strong soft excess below 2 keV, evident relativistic reflection, broad Fe Kα line at around 6-7 keV, and Compton hump above 10 keV (Frederick et al., 2018). The combined *XMM-Newton* EPIC-PN (0.3−10.0 keV) and *NuSTAR* FPMA+FPMB (3.0−60.0 keV) time-integrated spectra of J1937 can be modeled by a Galactic absorption, a multi-blackbody accretion disk, and a relativistic reflection model for a lamp post geometry as well as an incident cutoff power-law continuum. Details are analyzed by Frederick et al. (2018).

J2135 (IRAS F21325-6237)

A simple power-law fitting gives a $\chi^2_\nu = 1.09$ in the range of 2-12 keV, indicating that J2135 is a S-NLS1. Since no X-ray spectrum or modeling was published for this object, I reproduced its *XMM-Newton* spectrum in 0.2-12.0 keV using a broken power-law model, which yields a χ^2/d.o.f. $= 354/322 = 1.10$, as shown in Table 5.6 and Fig. 5.3. The broken power-law model gives photon indexes of $\Gamma_1 = 2.29$ and $\Gamma_2 = 1.75$ below and above a break energy of $E_{break} = 1.93$ keV. No high-energy complexity is shown.

J2245 (IRAS F22423-4707)

The spectral fitting with a simple power-law between 2-12 keV reaches a $\chi^2_\nu = 0.94$, suggesting that J2245 is a S-NLS1. This object has never been analyzed in the literature. Its *XMM-Newton* spectrum in the range of 0.2-12.0 keV can be reproduced by a blackbody plus power-law model, yielding a blackbody temperature of $kT = 0.10$ keV and a photon index of $\Gamma = 2.16$. This model has a χ^2/d.o.f. $= 189.4/157 = 1.21$, as seen in Table 5.7

and Fig. 5.4. No complex feature is evident in the high-energy part of the spectrum.

5.4 Discussion

5.4.1 The X-ray complexity

The X-ray spectral complexity is due to the complex Fe K-shell features, which produce strong emission and absorption features around 6-8 keV in the rest frame of the galaxy appearing as a broad emission line or a sharp spectral drop. These spectral features are described as arising from extremely smeared and relativistic reflection from ionized material in the inner parts of the accretion disk surrounding a rapidly spinning black hole, with the additional requirement of strongly super-solar iron abundance (Fabian et al., 2013). An alternative explanation is that the complex Fe K-shell features are caused by a clumpy wind from the inner accretion disk, without requiring any extreme relativistic smearing or super-solar iron abundance (Hagino et al., 2016; Jin et al., 2017b). In this scenario, our line of sight crosses the acceleration region where the outflow or wind is launched. The wind leads to the iron emission and absorption lines covering a wide range of velocities, thereby resulting in a broad emission line or a deep absorption drop around 7 keV.

5.4.2 The flux state scenario

I plotted the relation between the black hole mass $\log_{10} M_{BH}$ and the X-ray luminosity $\log_{10} L_X$, as shown in Fig. 5.5. It is worth noting that there may be a linear correlation as found by Bianchi et al. (2009); Järvelä et al. (2015),

$$\log_{10} L_X = (1.3 \pm 0.4) \times \log_{10} M_{BH} + (35.0 \pm 9.7), \tag{5.2}$$

even though it is not so tight with values of $r = 0.85$ and $p = 1.05 \times 10^{-3}$. Moreover, C-NLS1s and S-NLS1s seem to occupy the low and high $M_{BH} - L_X$ regions of the plot respectively.

I used a two-sample Kolmogorov-Smirnov (K-S) test to examine the distributions of black hole mass and X-ray luminosity of the C-NLS1 and S-NLS1 subsamples. The null hypothesis is that two distributions originate from the same population of sources. I applied the rejection of the null hypothesis at a 90% confidence level corresponding to a value of $p \leq 0.10$, which is at the same confidence level of the classification of C-NLS1s and S-NLS1s. The K-S test on the X-ray luminosity ($p = 0.026$) suggests that C-NLS1s and

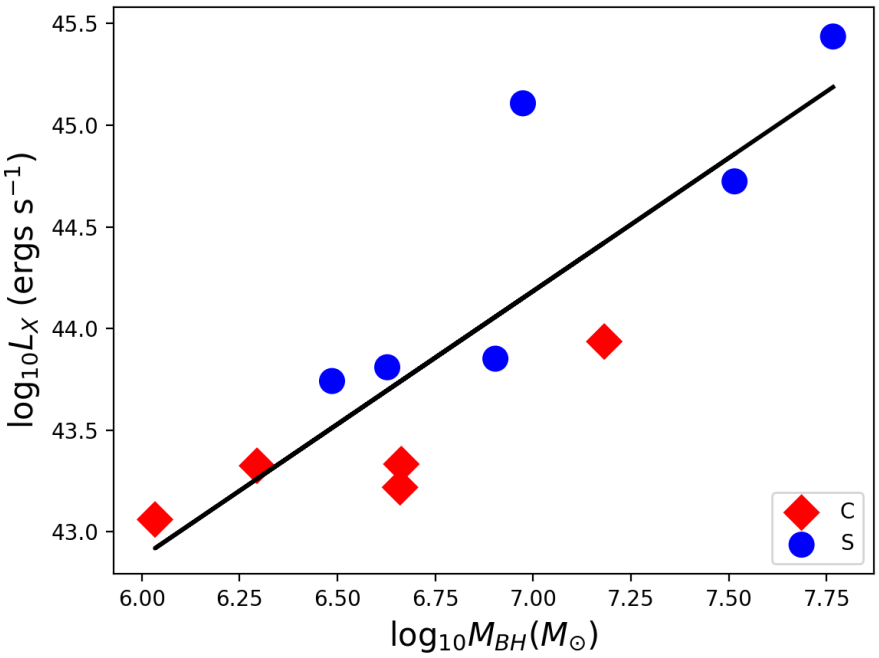

Figure 5.5: The linear correlation (black line) between the black hole mass and the X-ray luminosity for C-NLS1s (red diamonds) and S-NLS1s (blue circles).

S-NLS1s do not originate from the same population. Instead, the K-S test on the black hole mass ($p = 0.454$) suggests that C-NLS1s and S-NLS1s are the same population.

This result seems to be in agreement with the conclusion by Gallo (2006), that is C-NLS1s and S-NLS1s represent sources from the same population but in a low and normal X-ray flux state respectively. According to our results, in fact, C-NLS1s are systematically at a lower luminosity from both *XMM-Newton* and *Swift*-BAT detections, thus the high-energy complexity in the X-ray spectra is visible. If the luminosity becomes higher, the X-ray spectral complexity is less prominent due to the bright continuum overwhelming the emission lines (Foschini, 2012), therefore appearing as S-NLS1s. If this scenario is correct, the classification of S-NLS1s or C-NLS1s is a transient condition, strongly dependent on the activity state of each source.

5.4.3 The outflow scenario

To study the [O III] outflow properties, I plotted the velocity distribution of the blue wings which might be associated with the wind interacting with the NLR material and appearing

as the gas outflows (Berton et al., 2016), as displayed in Fig. 5.6. I found that such outflows from the acceleration region are present in both C-NLS1s and S-NLS1s. Indeed, NLS1s with a high accretion rate are very likely to power a wind by means of the radiation pressure coming from the accretion disk (Proga et al., 2000; Parker et al., 2017).

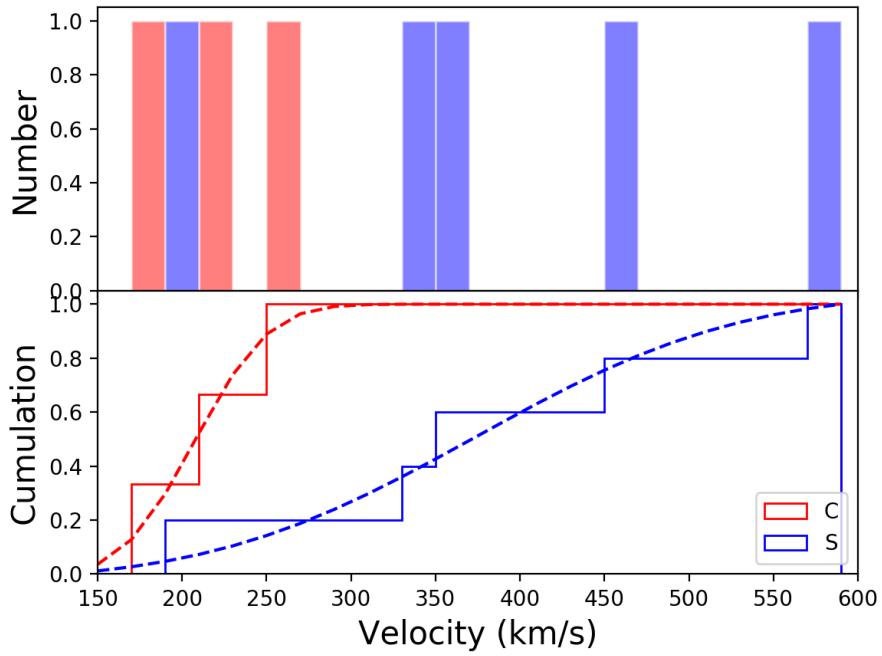

Figure 5.6: The velocity distribution of the blue wing in [O III] λ5007 line for C-NLS1s (red) and S-NLS1s (blue) using a 20 bin width.

As before, I performed a K-S test to verify if the blue wing velocity distribution of the C-NLS1 and S-NLS1 subsamples are the same. I applied the rejection of the null hypothesis that two distributions originate from the same population at a 90% confidence level with a value of $p \leq 0.10$. The result of the K-S test ($p = 0.085$) suggests that the blue wing velocity in C-NLS1s and S-NLS1s have different distributions, even though not in a high confidence level due to the small sample and the large uncertainty of the velocity measurement. The wind in S-NLS1s tends to be faster than that in C-NLS1s.

A possible explanation is that the low velocity of the wind observed in C-NLS1s corresponds to a low energy, which is not sufficient to blow away the ionized material. Therefore, such material remains close to the central engine where it can produce the X-ray complexity. On the other hand, in S-NLS1s the wind velocity and energy are significantly higher,

thus it is able to clean the ionized material in its path and cause the lack of complex feature in the X-ray spectra.

5.4.4 The inclination scenario

As mentioned above, the X-ray spectral complexity might be an inclination effect (Jin et al., 2017a,b). The outflows observed as blue wings in the [O III] lines are mostly directed along the system axis perpendicularly to the accretion disk. If the source is seen at a low inclination, the outflows will be directed toward the observers, and the blueshift will be large. Furthermore, along the system axis the line of sight is free of obscuration because all the ionized material is blown away by such a strong wind. In fact, as shown by a magnetohydrodynamic simulation, outflows along the line of sight ($i < 15°$) are those with higher speeds $\sim$ (0.3-0.4)c (Yuan et al., 2015). At a larger inclination, instead, the blueshifted components of the [O III] lines will be less prominent, and as shown by Jin et al. (2017b), obscuring material will be present along the line of sight, thus producing the observed complexity.

Therefore, S-NLS1s may be sources viewed at small inclination angles, and their blue wings are faster because they are directed toward the observers. Since the line of sight is clear from obscuration, what I observe is the X-ray spectrum of the central engine. Conversely, C-NLS1s are sources viewed at large inclination angles, in which the blueshift of the wings is smaller, and the presence of ionized material leads to the X-ray spectral complexity.

This scenario has important implications on the nature of NLS1s. If this hypothesis is correct, the X-ray complexity could be used as an inclination indicator for these sources. Some authors proposed that the narrow permitted lines typical of NLS1s may be the product of a disk-like BLR observed pole-on (Decarli et al., 2008). In this framework, if C-NLS1s are objects seen at a large inclination with a flat BLR, their permitted lines should be broader than those of S-NLS1s. However, such difference has not been observed (Vietri et al., 2018). This indicates that either C-NLS1s are not viewed at larger angles, or the BLR in NLS1s is not flattened. The latter hypothesis is also in agreement with the physical interpretation of the Lorentzian line profiles observed in NLS1s (Kollatschny & Zetzl, 2013).

However, it is worth noting that this scenario does not account for the difference I observed in the X-ray luminosity of simple and complex sources. As mentioned above, C-NLS1s have on average a lower luminosity with respect to S-NLS1s, and this result seems

to be easily explainable in the flux state scenario. Further observations on a larger sample are needed to confirm or disprove these findings.

5.5 Summary

In this work, I analyzed 11 NLS1s in the 6dFGS sample with both optical and X-ray spectroscopic observations. Combining the optical and X-ray spectral properties, I propose a possible correlation between [O III] line asymmetry and X-ray spectral complexity in NLS1s.

1. The outflow or wind is probably formed via radiation pressure from the inner accretion disk of NLS1s. Its interaction with the material in the inner NLR may be seen in terms of blue wing velocity in the [O III] emission lines. In C-NLS1s only weak wind effects are measured, the X-ray spectral complexity can be well explained by the ionized material in the wind leading to the complex features. On the contrary, the wind effects detected in S-NLS1s are strong and very likely to blow away the ionization material, therefore resulting in the X-ray spectral simplicity.

2. I also suggest that this correlation is due to an inclination effect. S-NLS1s may be sources viewed at small inclination angles, in which the X-ray spectrum is not obscured by any intervening medium. Since the outflows are mostly directed along the system axis, the bulk of the gas is moving toward the observers, and the blueshift of the emission lines is maximum. C-NLS1s instead may be sources viewed at large inclination angles, where the ionized material is still present, and the blueshift effect is less prominent.

However, I remark that these results should be taken with caution because of the limited number of NLS1s used in this analysis and the large uncertainty of the blue wing velocity measurements. Further study on a larger sample and higher S/N ratio spectra will be necessary to unveil the peculiar X-ray properties of NLS1s.

Table 5.2: The *XMM-Newton* observation details of the 11 NLS1s.

3XMM name	Short name	Counterpart	R.A.	Dec.	Observed date	CCD	Count rate	Exp. time
-	-	-	(hh:mm:ss)	(dd:mm:ss)	(yyyy-mm)	-	($cts\,s^{-1}$)	(sec)
3XMM J022815.2-405714	J0228	IRAS 02262-4110	02:28:14.99	-40:57:16.0	2004-12	PN	1.790 ± 0.008	26670
						MOS1	0.343 ± 0.003	31520
						MOS2	0.362 ± 0.003	31550
3XMM J023005.5-085953	J0230	Mrk 1044	02:30:05.50	-08:59:53.0	2013-01	PN	18.740 ± 0.015	85550
						MOS1	3.990 ± 0.007	84900
						MOS2	3.941 ± 0.007	82980
3XMM J043622.2-102233	J0436	Mrk 618	04:36:22.24	-10:22:33.8	2006-02	PN	9.733 ± 0.053	3538
						MOS1	2.149 ± 0.015	9630
						MOS2	2.515 ± 0.017	8883
3XMM J045230.0-295335	J0452	IRAS 04505-2958	04:52:30.08	-29:53:35.3	2003-09	PN	3.822 ± 0.021	8664
						MOS1	0.781 ± 0.008	13820
						MOS2	0.803 ± 0.008	13420
3XMM J070841.4-493306	J0708	1H 0707-495	07:08:41.49	-49:33:06.0	2010-09	PN	5.466 ± 0.007	97710
						MOS1	1.111 ± 0.003	114000
						MOS2	1.079 ± 0.003	116400
3XMM J132519.3-382452	J1325	IRAS 13224-3809	13:25:19.40	-38:24:53.0	2016-08	PN	5.798 ± 0.007	108100
						MOS1	1.095 ± 0.003	125600
						MOS2	1.088 ± 0.003	124800
3XMM J151159.8-211902	J1511	IRAS 15091-2107	15:11:59.78	-21:19:01.6	2005-07	PN	2.895 ± 0.023	5650
						MOS1	0.906 ± 0.008	15090
						MOS2	0.910 ± 0.008	14190
3XMM J163830.8-205524	J1638	IGR J16385-2057	16:38:31.09	-20:55:25.0	2010-02	PN	2.641 ± 0.015	11490
						MOS1	0.761 ± 0.006	24080
						MOS2	0.759 ± 0.006	24080
3XMM J193733.0-061304	J1937	IGR J19378-0617	19:37:33.01	-06:13:04.8	2015-10	PN	19.970 ± 0.015	92900
						MOS1	4.534 ± 0.006	124600
						MOS2	5.041 ± 0.006	125300
3XMM J213529.4-623006	J2135	IRAS F21325-6237	21:36:23.11	-62:24:00.6	2006-11	PN	7.609 ± 0.121	525
						MOS1	1.886 ± 0.013	12060
						MOS2	1.902 ± 0.013	11580
3XMM J224520.2-465211	J2245	IRAS F22423-4707	22:45:20.19	-46:52:13.4	2008-11	PN	2.909 ± 0.036	2255
						MOS1	0.540 ± 0.010	5216
						MOS2	0.528 ± 0.010	5125

Table 5.5: The X-ray flux and luminosity, and black hole mass of the 11 NLS1s.

Short name	$F_{XMM-Newton}$	$\log_{10} L_{XMM-Newton}$	$F_{Swift-BAT}$	$\log_{10} L_{Swift-BAT}$	$\log_{10} M_{BH}$	Type
-	(10^{-12} erg cm^{-2} s^{-1})	(erg s^{-1})	(10^{-12} erg cm^{-2} s^{-1})	(erg s^{-1})	($M_\odot$)	(C/S)
J0228	2.94	45.44	-	-	7.77	S
J0230	34.71	43.33	11.87	42.86	6.29 [a]	C
J0436	24.30	43.85	18.30	43.73	6.90	S
J0452	6.97	45.11	-	-	6.97 [b]	S
J0708	5.61	43.33	-	-	6.66 [c]	C
J1325	8.24	43.94	-	-	7.18 [d]	C
J1511	13.82	43.81	32.67	44.18	6.63	S
J1638	10.43	43.22	20.34	43.51	6.66	C
J1937	49.06	43.06	25.15	42.77	6.03 [e]	C
J2135	6.18	43.74	-	-	6.49	S
J2245	4.61	44.72	-	-	7.51	S

Columns: (1) short name, (2) X-ray flux in 0.2-12.0 keV from the 3XMM-DR8 catalog (Rosen et al., 2016), (3) X-ray luminosity in 0.2-12.0 keV derived by Eq. (5.1), (4) X-ray flux in 14-195 keV from the Swift-BAT 105-month catalog (Oh et al., 2018), (5) X-ray luminosity in 14-175 keV from the Swift-BAT 105-month catalog (Oh et al., 2018), (6) Black hole mass from Chen et al. (2018b), (7) X-ray classification, complex (C) or simple (S). **a.** Other reverberation mapping measurement from the Hβ line gives $M_{BH} = 3.0 \times 10^6 M_\odot$ (Wang & Lu, 2001; Du et al., 2015). **b.** Another black hole mass measurement based on the X-ray variability gives $M_{BH} = 2.0 \times 10^7 M_\odot$ (Zhou et al., 2007). **c.** Other reverberation mapping measurement gives $M_{BH} = 5.0 \times 10^6 M_\odot$ (Zoghbi et al., 2010). **d.** Another black hole mass measurement gives the same $M_{BH} = 1.5 \times 10^7 M_\odot$ (Kaspi et al., 2000). **e.** Other black hole mass estimation from the FWHM of Hβ line gives $M_{BH} = 3.0 \times 10^6 M_\odot$ (Rodríguez-Ardila et al., 2000; Malizia et al., 2008).

Table 5.6: X-ray spectral fitting parameters of J2135

model	**wabs * bknpower**
n_H	3.12×10^{20} cm^{-2}
Γ_1	2.29 ± 0.02
E_{break}	$1.93\ ^{+0.20}_{-0.17}$ keV
Γ_2	$1.75\ ^{+0.05}_{-0.06}$
norm	$(3.34 \pm 0.09) \times 10^{-3}$
c_{MOS1}	1.08 ± 0.03
c_{MOS2}	1.09 ± 0.03
χ^2/d.o.f.	$354/322 = 1.10$

Lines: (1) Galactic hydrogen column density from HI4PI Collaboration et al. (2016), (2) the first photon index of the broken power-law, (3) break energy of the broken power-law, (4) the second photon index of the broken power-law, (5) normalization of the broken power-law, (6) cross-calibration constant for MOS1, (7) cross-calibration constant for MOS2, (8) Chi-squared and degree of freedom.

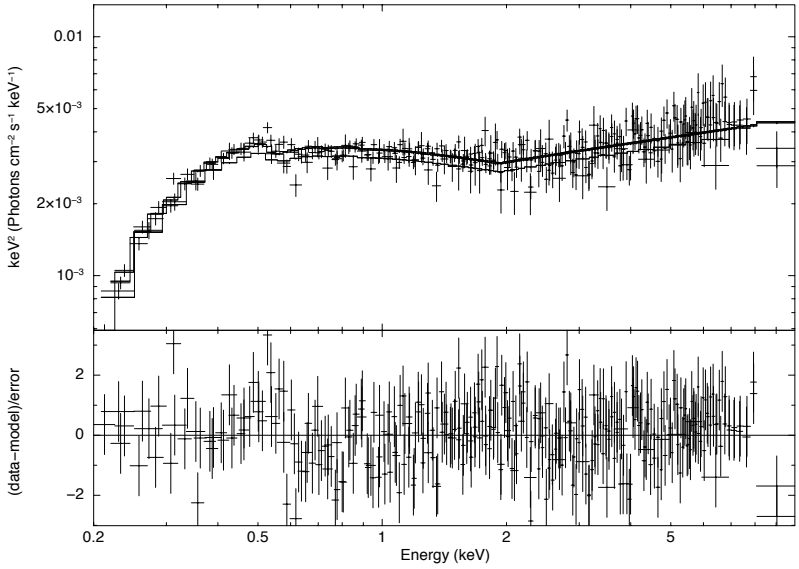

Figure 5.3: The best-fitting model for the X-ray spectrum of J2135 in 0.2-12.0 keV energy band.

Table 5.7: X-ray spectral fitting parameters of J2245

model	**wabs * (zbbody + zpowerlw)**
n_H	0.94×10^{20} cm^{-2}
kT	0.10 ± 0.00 keV
norm	$(5.30 \pm 0.41) \times 10^{-5}$
Γ	2.16 ± 0.07
norm	$(9.35\ ^{+0.58}_{-0.57}) \times 10^{-4}$
c_{MOS1}	0.99 ± 0.04
c_{MOS2}	0.99 ± 0.04
χ^2/d.o.f.	$189.4/157 = 1.21$

Lines: (1) Galactic hydrogen column density from HI4PI Collaboration et al. (2016), (2) temperature of the blackbody, (3) normalization of the blackbody, (4) photon index of the power-law, (5) normalization of the power-law, (6) cross-calibration constant for MOS1, (7) cross-calibration constant for MOS2, (8) Chi-squared and degree of freedom.

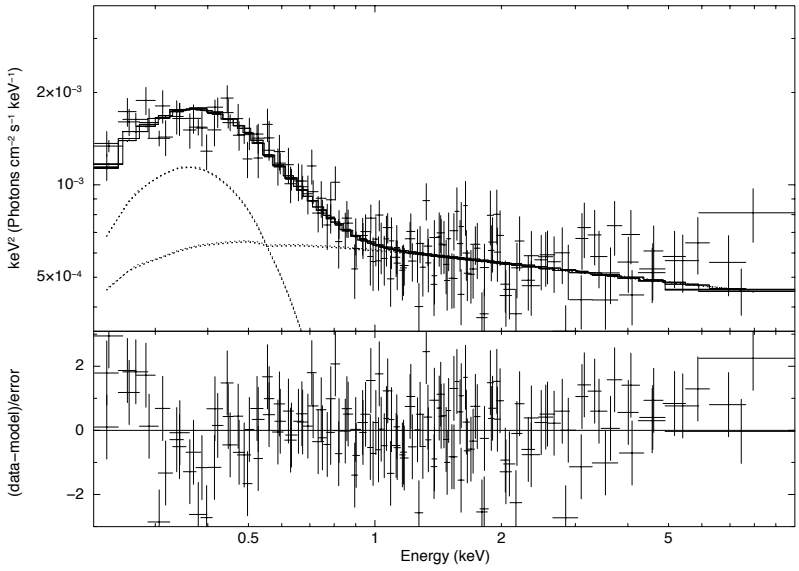

Figure 5.4: The best-fitting model for the X-ray spectrum of J2245 in 0.2-12.0 keV energy band.

Chapter 6

Radio properties of NLS1s in the 6dFGS catalog

In order to study the radio properties of the new NLS1s sample, I proposed a new Karl G. Jansky Very Large Array (JVLA) observation using C-configuration (Proposal ID: VLA/18B-126). I was granted 55 hours observing time in C-band at 5 GHz with a bandwidth of 2 GHz and an angular resolution of 3.5 arcsec for 62 southern NLS1s that have a declination higher than -30° thus can be observed by the JVLA. With the higher resolution and sensitivity of the JVLA compared to the NVSS, the number of radio-detected NLS1s in the southern hemisphere could be increased significantly.

These observations have been carried out and the data reduction is ongoing. Beside looking for new radio-emitting NLS1s, I aim to study their flux, luminosity, radio-loudness, morphology, and spectral index in the sample, to verify the results in Berton et al. (2018) who found that flat-spectrum RL NLS1s mainly have compact morphology and high luminosity, steep-spectrum RL NLS1s often show intermediate or extended morphology and lower luminosity compared to flat-spectrum RL sources although remain brighter than RQ sources, and RQ NLS1s usually exhibit faint diffuse emission on kpc-scales surrounding an unresolved core. In this chapter, I will present the radio properties of 15 NLS1s which were already detected by the NVSS at 1.4 GHz.

6.1 Data reduction

These observations were carried out from November 2018 to February 2019 with an exposure time of 20-30 minutes on each target, yielding an image sensitivity around 7 μJy.

I reduced the data using the Common Astronomy Software Applications (CASA) version 5.5.0 and the standard Expanded VLA (EVLA) data reduction pipeline version 5.4.0. Standard flux density calibrators 3C 147 or 3C 286 were used for each source. The measurement set is in one channel and split off 16 spectral windows (centered on 4.55, 4.68, 4.81, 4.94, 5.06, 5.19, 5.32, 5.45, 5.55, 5.68, 5.81, 5.94, 6.06, 6.19, 6.32, 6.45 GHz) for each target.

To produce the maps, I used a pixel size of 0.5 arcsec to properly sample the beam in C-configuration that has a FWHM of 5 arcsec, and a region of 2048 × 2048 pixels centered on the source coordinates to check for the presence of nearby sources. I modeled the main target along with the nearby sources using the CLEAN algorithm in all spectral windows to avoid the contamination from the sidelobes. For the first tentative image, I used a natural weighting. After the first cleaning, I proceeded with iterative cycles of phase-only self-calibration on the visibility to improve the dynamic range of the final maps. The radio maps of 15 NLS1s observed by the JVLA are shown in Fig. 6.1.

Besides, I also collected the radio maps of these objects observed by the NVSS, as shown in Fig. 6.1. These images have a field of 4 × 4 degrees and a relatively large restoring beam of 45 arcsec FWHM (Condon et al., 1998). Compared to the JVLA maps, no structure is displayed on the NVSS maps.

6.2 Analysis and discussion

I measured the beam size and its position angle, the RMS, and the peak S_p and integrated S_{int} flux density. These sources were re-classified as RL or RQ using

$$R_L = F_{5GHz}/F_{4400\text{Å}}. \tag{6.1}$$

The new classification calculated by the radio flux at 5 GHz is more precise than the previous one converting the radio flux from 1.4 GHz to 5 GHz under the assumption of a power-law spectrum $F_\nu \propto \nu^{-\alpha}$ with a spectral index $\alpha = 0.5$. These NLS1s were both detected by the NVSS at 1.4 GHz and the JVLA at 5.5 GHz respectively, even though these observations are non-simultaneous, the spectral index could be an important sign of the origin of the radio emission. I measured their spectral indexes between 1.4 and 5.5 GHz derived by modeling the spectrum with a power-law. The usual definition gives

$$\alpha = -\frac{\log_{10}(S_1/S_2)}{\log_{10}(\nu_1/\nu_2)}. \tag{6.2}$$

Sources showing $\alpha < 0.5$ have a flat (F) radio spectrum while showing $\alpha > 0.5$ have a steep (S) radio spectrum. Additionally, I studied the morphological classification of these radio maps according to the ratio of the peak to integrated flux density

$$R = S_p/S_{int}. \tag{6.3}$$

Sources having $R > 0.95$ are labeled as compact (C), having $0.75 < R < 0.95$ are labeled as intermediate (I), and having $R < 0.75$ are labeled as extended (E). The peak L_p and integrated L_{int} luminosity were derived by

$$L_\nu = 4\pi D_L^2 \nu S_\nu (1+z)^{1-\alpha}, \tag{6.4}$$

where ν is the observing frequency at 5.5 GHz and D_L is the luminosity distance at a cosmological redshift. All the parameters are reported in Table 6.1. However, I remark that there could be a bias on the spectral index due to the flux variability during the non-simultaneous observations at 1.4 and 5.5 GHz, and a bias on the radio luminosity because the same observed frequency may correspond to different frequencies in the rest frame and different intrinsic components in the radio SED.

The new radio classification gives four RL and 11 RQ objects among these 15 NLS1s, which is the same as the previous classification, except one object J1511-2119 located in the margin of $R_L \sim 10$ changes from RL to RQ. Besides, I note that the four RL NLS1s have a steep radio spectrum, which is likely an indication that the origin of the radio emission is star formation. The other RQ objects show a steep radio spectrum as well but with two exceptions. There is no flat-spectrum RL NLS1 among these 15 sources. However, simultaneous measurements are needed to confirm this result, since variability can strongly contribute to it, especially over such a long period of time. For example, if the two flat-spectrum sources classified as RQ were in a high state when observed in optical and in a low state when observed in radio, this would lead to a wrong classification. Moreover, the radio morphological classification results in seven C sources, three I sources, and five E sources.

I plotted the relation of redshift and radio luminosity for different types of sources as seen in Fig. 6.2, as well as the sensitivity for the JVLA (7 μJy at 5.5 GHz) and NVSS (2.5 mJy at 1.4 GHz) detection respectively. This figure shows that RL NLS1s tend to have higher redshift and radio luminosity compared to RQ NLS1s, which might be a selection effect. Because RQ sources are typically weak, they could be under the flux density limit of the radio survey at a high redshift, while bright RL sources should be detected both in the

nearby and far universe. However, this tendency is not obvious due to the small number of RL sources. Thanks for the high sensitivity of the JVLA compared to the NVSS, more radio sources will be detected in my future analysis to examine this finding. On the other hand, compact, intermediate, and extended sources tend to have similar distribution in the $z - L_X$ plane and do not show obvious differences between the RL and RQ population and between the flat and steep radio spectrum sources due to the limited number of the radio sample.

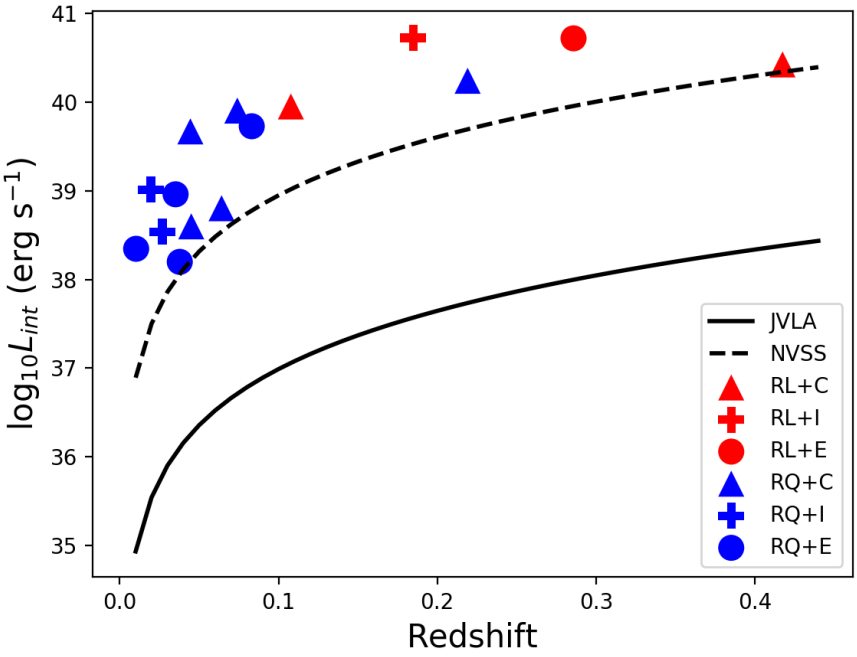

Figure 6.2: The red and blue symbols indicate RL and RQ sources respectively. The triangle, plus, and circle indicate compact, intermediate, and extended sources respectively.

In comparison of the NVSS and JVLA maps, I found a possible radio galaxy associated with J1638-2055. Two bright radio sources are present at the northeast (NE) and southwest (SW) of the NLS1 on the NVSS map, called NVSS J163840-205345 and NVSS J163826-205639 respectively. They are displayed on the JVLA map as well with a resolved structure, as seen in Fig. 6.3. However, both of them do not have an optical counterpart. The NE point has a flux of $f_{1.4GHz}$(NE) = 42.9 mJy and $f_{5.5GHz}$(NE) = 10.8 mJy, and the SW point has a flux of $f_{1.4GHz}$(SW) = 56.9 mJy and $f_{5.5GHz}$(SW) = 13.5 mJy, detected by the NVSS and the JVLA respectively. This yields a non-simultaneous spectral index between

1.4 and 5.5 GHz of α(NE) = 1.01 and α(SW) = 1.05 under the assumption of $F_\nu \propto \nu^{-\alpha}$ for the NE and SW sources respectively, which might point out that they are radio lobes associated with J1638-2055. The NE and SW parts have a distance of 2.791 arcmin and of 1.596 arcmin from the NLS1 in the middle, at redshift $z = 0.026$ corresponding to 91 kpc and 52 kpc respectively. If the hypothesis that they are actually the radio lobes of J1638-2055 is true, this will be the biggest jetted NLS1 found in the sky. However, a more detailed analysis is needed to confirm or disprove this hypothesis.

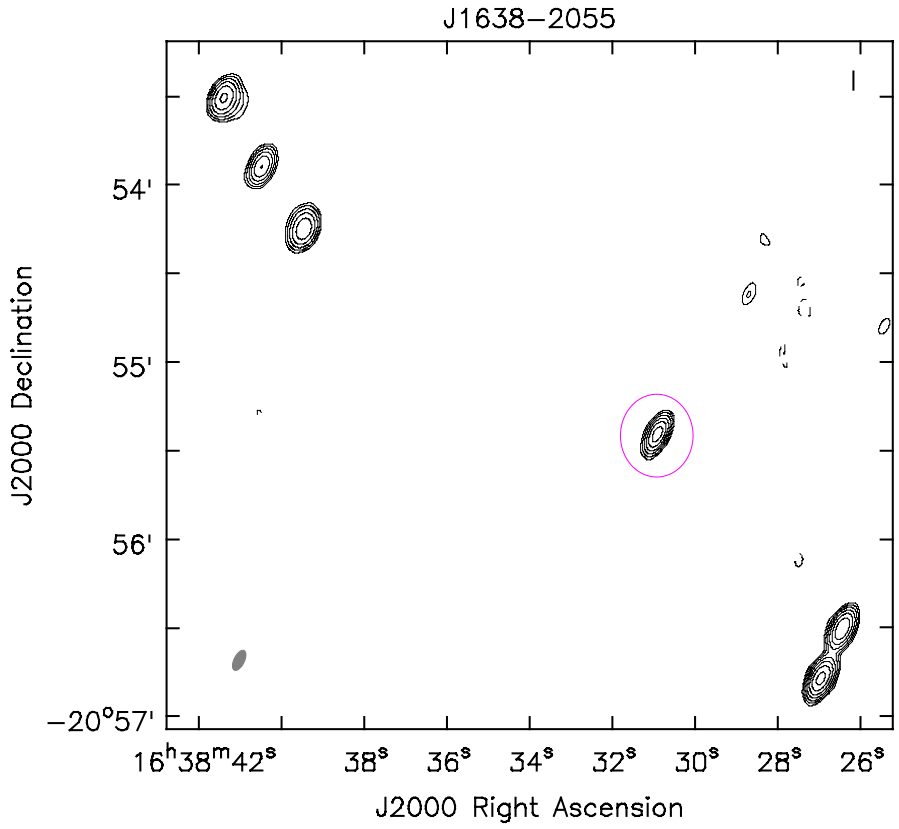

Figure 6.3: The JVLA map of J1638-2055, rms = 25 μJy beam^{-1}, contour levels at -3, 3×2^n, $n \in$ [0,6], beam size 4.23 × 2.01 kpc.

6.3 Results

In this work, I analyzed the radio properties of 15 NLS1s both detected by the NVSS at 1.4 GHz and newly observed by the JVLA at 5 GHz. The results are summarized as follows.

1. I measured the peak and integrated flux and luminosity at 5 GHz, identifying four RL and 11 RQ sources in the radio-loudness classification, as well as seven C, three I, and five E sources in the radio morphological classification. The non-simultaneous spectral index measurements between 1.4 and 5 GHz give 13 sources showing a steep radio spectrum with two exceptions.

2. The distribution between redshift and radio luminosity for different types of sources reveals that, firstly, RL NLS1s tend to have higher redshift and radio luminosity compared to RQ NLS1s, secondly, compact, intermediate, and extended sources do not show an obvious difference between the RL and RQ population and between the flat and steep radio spectrum objects.

The JVLA data reduction and analysis are incomplete and still ongoing. I remark that these results could be a bias due to the small radio sample. I will continue to study the radio properties of the whole NLS1 sample, for the purpose of performing a reliable statistical analysis and examining the possibility of the presence of radio jets in some sources.

Table 6.1: The radio properties of 15 NLS1s observed by the JVLA.

Name	Scale	Beam maj	Beam min	Beam PA	rms	S_{int}	S_p	$\log_{10} L_{int}$	$\log_{10} L_p$	Radio type		Spectral type		Morphological type	
-	(kpc arcsec^{-1})	(arcsec)	(arcsec)	(degree)	(μJy beam^{-1})	(mJy)	(mJy beam^{-1})	(erg s^{-1})	(erg s^{-1})	Type	R_L	Type	$\alpha_{1.4-5.5}$	Type	R
J0122-2646	11.08	10.86	3.21	-32.56	58.0	0.81	0.82	40.42	40.43	RL	32.87	S	1.13	C	1.01
J0422-1854	1.4	6.45	3.47	-22.76	11.0	1.14	1.09	38.8	38.78	RQ	2.35	S	0.66	C	0.96
J0436-1022	0.75	12.3	3.54	-47.45	12.0	5.76	4.13	38.96	38.82	RQ	1.07	S	0.79	E	0.72
J0452-2953	7.12	5.67	3.61	1.4	10.0	3.45	2.58	40.72	40.59	RL	34.42	S	0.74	E	0.75
J0549-2425	0.97	6.15	2.51	-18.0	12.0	1.48	1.53	38.6	38.62	RQ	2.01	F	0.36	C	1.04
J0622-2317	0.81	11.02	4.55	-35.67	12.0	0.87	0.29	38.2	37.72	RQ	0.59	S	1.17	E	0.33
J0846-1214	2.42	3.78	2.04	-2.34	15.0	5.32	5.13	39.95	39.93	RL	14.35	S	0.77	C	0.96
J0952-0136	0.41	7.19	3.45	50.41	35.0	21.5	20.13	39.01	38.98	RQ	5.5	S	0.78	I	0.94
J1147-2145	5.26	8.45	3.94	36.02	15.0	2.12	2.05	40.24	40.22	RQ	6.82	S	0.72	C	0.96
J1511-2119	0.95	7.41	3.16	-23.72	25.0	18.08	17.51	39.67	39.66	RQ	9.79	S	0.7	C	0.97
J1522-0644	1.83	5.12	3.34	-21.38	9.0	5.54	4.12	39.73	39.6	RQ	6.05	S	0.71	E	0.74
J1638-2055	0.57	7.43	3.53	-26.42	14.0	3.75	3.51	38.54	38.51	RQ	0.61	F	0.44	I	0.94
J1646-1124	1.62	6.22	3.24	31.18	31.0	10.82	10.46	39.9	39.89	RQ	3.9	S	0.92	C	0.97
J1937-0613	0.22	4.42	3.36	0.28	10.0	16.96	6.18	38.35	37.91	RQ	2.2	S	0.67	E	0.36
J2021-2235	4.35	6.46	3.22	1.21	15.0	9.51	8.91	40.73	40.7	RL	35.1	S	0.69	I	0.94

Figure 6.1: The radio maps of 15 NLS1s observed by the NVSS and the JVLA.

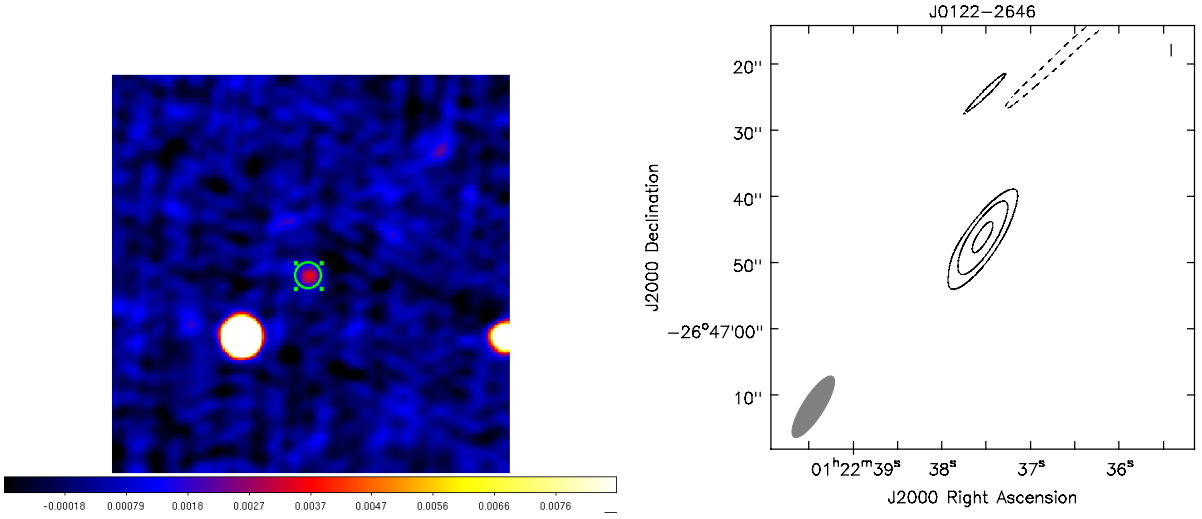

(a) 6dFGS gJ012237.5-264646, *left panel:* the NVSS map, *right panel:* the JVLA map, rms = 58 μJy beam^{-1}, contour levels at -3, 3×2^n, $n \in$ [0,2], beam size 120.24 $\times$ 35.54 kpc.

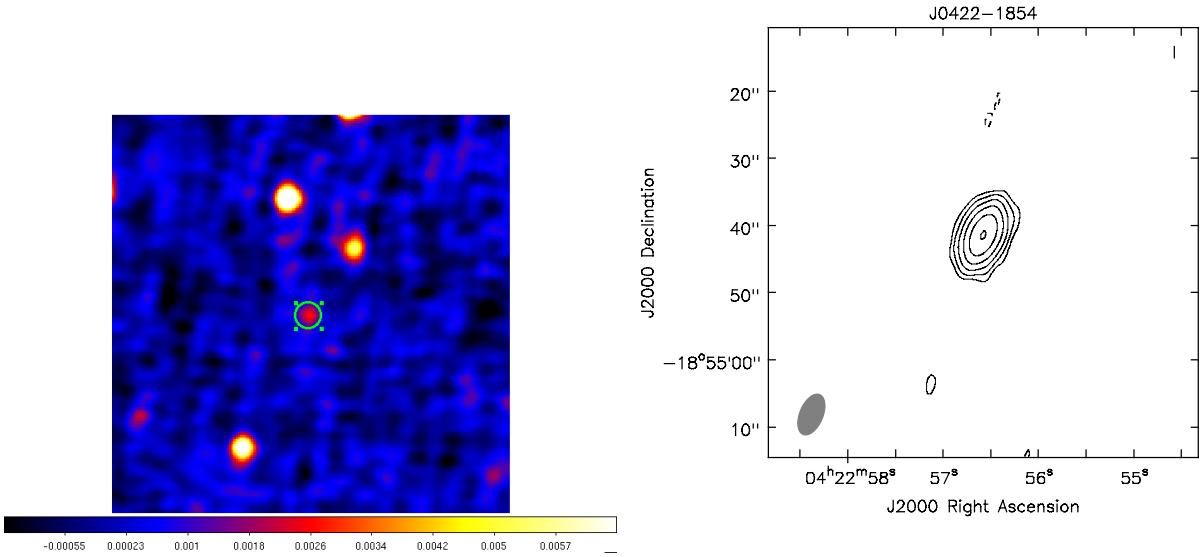

(b) 6dFGS gJ042256.6-185442, *left panel:* the NVSS map, *right panel:* the JVLA map, rms = 11 μJy beam^{-1}, contour levels at -3, 3×2^n, $n \in$ [0,5], beam size 9.00 $\times$ 4.85 kpc.

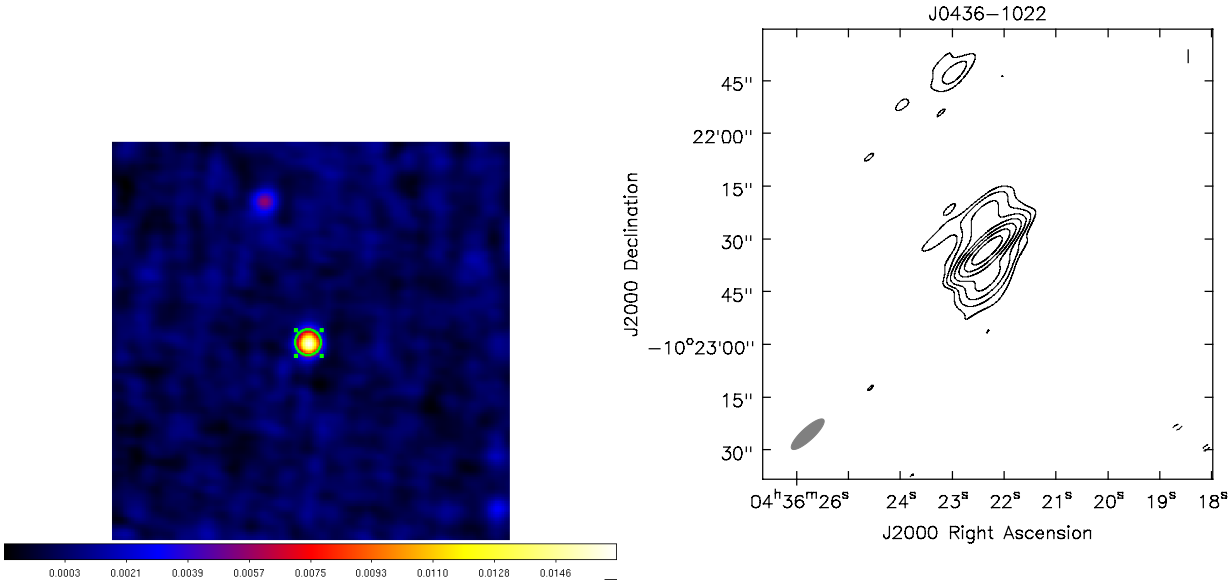

(c) 6dFGS gJ043622.3-102234, *left panel:* the NVSS map, *right panel:* the JVLA map, rms = 12 μJy beam^{-1}, contour levels at -3, 3×2^n, $n \in$ [0,6], beam size 9.22 $\times$ 2.66 kpc.

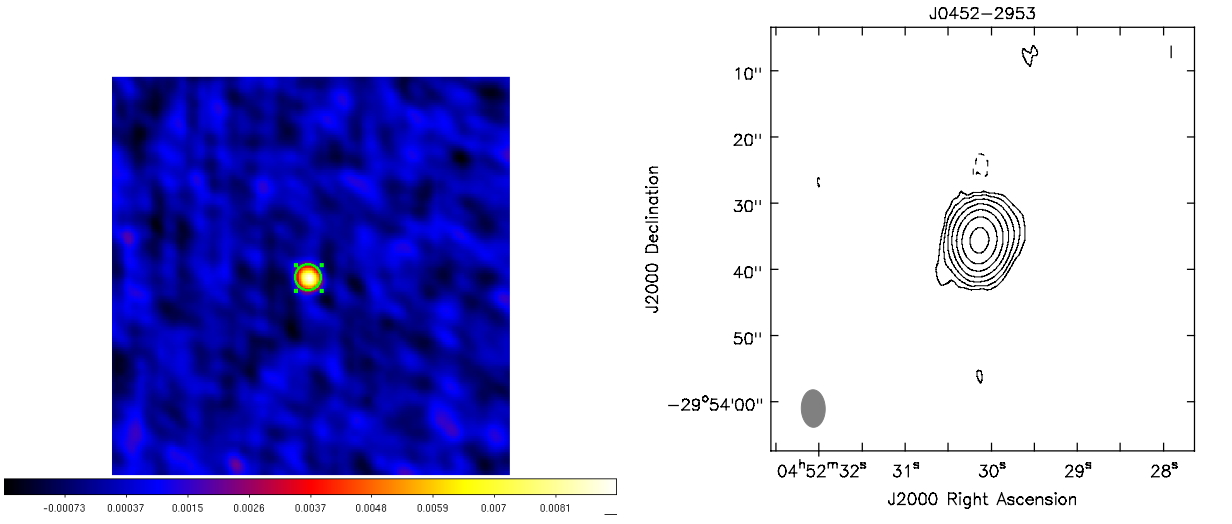

(d) 6dFGS gJ045230.1-295335, *left panel:* the NVSS map, *right panel:* the JVLA map, rms = 10 μJy beam^{-1}, contour levels at -3, 3×2^n, $n \in$ [0,6], beam size 40.35 $\times$ 25.70 kpc.

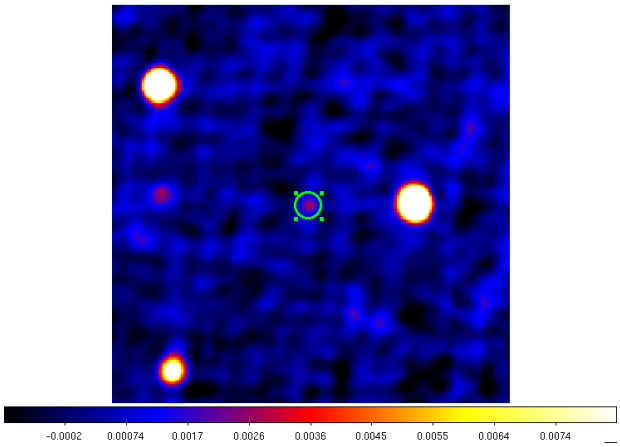

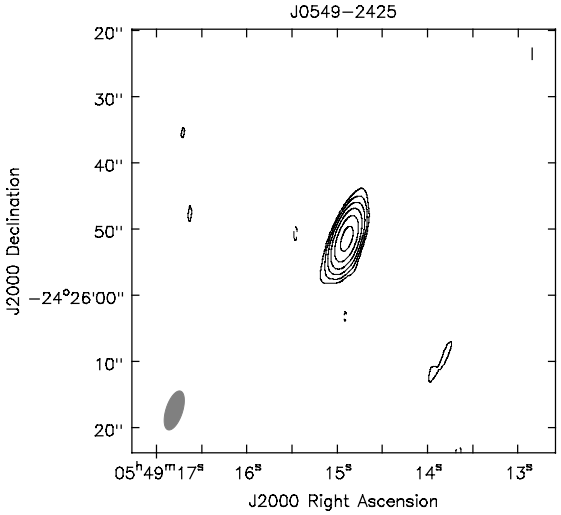

(e) 6dFGS gJ054914.9-242552, *left panel:* the NVSS map, *right panel:* the JVLA map, rms = 12 μJy beam^{-1}, contour levels at -3, 3×2^n, $n \in$ [0,5], beam size 5.95 $\times$ 2.43 kpc.

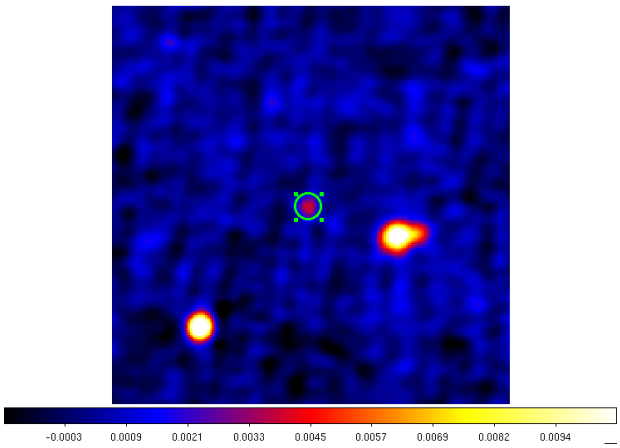

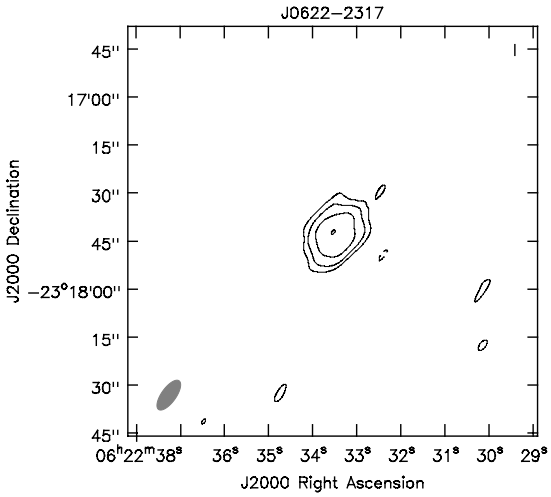

(f) 6dFGS gJ062233.5-231742, *left panel:* the NVSS map, *right panel:* the JVLA map, rms = 12 μJy beam^{-1}, contour levels at -3, 3×2^n, $n \in$ [0,3], beam size 8.89 $\times$ 3.67 kpc.

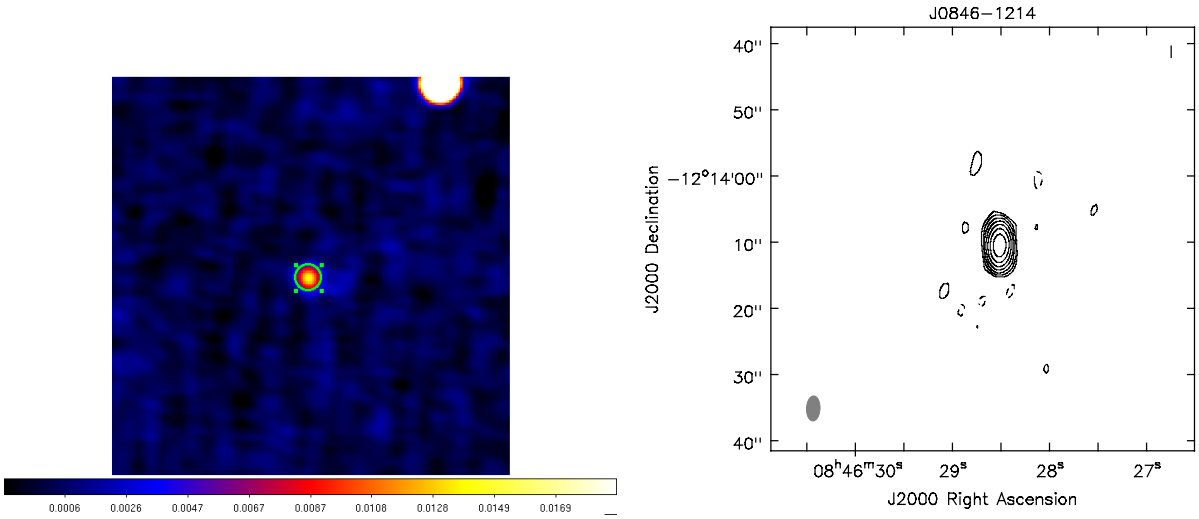

(g) 6dFGS gJ084628.7-121409, *left panel:* the NVSS map, *right panel:* the JVLA map, rms = 15 μJy beam^{-1}, contour levels at -3, 3×2^n, $n \in$ [0,6], beam size 9.13 $\times$ 4.93 kpc.

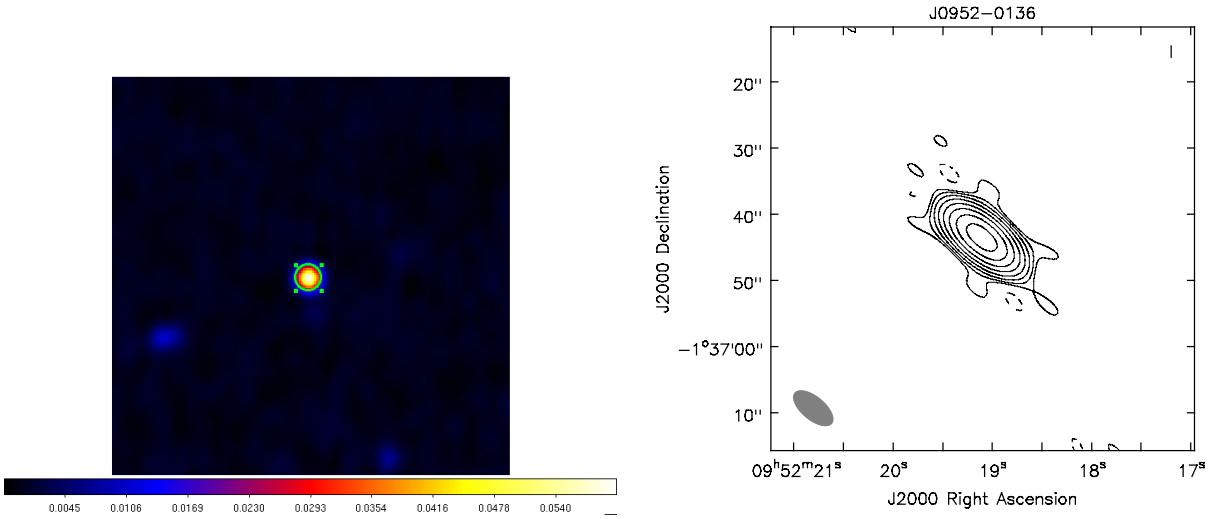

(h) 6dFGS gJ095219.1-013644, *left panel:* the NVSS map, *right panel:* the JVLA map, rms = 35 μJy beam^{-1}, contour levels at -3, 3×2^n, $n \in$ [0,7], beam size 2.97 $\times$ 1.42 kpc.

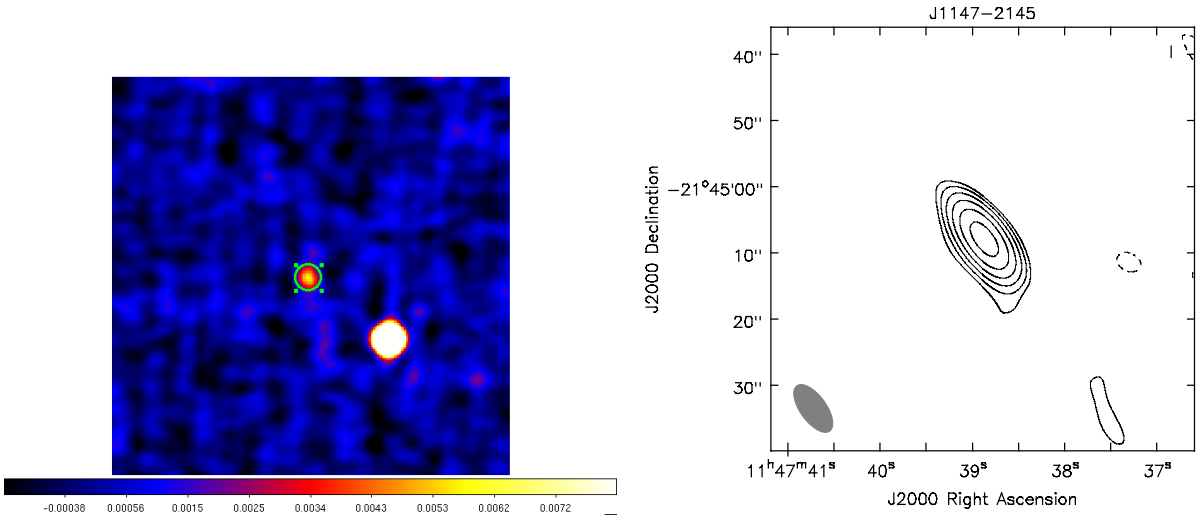

(i) 6dFGS gJ114738.9-214508, *left panel:* the NVSS map, *right panel:* the JVLA map, rms = 15 μJy beam^{-1}, contour levels at -3, 3×2^n, $n \in$ [0,5], beam size 44.47 $\times$ 20.73 kpc.

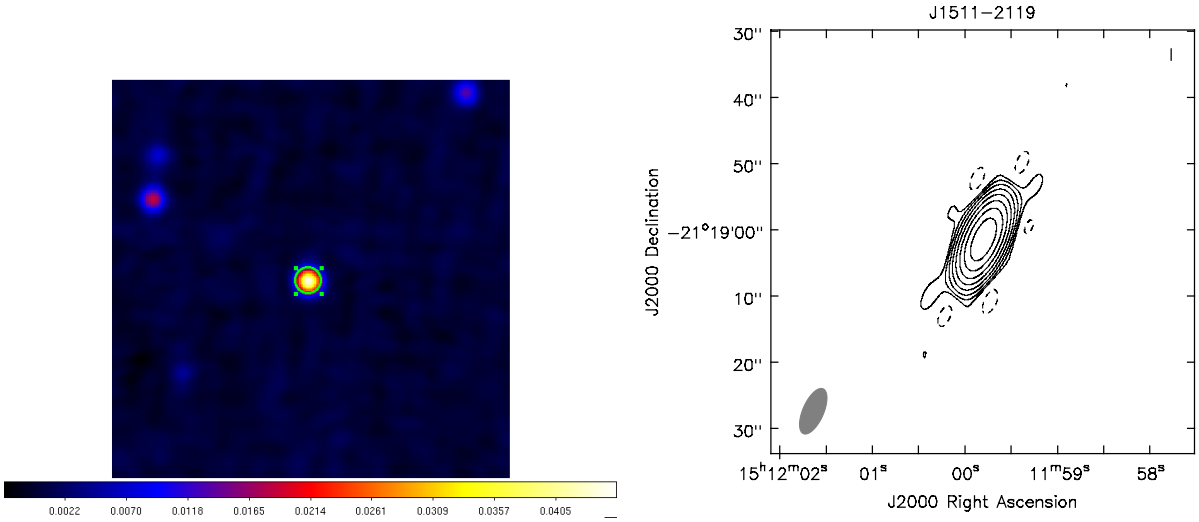

(j) 6dFGS gJ151159.8-211902, *left panel:* the NVSS map, *right panel:* the JVLA map, rms = 25 μJy beam^{-1}, contour levels at -3, 3×2^n, $n \in$ [0,7], beam size 7.07 $\times$ 3.01 kpc.

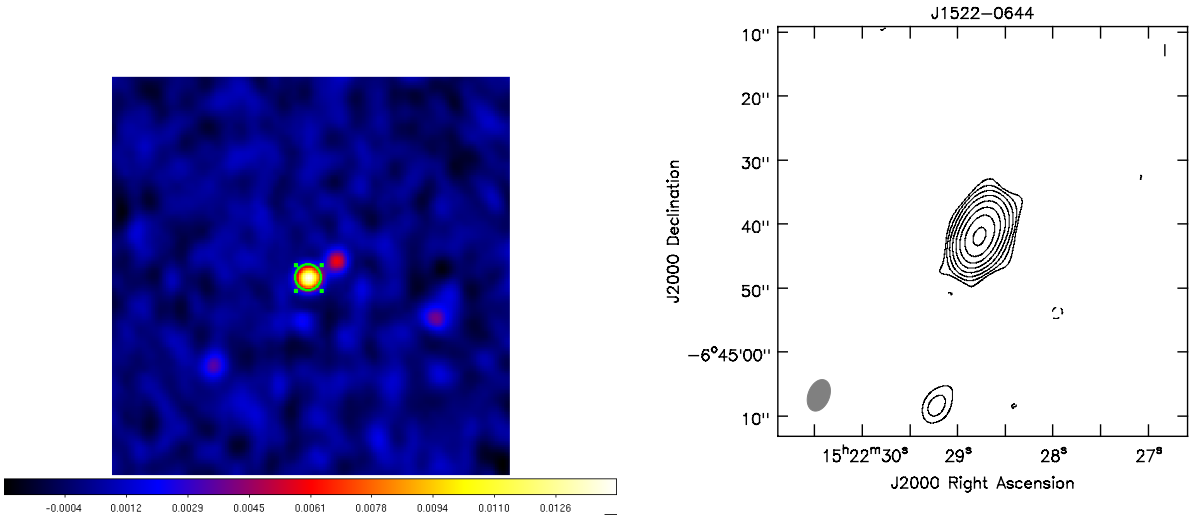

(k) 6dFGS gJ152228.7-064441, *left panel:* the NVSS map, *right panel:* the JVLA map, rms = 9 μJy beam^{-1}, contour levels at -3, 3×2^n, $n \in$ [0,7], beam size 9.39 × 6.12 kpc.

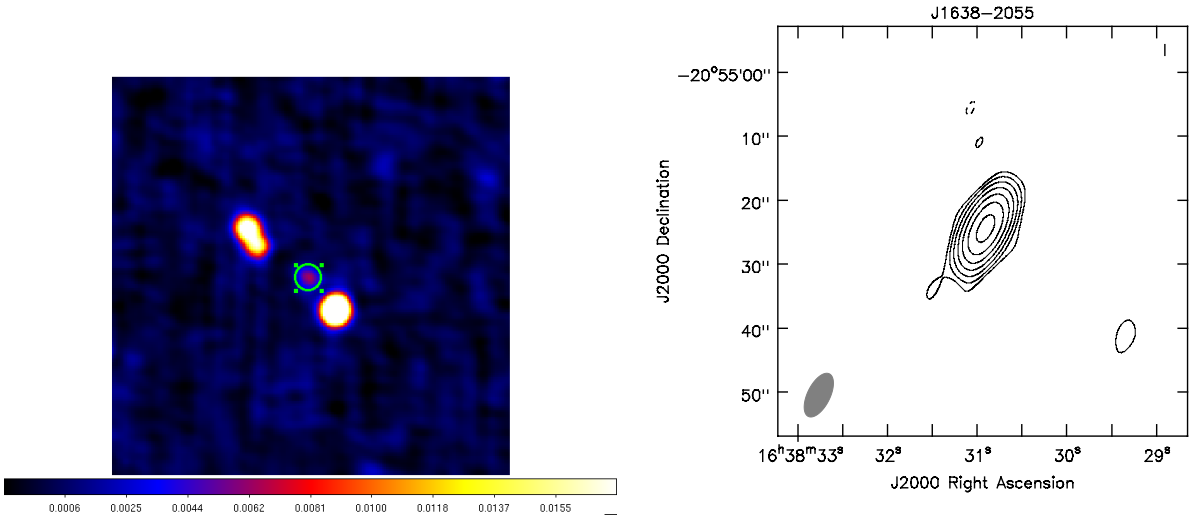

(l) 6dFGS gJ163830.9-205525, *left panel:* the NVSS map, *right panel:* the JVLA map, rms = 14 μJy beam^{-1}, contour levels at -3, 3×2^n, $n \in$ [0,6], beam size 4.23 × 2.01 kpc.

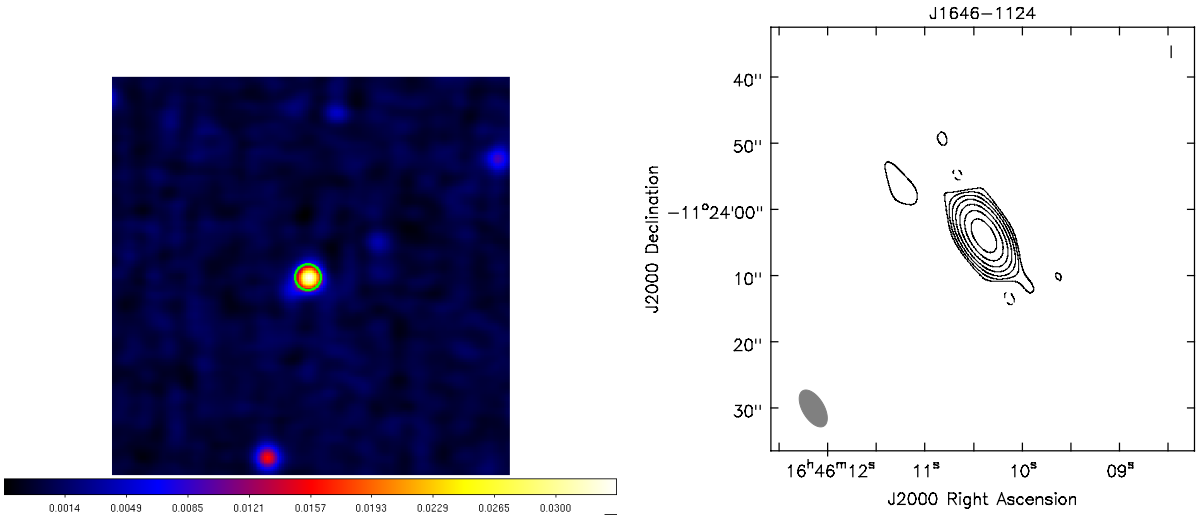

(m) 6dFGS gJ164610.4-112404, *left panel:* the NVSS map, *right panel:* the JVLA map, rms = 31 μJy beam^{-1}, contour levels at -3, 3×2^n, $n \in$ [0,6], beam size 10.09 $\times$ 5.26 kpc.

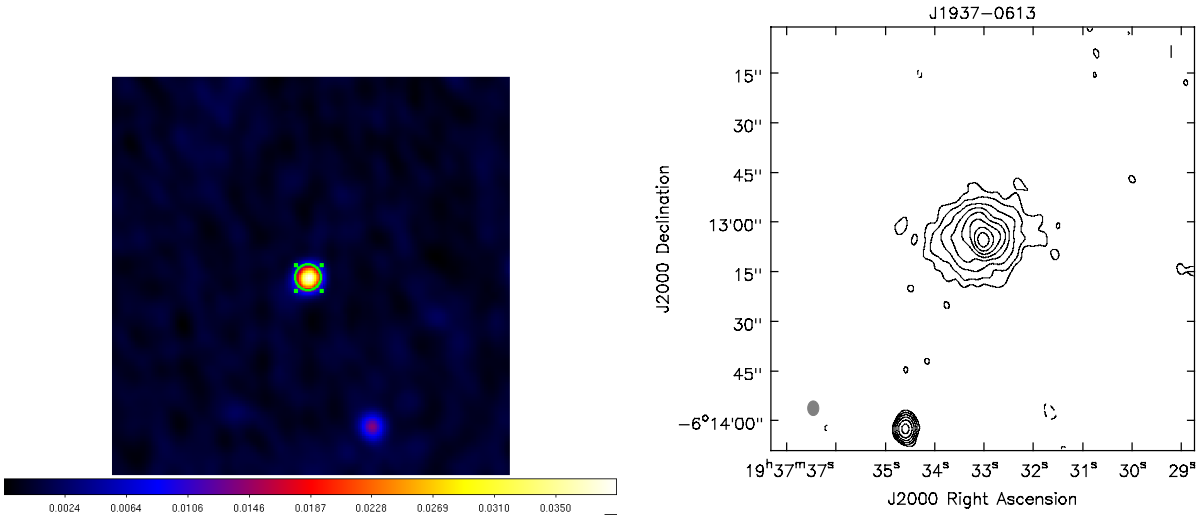

(n) 6dFGS gJ193733.0-061305, *left panel:* the NVSS map, *right panel:* the JVLA map, rms = 10 μJy beam^{-1}, contour levels at -3, 3×2^n, $n \in$ [0,7], beam size 0.95 $\times$ 0.72 kpc.

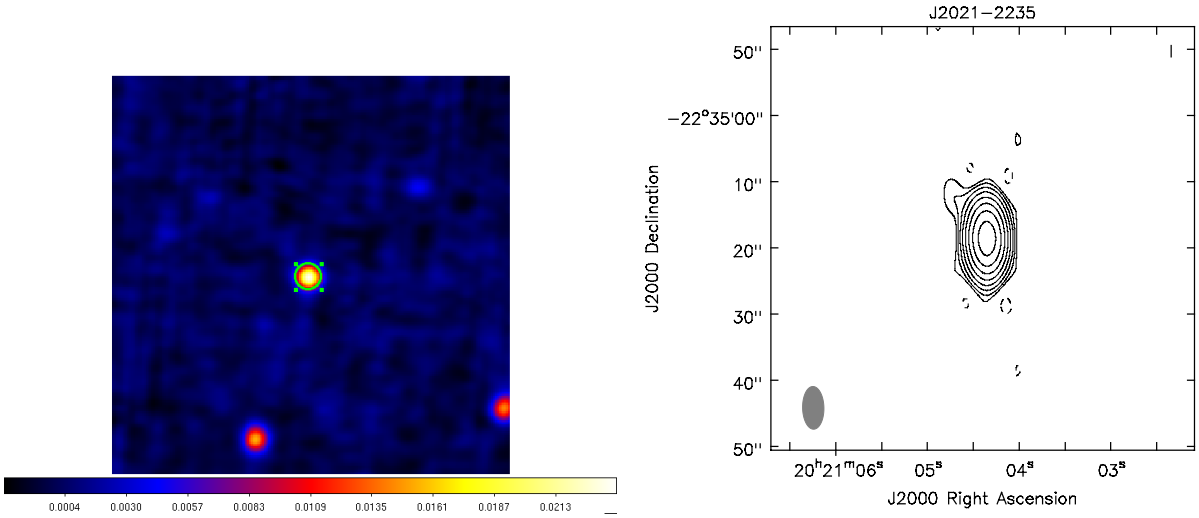

(o) 6dFGS gJ202104.4-223518, *left panel:* the NVSS map, *right panel:* the JVLA map, rms = 15 μJy beam^{-1}, contour levels at -3, 3×2^n, $n \in [0,7]$, beam size 28.10 × 14.03 kpc.

Chapter 7

Conclusions

7.1 Summary

During my Ph.D., I carried out a study of multi-wavelength properties of AGN, in particular NLS1s, including radio, optical, X-ray, and γ-ray bands. A graphical workflow is shown in Fig. 7.1.

Beginning from the optical band, I created a new catalog including 167 NLS1s in the southern hemisphere based on the optical spectroscopic properties. This result increases the number of NLS1s. I further derived the flux-calibrated spectra for these objects which are not provided by the 6dFGS. By analyzing these spectra, I obtained strong correlations between the monochromatic luminosity at 5100 Å and the luminosities of Hβ and [O III] λ5007 lines, as found by literature. The black hole mass was estimated by the virial theorem via the relationship between the BLR radius and the luminosity at 5100 Å continuum from the reverberation mapping measurements. It confirms that NLS1s indeed host a relatively small massive black hole with $M_{BH} \sim 10^6 - 10^8 M_{\odot}$ compared to BLS1s, and can explain many observational phenomenons. Such as the visibility of Fe II multiplets indicates that they are type I AGN having unobscured accretion disk and BLR. The narrow permitted lines in NLS1s are generally due to a low rotational velocity of the gas in the BLR around a relatively undermassive central black hole with respect to BLS1s. Moreover, NLS1s preferably reside in spiral galaxies and nearby universe suggesting that they are likely formed recently in the cosmic time.

In the X-ray band, I analyzed the optical and X-ray spectra of 11 NLS1s and propose a possible correlation between the [O III] line property and the X-ray spectral complexity. The opinion is that the outflow or wind is commonly formed via the radiation pressure

from the inner accretion disk of NLS1s, and it affects the surrounding gas with a strength that can be estimated by the blue wing velocity of the optical emission lines from the NLR. The blue wing velocity in C-NLS1s tends to be small. The X-ray spectral complexity could be due to the ionized material in the weak wind leading to the complex features. On the contrary, the wind in S-NLS1s is strong and likely to blow away the ionized material, therefore resulting in the X-ray spectral simplicity. I also suggest that this scenario could be an inclination effect. The outflow is mostly launched along the system axis. S-NLS1s are sources viewed at a small inclination, where the outflow is moving directed toward the observers. Such a strong wind cleans the ionized material in its path, thus results in a simple X-ray spectra. Instead, at a large inclination, the outflow is less prominent, hence the presence of ionized material leads to the X-ray spectral complexity. However, I remark that these results should be taken with caution because of the limited number of NLS1s used in this analysis and the large uncertainty of the blue wing velocity measurements.

A fraction of NLS1s are detected at radio frequencies. I studied the radio properties of 23 objects at 1.4 GHz and of 15 objects at 5 GHz. RL sources tend to locate in the more distant universe, host a large massive black hole, and have a higher radio and optical luminosity compared to RQ sources. However, the radio morphological characteristics seems to have similar distribution between RL and RQ population, and the spectral indexes between 1.4 and 5.5 GHz from non-simultaneous observations do not show any connection between sources with different radio morphological classification. This could be a bias caused by the limited number of radio sources I analyzed. Besides, I generated the TS maps for 23 radio-emitting sources using the *Fermi*-LAT ten years data set, there is no γ-ray NLS1 in the radio-detected subsample. However, I can not rule out that γ-ray sources might be present in the radio-silent subsample.

7.2 Perspectives

I plan to continue the previous JVLA study and propose new radio observations for the whole NLS1 sample, to investigate the radio properties between RL and RQ populations, and to perform a reliable statistical analysis with a large sample. I aim to verify the results in Berton et al. (2018), who found that flat-spectrum RL NLS1s mainly have compact morphology and high luminosity, steep-spectrum RL NLS1s often show intermediate or extended morphology and lower luminosity compared to flat-spectrum RL sources although remain brighter than RQ sources, and RQ NLS1s usually exhibit faint diffuse emission on

kpc-scales surrounding an unresolved core.

The results of the JVLA observations will provide potential targets that are dominated by jet activity or star formation. On one hand, I intend to propose follow-up VLBA observations, as high-resolution radio observations will resolve the radio core, to unveil if a jet-like structure is present or if a diffuse emission associated with star forming is visible. On the other hand, observations at millimeter/sub-millimeter frequencies, which is the missing piece in my multi-wavelength projects of NLS1s, can make a great contribution in separating the radiation from jet activity or star formation more efficiently (although adding the dusty torus component) (Morganti et al., 2015). I aim to investigate the interplay between a relativistic jet and star formation, and any possible form of positive or negative feedback. Since jetted NLS1s are young AGN harboring a relativistic jet and hosted by spiral galaxies with an ongoing star formation, they are an important laboratory in studying this topic. To do this, I will firstly propose the APEX telescope (South) and/or the NOEMA interferometer of IRAM (North), in order to obtain flux estimates that will pave the way to the ALMA high resolution and sensitivity observations.

In addition, I plan to carry out a morphological study of NLS1s and their environment, in particular their host galaxy, which could be an independent indicator of the black hole mass. Typically, spiral galaxies are associated with low-mass black holes, while elliptical galaxies harbor high-mass black holes (Salucci et al., 2000; Kormendy & Ho, 2013). For this reason, a morphological study of the host galaxy could be a different way to verify if NLS1s are young in the AGN family. In this aspect, those advanced facilities, such as the Keck telescopes (North) and the Very Large Telescope (VLT) (South), can make a great contribution in high-resolution imaging even if the source is located in the far universe. Therefore, I will explore the archive data and propose photometric observations, to investigate the co-evolution of the AGN and their host galaxy which is still unclear (Berton et al., 2019).

Furthermore, I intend to propose high-resolution optical and X-ray spectroscopic observations for a sample of jetted and non-jetted NLS1s, with the aim of further investigating the outflow from the inner accretion disk, which is associated with emission lines in optical and X-ray spectra. On one hand, I am interested in studying the interplay between the relativistic jet and the outflow. On the other hand, I expect to verify if the X-ray spectral complexity in NLS1s is related to the strength of the outflow with a larger sample, which might be explained as an inclination effect due to the different speed of the outflow at different viewing angles. Besides, I could study the correlation between the radio and X-ray

properties, which is currently unclear.

Finally, I remark that NLS1s are a peculiar class of AGN making them hard to be included in the orientation-driven AGN unification model. Current studies tend to favor the scenario that NLS1s are a young and fast-growing phase of AGN that can well explain many observational phenomenons. However, further research will be necessary to carry out, for the propose of clarifying many fundamental mechanism of NLS1s with respect to other types of AGN.

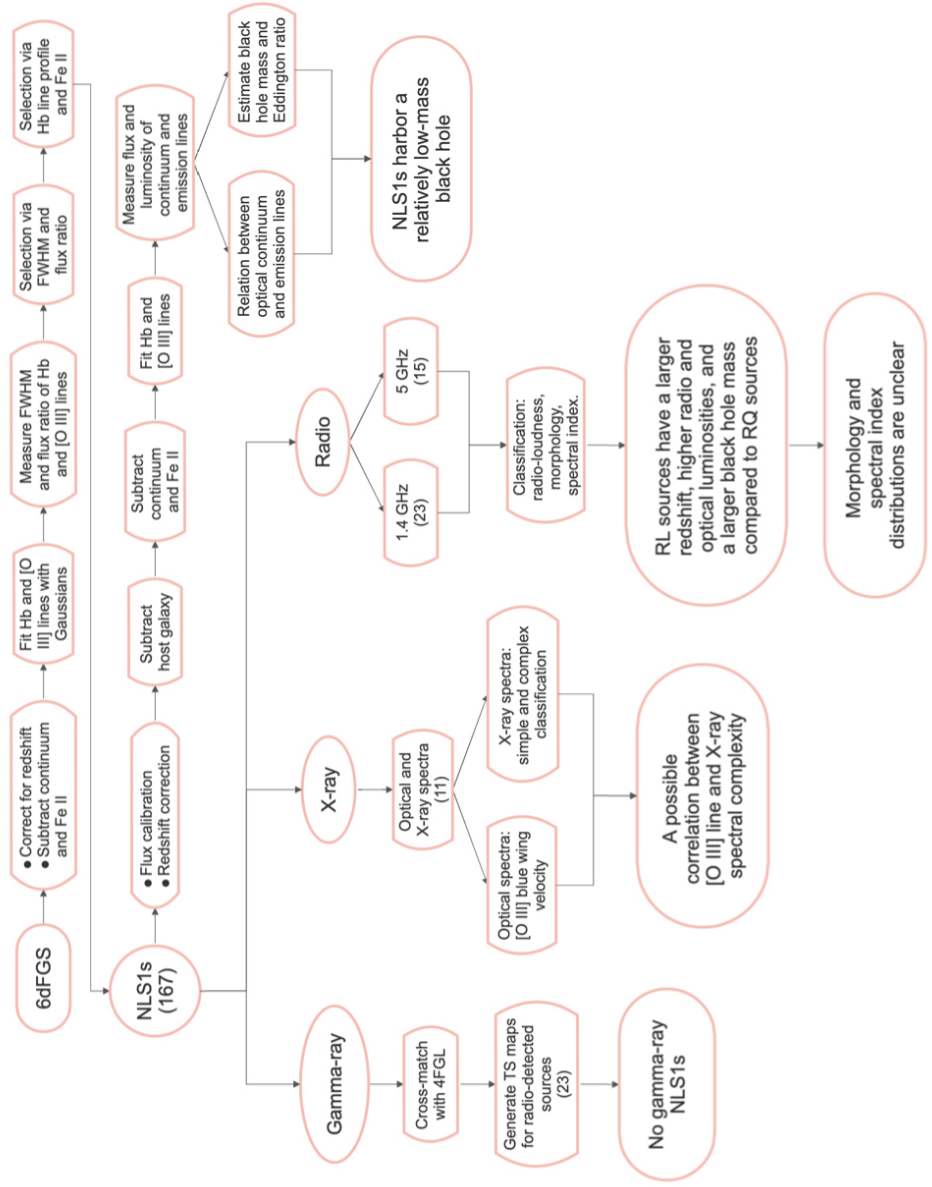

Figure 7.1: A graphical workflow of my Ph.D. thesis.

Acknowledgements

First of all, I would like to express my sincere gratitude to my supervisors Prof. Piero Rafanelli, Dr. Stefano Ciroi, Dr. Marco Berton, and Dr. Giovanni La Mura, for the continuous support of my Ph.D. study and related research, for their patience, motivation, and immense knowledge. Their guidance helped me in all the time of research, from selecting a research topic, to observing and data analyzing, finding a solution, publishing the results, and finally writing this thesis. I could not have imagined having better advisors and mentors for my Ph.D. study.

I would like to thank my dissertation committee members, for their great support and insightful comments to improve my final dissertation.

I would like to acknowledge Prof. Denis Bastieri and Prof. JunHui Fan, for providing me an opportunity to join the doctoral training project between the University of Padova and the University of Guangzhou. Without this, I could not be a Ph.D. student in the University of Padova.

In addition, I am grateful to my AGN group, my collaborators, and my colleagues. You are fantastic researchers. You supported me greatly and were always willing to help me. Many thanks for your wonderful collaboration.

I would like to thank my family, my parents and grandparents, for supporting me throughout my life in general. You are always there for me.

Last but not least, I would like to thank my friends, for providing happy distraction to rest my mind outside of my research.

Thanks for all your encouragement!

Bibliography

Abdo, A. A., Ackermann, M., Ajello, M., et al. 2009a, ApJ, 699, 976

—. 2009b, ApJ, 707, 727

—. 2009c, ApJL, 707, L142

Angelakis, E., Fuhrmann, L., Marchili, N., et al. 2015, A&A, 575, A55

Antonucci, R. 1993, Annu. Rev. Astron. Astrophys., 31, 473

Arnaud, K. A. 1996, in Astronomical Society of the Pacific Conference Series, Vol. 101, Astronomical Data Analysis Software and Systems V, ed. G. H. Jacoby & J. Barnes, 17

Balbus, S. A., & Hawley, J. F. 1992, ApJ, 400, 610

Baldi, R. D., Capetti, A., Robinson, A., Laor, A., & Behar, E. 2016, MNRAS, 458, L69

Beckmann, V., & Shrader, C. R. 2012, Active Galactic Nuclei

Bennert, N., Falcke, H., Shchekinov, Y., & Wilson, A. S. 2004, in IAU Symposium, Vol. 222, The Interplay Among Black Holes, Stars and ISM in Galactic Nuclei, ed. T. Storchi-Bergmann, L. C. Ho, & H. R. Schmitt, 307–308

Bentz, M. C., Denney, K. D., Grier, C. J., et al. 2013, ApJ, 767, 149

Berton, M., Foschini, L., Ciroi, S., et al. 2016, A&A, 591, A88

—. 2015, A&A, 578, A28

Berton, M., Foschini, L., Caccianiga, A., et al. 2017, Frontiers in Astronomy and Space Sciences, 4, 8

Berton, M., Congiu, E., Järvelä, E., et al. 2018, A&A, 614, A87

Berton, M., Congiu, E., Ciroi, S., et al. 2019, AJ, 157, 48

Bianchi, S., Bonilla, N. F., Guainazzi, M., Matt, G., & Ponti, G. 2009, A&A, 501, 915

Blandford, R. D., & Znajek, R. L. 1977, MNRAS, 179, 433

Boller, T. 2000, New Astron. Rev., 44, 387

Boller, T., Brandt, W. N., & Fink, H. 1996, A&A, 305, 53

Boller, T., Tanaka, Y., Fabian, A., et al. 2003, MNRAS, 343, L89

Boller, T., Fabian, A. C., Sunyaev, R., et al. 2002, MNRAS, 329, L1

Bon, E., Marziani, P., Berton, M., et al. 2018, in Revisiting Narrow-Line Seyfert 1 Galaxies and their Place in the Universe, 7

Boroson, T. A., & Green, R. F. 1992, ApJS, 80, 109

Böttcher, M., Reimer, A., Sweeney, K., & Prakash, A. 2013, ApJ, 768, 54

Brandt, W. N., Mathur, S., & Elvis, M. 1997, MNRAS, 285, L25

Bridle, A. H., Hough, D. H., Lonsdale, C. J., Burns, J. O., & Laing, R. A. 1994, AJ, 108, 766

Burrows, D. N., Hill, J. E., Nousek, J. A., et al. 2005, Space Sci. Rev., 120, 165

Caccianiga, A., Severgnini, P., Della Ceca, R., et al. 2008, A&A, 477, 735

Carilli, C. L., & Barthel, P. D. 1996, A&ARv, 7, 1

Cash, W. 1979, ApJ, 228, 939

Chen, S., Berton, M., La Mura, G., et al. 2018a, in Revisiting Narrow-Line Seyfert 1 Galaxies and their Place in the Universe, 4

Chen, S., Berton, M., La Mura, G., et al. 2018b, A&A, 615, A167

Chiang, C.-Y., Walton, D. J., Fabian, A. C., Wilkins, D. R., & Gallo, L. C. 2015, MNRAS, 446, 759

Collin, S., & Kawaguchi, T. 2004, A&A, 426, 797

Collin, S., Kawaguchi, T., Peterson, B. M., & Vestergaard, M. 2006, A&A, 456, 75

Condon, J. J., Cotton, W. D., Greisen, E. W., et al. 1998, AJ, 115, 1693

Connolly, A. J., Szalay, A. S., Bershady, M. A., Kinney, A. L., & Calzetti, D. 1995, AJ, 110, 1071

Cracco, V., Ciroi, S., Berton, M., et al. 2016, MNRAS, 462, 1256

Crummy, J., Fabian, A. C., Gallo, L., & Ross, R. R. 2006, MNRAS, 365, 1067

D'Ammando, F., Orienti, M., Larsson, J., & Giroletti, M. 2015, MNRAS, 452, 520

D'Ammando, F., Orienti, M., Finke, J., et al. 2016, MNRAS, 463, 4469

Davidson, K., & Kinman, T. D. 1978, ApJ, 225, 776

Decarli, R., Dotti, M., Fontana, M., & Haardt, F. 2008, MNRAS, 386, L15

Deo, R. P., Crenshaw, D. M., & Kraemer, S. B. 2006, AJ, 132, 321

Dewangan, G. C., Griffiths, R. E., Dasgupta, S., & Rao, A. R. 2007, ApJ, 671, 1284

Doi, A., Nagira, H., Kawakatu, N., et al. 2012, ApJ, 760, 41

Done, C. 2007, Progress of Theoretical Physics Supplement, 169, 248

Done, C., Davis, S. W., Jin, C., Blaes, O., & Ward, M. 2012, MNRAS, 420, 1848

Du, P., Hu, C., Lu, K.-X., et al. 2015, ApJ, 806, 22

Elitzur, M., & Shlosman, I. 2006, ApJL, 648, L101

Fabian, A. C., Iwasawa, K., Reynolds, C. S., & Young, A. J. 2000, Publ. Astron. Soc. Pac., 112, 1145

Fabian, A. C., Zoghbi, A., Ross, R. R., et al. 2009, Nature, 459, 540

Fabian, A. C., Kara, E., Walton, D. J., et al. 2013, MNRAS, 429, 2917

Fanaroff, B. L., & Riley, J. M. 1974, MNRAS, 167, 31P

Ferrarese, L., & Merritt, D. 2000, ApJL, 539, L9

Foschini, L. 2012, Research in Astronomy and Astrophysics, 12, 359

—. 2017, Frontiers in Astronomy and Space Sciences, 4, 6

Foschini, L., Ghisellini, G., Kovalev, Y. Y., et al. 2011, MNRAS, 413, 1671

Foschini, L., Angelakis, E., Fuhrmann, L., et al. 2012, A&A, 548, A106

Foschini, L., Berton, M., Caccianiga, A., et al. 2015, A&A, 575, A13

Fossati, G., Maraschi, L., Celotti, A., Comastri, A., & Ghisellini, G. 1998, MNRAS, 299, 433

Frederick, S., Kara, E., Reynolds, C., Pinto, C., & Fabian, A. 2018, ApJ, 867, 67

Fuhrmann, L., Karamanavis, V., Komossa, S., et al. 2016, Research in Astronomy and Astrophysics, 16, 176

Gallo, L. C. 2006, MNRAS, 368, 479

Gaskell, C. M. 2009, New Astron. Rev., 53, 140

Gebhardt, K., Bender, R., Bower, G., et al. 2000, ApJL, 539, L13

Ghisellini, G., Celotti, A., Fossati, G., Maraschi, L., & Comastri, A. 1998, MNRAS, 301, 451

Ghisellini, G., & Tavecchio, F. 2009, MNRAS, 397, 985

Ghisellini, G., Tavecchio, F., Foschini, L., et al. 2010, MNRAS, 402, 497

Gierliński, M., & Done, C. 2004, MNRAS, 349, L7

Goodrich, R. W. 1989, ApJ, 342, 224

Greene, J. E., & Ho, L. C. 2005a, ApJ, 627, 721

—. 2005b, ApJ, 630, 122

—. 2006, ApJL, 641, L21

Greene, J. E., Hood, C. E., Barth, A. J., et al. 2010, ApJ, 723, 409

Grier, C. J., Martini, P., Watson, L. C., et al. 2013, ApJ, 773, 90

Grupe, D. 2000, New Astron. Rev., 44, 455

Gu, M., & Chen, Y. 2010, AJ, 139, 2612

Gu, M., Chen, Y., Komossa, S., et al. 2015, ApJS, 221, 3

Gültekin, K., Richstone, D. O., Gebhardt, K., et al. 2009, ApJ, 698, 198

Haardt, F., & Maraschi, L. 1993, ApJ, 413, 507

Hagino, K., Odaka, H., Done, C., et al. 2016, MNRAS, 461, 3954

HI4PI Collaboration, Ben Bekhti, N., Flöer, L., et al. 2016, A&A, 594, A116

Ho, L. C., & Kim, M. 2014, ApJ, 789, 17

Ho, L. C., & Peng, C. Y. 2001, ApJ, 555, 650

Ishibashi, W., & Courvoisier, T. J.-L. 2011, A&A, 525, A118

Järvelä, E., Lähteenmäki, A., & Berton, M. 2018, A&A, 619, A69

Järvelä, E., Lähteenmäki, A., & León-Tavares, J. 2015, A&A, 573, A76

Järvelä, E., Lähteenmäki, A., Lietzen, H., et al. 2017, A&A, 606, A9

Jester, S., Schneider, D. P., Richards, G. T., et al. 2005, AJ, 130, 873

Jin, C., Done, C., & Ward, M. 2017a, MNRAS, 468, 3663

Jin, C., Done, C., Ward, M., & Gardner, E. 2017b, MNRAS, 471, 706

Jolley, E. J. D., & Kuncic, Z. 2008, MNRAS, 386, 989

Jones, D. H., Saunders, W., Colless, M., et al. 2004, MNRAS, 355, 747

Jones, D. H., Read, M. A., Saunders, W., et al. 2009, MNRAS, 399, 683

Kara, E., Fabian, A. C., Cackett, E. M., et al. 2013, MNRAS, 428, 2795

Kaspi, S., Smith, P. S., Netzer, H., et al. 2000, ApJ, 533, 631

Kellermann, K. I., Sramek, R., Schmidt, M., Shaffer, D. B., & Green, R. 1989, AJ, 98, 1195

Kelly, B. C. 2007, ApJ, 665, 1489

Khachikian, E. Y., & Weedman, D. W. 1974, ApJ, 192, 581

Kollatschny, W., & Zetzl, M. 2013, A&A, 549, A100

Komatsu, E., Smith, K. M., Dunkley, J., et al. 2011, ApJS, 192, 18

Komossa, S., Voges, W., Xu, D., et al. 2006, AJ, 132, 531

Komossa, S., Xu, D., Zhou, H., Storchi-Bergmann, T., & Binette, L. 2008, ApJ, 680, 926

Kondratko, P. T., Greenhill, L. J., & Moran, J. M. 2005, ApJ, 618, 618

Kormendy, J., & Ho, L. C. 2013, Annu. Rev. Astron. Astrophys., 51, 511

Koski, A. T. 1978, ApJ, 223, 56

Kovačević, J., Popović, L. Č., & Dimitrijević, M. S. 2010, ApJS, 189, 15

Kraemer, S. B., Schmitt, H. R., & Crenshaw, D. M. 2008, ApJ, 679, 1128

Krolik, J. H., & Begelman, M. C. 1988, ApJ, 329, 702

Krumpe, M., Lamer, G., Markowitz, A., & Corral, A. 2010, The Astrophysical Journal, 725, 2444

La Mura, G., Popović, L. Č., Ciroi, S., Rafanelli, P., & Ilić, D. 2007, ApJ, 671, 104

Laha, S., Ghosh, R., Guainazzi, M., & Markowitz, A. G. 2018, Monthly Notices of the Royal Astronomical Society, 480, 1522

Lähteenmäki, A., Järvelä, E., Ramakrishnan, V., et al. 2018, A&A, 614, L1

Laing, R. A., & Bridle, A. H. 1987, MNRAS, 228, 557

Laor, A., & Behar, E. 2008, MNRAS, 390, 847

Liao, N.-H., Liang, Y.-F., Weng, S.-S., et al. 2015, ArXiv e-prints, arXiv:1510.05584

Lister, M. L., Aller, M. F., Aller, H. D., et al. 2018, ApJS, 234, 12

—. 2013, AJ, 146, 120

—. 2016, AJ, 152, 12

Lister, M. L., Homan, D. C., Hovatta, T., et al. 2019, ApJ, 874, 43

Magorrian, J., Tremaine, S., Richstone, D., et al. 1998, AJ, 115, 2285

Malizia, A., Bassani, L., Bird, A. J., et al. 2008, MNRAS, 389, 1360

Mallick, L., Alston, W. N., Parker, M. L., et al. 2018, MNRAS, 479, 615

Maraschi, L., & Haardt, F. 1997, in Astronomical Society of the Pacific Conference Series, Vol. 121, IAU Colloq. 163: Accretion Phenomena and Related Outflows, ed. D. T. Wickramasinghe, G. V. Bicknell, & L. Ferrario, 101

Marziani, P., Zamanov, R., Sulentic, J. W., Calvani, M., & Dultzin-Hacyan, D. 2003, Mem. Soc. Astron. Italiana, 74, 492

Marziani, P., Dultzin, D., Sulentic, J. W., et al. 2018, Frontiers in Astronomy and Space Sciences, 5, 6

Mathur, S. 2000, MNRAS, 314, L17

Mauch, T., Murphy, T., Buttery, H. J., et al. 2003, MNRAS, 342, 1117

Morganti, R., Oosterloo, T., Oonk, J. B. R., Frieswijk, W., & Tadhunter, C. 2015, A&A, 580, A1

Mullaney, J. R., Alexander, D. M., Fine, S., et al. 2013, MNRAS, 433, 622

Mullaney, J. R., & Ward, M. J. 2008, MNRAS, 385, 53

Murphy, T., Sadler, E. M., Ekers, R. D., et al. 2010, MNRAS, 402, 2403

Oh, K., Koss, M., Markwardt, C. B., et al. 2018, ApJS, 235, 4

Osterbrock, D. E. 1977, ApJ, 215, 733

Osterbrock, D. E., & Pogge, R. W. 1985, ApJ, 297, 166

Padovani, P. 2017, Nature Astronomy, 1, 0194

Paliya, V. S., Ajello, M., Rakshit, S., et al. 2018, ApJL, 853, L2

Paliya, V. S., Parker, M. L., Jiang, J., et al. 2019, ApJ, 872, 169

Paliya, V. S., & Stalin, C. S. 2016, ApJ, 820, 52

Panessa, F., de Rosa, A., Bassani, L., et al. 2011, Monthly Notices of the Royal Astronomical Society, 417, 2426

Pariev, V. I., & Bromley, B. C. 1998, ApJ, 508, 590

Parker, M. L., Pinto, C., Fabian, A. C., et al. 2017, Nature, 543, 83

Peterson, B. M. 1993, Publ. Astron. Soc. Pac., 105, 247

Peterson, B. M., & Horne, K. 2004, Astronomische Nachrichten, 325, 248

Peterson, B. M., Ferrarese, L., Gilbert, K. M., et al. 2004, ApJ, 613, 682

Phillips, M. M. 1976, ApJ, 208, 37

—. 1978, ApJS, 38, 187

Pogge, R. W. 2011, in Narrow-Line Seyfert 1 Galaxies and their Place in the Universe, 2

Ponti, G., Papadakis, I., Bianchi, S., et al. 2012, A&A, 542, A83

Proga, D., Stone, J. M., & Kallman, T. R. 2000, ApJ, 543, 686

Rakshit, S., & Stalin, C. S. 2017, ApJ, 842, 96

Rakshit, S., Stalin, C. S., Chand, H., & Zhang, X.-G. 2017, ApJS, 229, 39

Rodríguez-Ardila, A., Pastoriza, M. G., & Donzelli, C. J. 2000, ApJS, 126, 63

Romano, P., Vercellone, S., Foschini, L., et al. 2018, MNRAS, 481, 5046

Rosen, S. R., Webb, N. A., Watson, M. G., et al. 2016, A&A, 590, A1

Ross, R. R., & Fabian, A. C. 2005, MNRAS, 358, 211

Salucci, P., Ratnam, C., Monaco, P., & Danese, L. 2000, MNRAS, 317, 488

Sargent, W. L. W. 1968, ApJL, 152, L31

Schlafly, E. F., & Finkbeiner, D. P. 2011, ApJ, 737, 103

Schmidt, M., & Green, R. F. 1983, ApJ, 269, 352

Schmitt, H. R., Antonucci, R. R. J., Ulvestad, J. S., et al. 2001, ApJ, 555, 663

Seyfert, C. K. 1943, ApJ, 97, 28

Shakura, N. I., & Sunyaev, R. A. 1973, A&A, 24, 337

Shapovalova, A. I., Popović, L. Č., Burenkov, A. N., et al. 2012, ApJS, 202, 10

Shen, Y., & Ho, L. C. 2014, Nature, 513, 210

Sikora, M., Stawarz, Ł., & Lasota, J.-P. 2007, ApJ, 658, 815

Sikora, M., Stawarz, Ł., Moderski, R., Nalewajko, K., & Madejski, G. M. 2009, ApJ, 704, 38

Tchekhovskoy, A., Narayan, R., & McKinney, J. C. 2011, MNRAS, 418, L79

The Fermi-LAT collaboration. 2019, arXiv e-prints, arXiv:1902.10045

Ulvestad, J. S., Antonucci, R. R. J., & Barvainis, R. 2005, ApJ, 621, 123

Urry, C. M., & Padovani, P. 1995, Publ. Astron. Soc. Pac., 107, 803

Vaona, L., Ciroi, S., Di Mille, F., et al. 2012, MNRAS, 427, 1266

Varisco, L., Sbarrato, T., Calderone, G., & Dotti, M. 2018, A&A, 618, A127

Veilleux, S., & Osterbrock, D. E. 1987, ApJS, 63, 295

Véron-Cetty, M. P., Véron, P., & Gonçalves, A. C. 2001, A&A, 372, 730

Vietri, A., Berton, M., Ciroi, S., et al. 2018, in Revisiting Narrow-Line Seyfert 1 Galaxies and their Place in the Universe, 47

Wang, T., & Lu, Y. 2001, A&A, 377, 52

Williams, R. J., Pogge, R. W., & Mathur, S. 2002, AJ, 124, 3042

Wood, M., Caputo, R., Charles, E., et al. 2017, International Cosmic Ray Conference, 301, 824

Yao, S., Komossa, S., Liu, W.-J., et al. 2019, MNRAS, 487, L40

Yao, S., Yuan, W., Zhou, H., et al. 2015, MNRAS, 454, L16

Yee, H. K. C. 1980, ApJ, 241, 894

Yip, C. W., Connolly, A. J., Szalay, A. S., et al. 2004a, AJ, 128, 585

Yip, C. W., Connolly, A. J., Vanden Berk, D. E., et al. 2004b, AJ, 128, 2603

Yuan, F., Gan, Z., Narayan, R., et al. 2015, ApJ, 804, 101

Yuan, W., Zhou, H. Y., Komossa, S., et al. 2008, ApJ, 685, 801

Zakamska, N. L., Strauss, M. A., Krolik, J. H., et al. 2003, AJ, 126, 2125

Zamanov, R., Marziani, P., Sulentic, J. W., et al. 2002, ApJ, 576, L9

Zdziarski, A. A., Fabian, A. C., Nandra, K., et al. 1994, MNRAS, 269, L55

Zhou, H., Wang, T., Yuan, W., et al. 2006, ApJS, 166, 128

Zhou, X.-L., Yang, F., Lü, X.-R., & Wang, J.-M. 2007, AJ, 133, 432

Zoghbi, A., Fabian, A. C., Uttley, P., et al. 2010, MNRAS, 401, 2419